Institut für Theoretische Physik

Fakultät Mathematik und Naturwissenschaften

Technische Universität Dresden

Dynamics of Cell Packing and Polar Order in Developing Epithelia

Dissertation

zur Erlangung des akademischen Grades

Doctor rerum naturalium

vorgelegt von

Reza Farhadifar

geboren am 24. Mai 1982 in Mashhad, Iran

Dresden   2009

Abstract

During development, organs with different shape and functionality form from a single fertilized egg cell. Mechanisms that control shape, size and morphology of tissues pose challenges for developmental biology. These mechanisms are tightly controlled by an underlying signaling system by which cells communicate to each other. However, these signaling networks can affect tissue size and morphology through limited processes such as cell proliferation, cell death and cell shape changes, which are controlled by cell mechanics and cell adhesion. One example of such a signaling system is the network of interacting proteins that control planar polarization of cells. These proteins distribute asymmetrically within cells and their distribution in each cell determines of the polarity of the neighboring cells. These proteins control the pattern of hairs in the adult *Drosophila* wing as well as hexagonal repacking of wing cells during development. Planar polarity proteins also control developmental processes such as convergent-extension. We present a theoretical study of cell packing geometry in developing epithelia. We use a vertex model to describe the packing geometry of tissues, for which forces are balanced throughout the tissue. We introduce a cell division algorithm and show that repeated cell division results in the formation of a distinct pattern of cells, which is controlled by cell mechanics and cell-cell interactions. We compare the vertex model with experimental measurements in the wing disc of *Drosophila* and quantify for the first time cell adhesion and perimeter contractility of cells. We also present a simple model for the dynamics of polarity order in tissues. We identify a basic mechanism by which long-range polarity order throughout the tissue can be established. In particular we study the role of shear deformations on polarity pattern and show that the polarity of the tissue reorients during shear flow. Our simple mechanisms for ordering can account for the processes observed during development of the *Drosophila* wing.
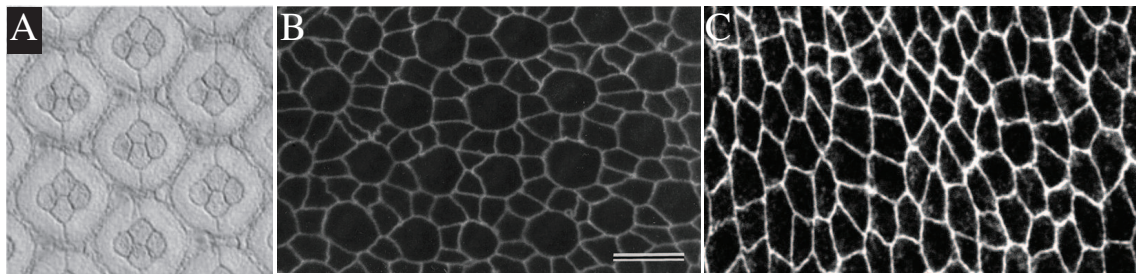
Contents

1 Introduction

1.1 Biophysics of Two-Dimensional Tissues

Figure 1.1: Examples of the epithelial junctional network. (A) *Drosophila* retina ommatidium (adapted from [1]), (B) basilar papilla of chicken embryo (adapted from [2]), and (C) *Drosophila* wing disc (adapted from [3]).

During development, organs with tremendous diversity in shape and functionality form from a single fertilized egg cell. Mechanisms that control shape, size and morphology of tissues are largely unknown. These mechanisms are tightly controlled by an underlying signaling system by which cells communicate to each other. For example, *morphogens*, molecules secreted by localized sources, spread in the tissue and guide the position dependent expression of genes and control tissues final size and shape [4]. Although many molecules are involved in the establishment of these signaling systems, the response of cells to such a flow of information throughout the tissue is limited to processes such as cell division, cell death, cell growth, cell migration and cell shape changes. All these processes are mainly governed by cell mechanics.

An important model system to study cell mechanics and cell adhesion is two-dimensional sheets of cells, called *epithelia*. Epithelia are formed by repeated cell division from a small group of cells, which have almost identical properties. Epithelial cells are packed in specific morphologies via cell-cell adhesion. These cell packings are inherently dynamic structures and remodel during development. However, biological tissues are structurally and functionally stable in physiological environments [11]. These two contradictory properties of tissues as active soft materials, have fascinated scientist for more than a century.

Epithelial cells assemble adhesive junctions with their neighbors in their apical region; the adhesion molecules, Cadherin, and components of the actin cytoskeleton are enriched apico-laterally. These apical junctions can be considered as a two-dimensional network that defines the cell packing geometry. In Fig. 1.1, three examples of the junctional network of cells are shown. In Fig. 1.1 A, we show the retina ommatidium[1] of the eye of the fruit fly. The specific arrangement of cells mimics light scattering, which is essential for correct vision. In Fig. 1.1 B and C, the junctional network of basilar papilla of a chicken embryo and the *Drosophila* wing disc are shown, respectively.

Basic physical principles that govern tissue shape and morphology have been studied in coarse-grained descriptions on different scales. They range from models that account for cell mechanics and shape to the hydrodynamic limit where the tissue exhibits the properties of an active viscoelastic fluid [12]-[19]. Here we discuss in more detail two models that are developed to study cell shape and cell packing geometry in epithelia. In [12], Graner and Glazier proposed an elastic energy functional for cell mechanics and cell-cell interactions based on the large-Q Potts model description of cells. This model describes a collection of N_C cells by defining N_C degenerate spins, $\sigma(i,j) = 1, 2, ..., N_C$, where i and j defines a lattice site. A cell σ is defined as a collection of all sites in the lattice with spin σ. Their energy functional has two terms: the first term accounts for cell-cell interactions and the second term accounts for the area elasticity of cells. They use the Monte Carlo method to minimize their energy functional; at each step a lattice site is selected at random and its spin is changed from σ to σ' with probability zero, if the change in energy, $\Delta\mathcal{H}$, is positive, 0.5 if $\Delta\mathcal{H} = 0$ and one if $\Delta\mathcal{H} < 0$.

This model has been used to study cell sorting [12]. Graner *et al.* define two cell populations with different interaction energies. Cells of similar type attract each other differently than cells of the other type. Graner *et al.* show that this can result in cell sorting starting from a mixed initial configuration. Graner *et al.* also use this model to study convergent-extension [22]-[24], a process in which the tissue expands in one direction while contracting in the other direction in the absence of cell divisions and cell shape changes. To trigger this phenomenon by energy minimization, they assume that the adhesive energy of the contact surface between two cells depends on its orientation relative to the axis of elongation of the two cells; i.e. the level of adhesion molecules might differ on long and short sides of a cell. They showed that this mechanism can result in elongation of cells and convergent-extension.

Hufnagel *et al.* [14] suggest a three dimensional description of tissue mechanics, in which each cell is represented as a polygon with certain height. The position, shape and height of cells are determined by the condition of mechanical equilibrium that corresponds to minimization of

---

[1]The compound eye of insects is composed of units called ommatidia. An ommatidium contains a cluster of photoreceptor cells surrounded by support cells.

the energy functional

$$E(r_i, \xi_i) = \sum_\alpha \left[\rho_\alpha + a \left(V_\alpha - V_0 \right)^2 + b \sum_{\beta = \nu(\alpha)} (\xi_\alpha - \xi_\beta)^2 + c(\xi_\alpha - 1)^2 \right], \qquad (1.1)$$

where ρ_α, V_α, and ξ_α denote the perimeter, volume, and the height of cell α, respectively. V_0 is the preferred volume of cells and the second summation in the parentheses is over all neighbors of cell α that are labeled as $\nu(\alpha)$. In this model, the first term mimics cytoskeletal tension and the second and third terms control deviations of cell volume from V_0 and the penalty on the variation of cell height between adjacent cells, respectively. The fourth term accounts for deviation of cell height from its unstressed value. The authors use this model together with a signaling network to study growth control in developing epithelia due to mechanical feedback.

1.2 Cell Packing and Tissue Morphology

Cell packing geometry was one of the earliest observations after the invention of the microscope [25]. Although the hexagonal packing observed in simple epithelia was explained in the early 1900s by Thompson in his book *On Growth and Form* [26], the packing geometry of proliferating tissues is still under debate. Proliferating epithelia are not necessarily hexagonally packed, but rather cells with different neighbor number coexist. It was shown recently that the frequency of different classes of polygons is highly reproducible even between different species. In Fig. 1.2, we show the distribution of different classes of polygons for the *Drosophila* wing disc, the *Hydra* epidermis and the tail epidermis of *Xenopus* [27]. In these three epithelia, hexagons are the most frequent polygons and pentagons and heptagons are the next most frequent polygon classes.

The distribution of different classes of polygons was first studied theoretically by Cowan and Morris in [28] and [29], in which they introduced the hypothetical organism, *Tessellata elegans*, which is a monolayer planar tissue. Its development starts from one polygonal cell with arbitrary edge number. Division corresponds to adding a new boundary passed randomly from two sides. A n-sided cell will divide into two cells with edge numbers that are either $(3, n+1)$, $(4, n)$, $(5, n-1)$, $\cdots$, $((n+3)/2, (n+5)/2)$ if n is odd and $((n+4)/2, (n+4)/2)$ if n is even. For example, a four-sided cell can divide into either a triangle and a five-sided cell or two four-sided cells. This rule can be described by a matrix M. Each matrix element, M_{ij},
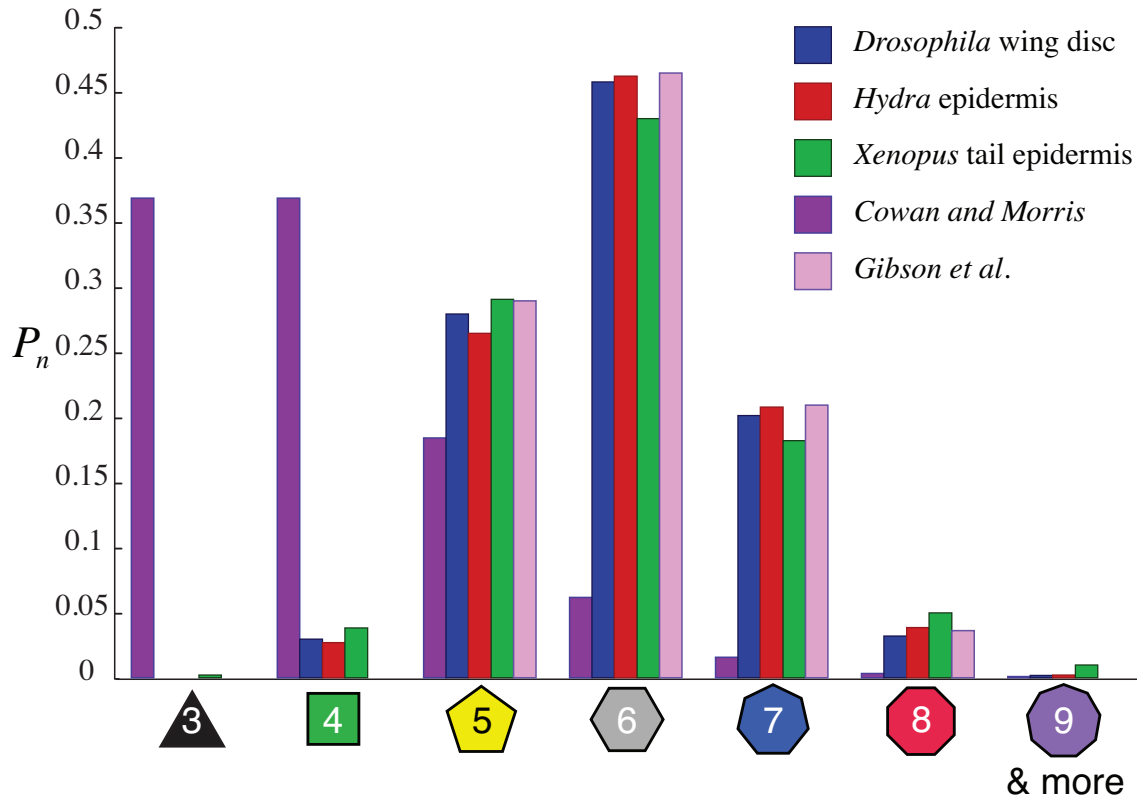
Figure 1.2: Distribution of different classes of polygons in the *Drosophila* wing disc, *Hydra* epidermis and *Xenopus* tail epidermis (adapted from [27]). Note that the distribution of polygon classes for the wing disc presented in [27] is slightly different from those that we will discuss in Chap. 6. This probably reflects the different methods used for assigning cells to polygon classes. Polygon-class distribution depends on the cutoff used to distinguish boundaries from four-fold vertices (see App. E). For comparison, we show the distribution of polygon classes that are found by Cowan and Morris [29] and Gibson et al. [27].

is the probability that an i-sided cell divides to produce a j-sided daughter cell

$$
M = \begin{bmatrix}
1/2 & 1/2 & & & & \\
1/3 & 1/3 & 1/3 & & & \\
1/4 & 1/4 & 1/4 & 1/4 & & \\
1/5 & 1/5 & 1/5 & 1/5 & 1/5 & \\
1/6 & 1/6 & 1/6 & 1/6 & 1/6 & 1/6 \\
\vdots & \vdots & \vdots & \vdots & \vdots & \vdots
\end{bmatrix} .
\tag{1.2}
$$

The frequency of different classes of polygons in generation t, $m_t = \{P_3, \ P_4, \ P_5, \ \cdots\}$, relates

to the frequency of polygon classes one generation before through matrix M

$$
\begin{aligned}
m_t &= m_{t-1}M \\
&= m_{t-2}M^2 \\
&\vdots \\
&= m_0 M^n.
\end{aligned}
\tag{1.3}
$$

Cowan and Morris showed in [29] that there exists a stationary distribution of polygon classes starting from any initial condition, which is shown in Fig. 1.2 A.

Clearly the distribution found by Cowan and Morris is different from what is found in nature for different epithelia. In [27], Gibson *et al.* suggest a different division rule that prevents formation of triangles. Therefore a four-sided cell can only divide into two four-sided cells and a five-sided cell can divide into four- and five-sided cells. The matrix M is now given by

$$
M = \begin{bmatrix}
1 & & & \\
1/2 & 1/2 & & \\
1/4 & 1/2 & 1/4 & \\
1/8 & 3/8 & 3/8 & 1/8 \\
\vdots & \vdots & \vdots & \vdots
\end{bmatrix}.
\tag{1.4}
$$

Note that here the rows and columns of M start from four-sided cells. They also introduce a mean-field approximation to take into account edges that are added to neighboring cells of a dividing cell. If a cell divides, two neighbor cells of the dividing cell also gain one new boundary. On average, all cells gain one boundary per generation due to division of neighboring cells. This can again be represented by a matrix S

$$
S = \begin{bmatrix}
0 & 1 & & & \\
 & 0 & 1 & & \\
 & & 0 & 1 & \\
 & & & 0 & 1 \\
 & & & \vdots & \vdots
\end{bmatrix}.
\tag{1.5}
$$

Now the frequency of polygon classes evolves as $m_t = m_{t-1}MS$, which again converges to an equilibrium distribution and is different from that found by Cowan and Morris (see Fig. 1.2). In this model, hexagons are the most common polygons and the distribution is more similar to experimental observations than that of Cowan and Morris. However, this model predicts no four-sided cells in its equilibrium configuration due to the mean-field approximation introduced by matrix S which adds one neighbor to all cells. These topological rules that are discussed in these papers are not based on the physical properties of the cells. However, we expect the

redistribution of neighbors after cell division to depend on physical cellular properties. Also, a purely topological description cannot account for cell size and shape or local force balances.

Apart from the topological inhomogeneity discussed above, cell area and cell shape is also inhomogeneous in proliferating epithelia. The geometric disorder induced by cell division in proliferating epithelia was first studied in 1928, when F.T. Lewis examined the epidermal cells of the cucumber [30] and [31]. Lewis noted that cells with different neighbor numbers were present in reproducible proportions, and their average areas varied linearly with neighbor number. This relation was termed Lewis's law when it was first studied theoretically by Rivier and Lissowski in 1982 [32]. Rivier and Lissowski showed that cellular networks with this property are dominant in the plane's random polygonal tiling that are subject to the constraints of space filling and an average neighbor number of six.

1.3   Planar Polarity of Epithelial Cells

The polarization of epithelial cells in the apical-basal axis (perpendicular to the plane of the epithelia) is well studied and it has been shown that this polarity is critical for the integrity and functionality of the epithelia. Most epithelia are also polarized in a second axis, in the plane of the epithelium. This phenomenon is known as planar cell polarity or tissue polarity. Planar polarity coordinates cell behavior across the epithelium. This polarity is clearly visible in the epidermis of animals. For example, the scales, bristles, and hairs of insects are typically aligned along the major body axis. A similar polarity is seen in the epidermis of vertebrates, e.g. the scales of fish and hair of mammals [36]. Planar polarity is not limited to cells that are fixed in space. For example, elongation of the body axis during development involves the coordination of multiple cell behaviors including cell rearrangement, cell division, and cell shape changes [37]- [40].

In Fig. 1.3, we show three features of planar polarity in wild-type animals and in mutants that cannot establish this planar polarity. Fig. 1.3 A shows hair polarity in the adult *Drosophila* wing, where each cell produces a single cytoskeletal extension which becomes the so-called wing hair of the adult fly. Wing hairs point distally in wild-type animals, however, in mutants hairs are misorientated as shown in Fig. 1.3 B. Similarly, the mechanosensory hair cells of the mouse cochlea extend a series of polarized actin-rich stereociliary bundles that point toward the fluid-filled lumen of the cochlea and respond to mechanosensory input [41]. We show, an example of sensory receptor cells of the wild-type mouse cochlea in Fig. 1.3 C. In mutants, the bundles form but the overall alignment is disrupted as shown in Fig. 1.3 D. In addition to the polarity of individual cells, group of cells can also behave in a polarized manner, e.g. rotational symmetry breaking of ommatidia in the *Drosophila* eye. Ommatidia are composed of multiple cells in which some cells in each unit differentiate in an asymmetric fashion. The entire
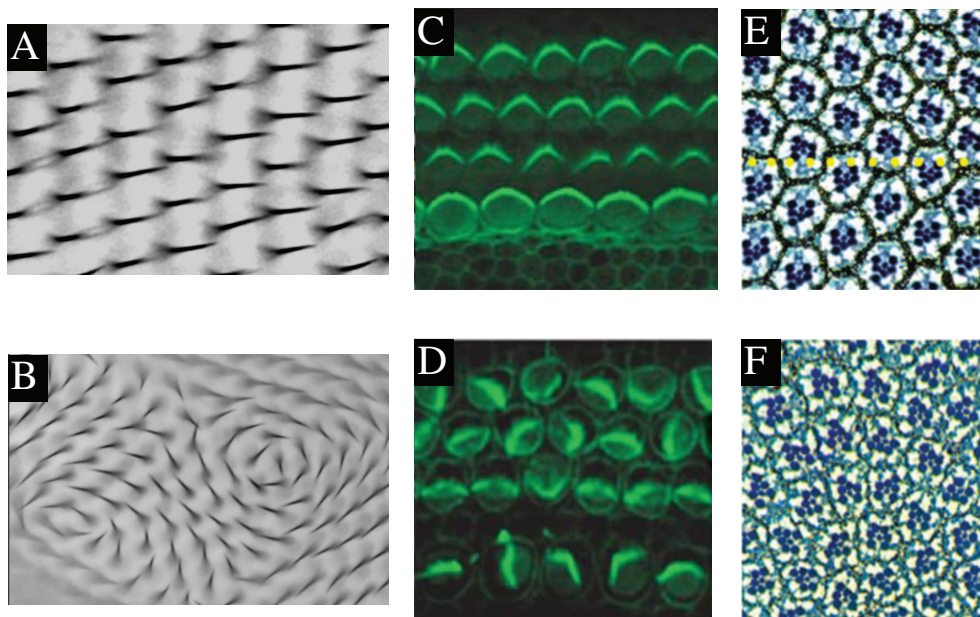
Figure 1.3: Features of planar polarity in epithelia. (A) and (B) Hair pattern in the wild-type and mutant (diego) *Drosophila* wing, respectively (adapted from [3]). In wild-type animals, hairs point in the distal direction of the wing. However, in the mutants hairs are misoriented and defective hair patterns form. (C) and (D) Wild-type and mutant (frizzled) sensory hair cells of the mouse cochlea (adapted from [38]). In wild-type animals, individual sensory cells generate polarized bundles of actin-based stereocilia. In mutants these bundles still form but their orientation becomes randomized. (E) and (F) The wild-type and mutant (frizzled) of the *Drosophila* ommatidia, or facets, which are composed of photoreceptors (adapted from [83]). In wild type animals, ommatidia are arranged in precisely oriented trapezoids, while in the mutant both the arrangement of the photoreceptors in ommatidium and the arrangement of ommatidia with respect to the whole eye become disorganized.

structure rotates as a unit in the opposite direction in the dorsal and ventral halves of the eye [42]-[43]. In Fig. 1.3 E, we show part of the *Drosophila* eye near the dorsal-ventral boundary, where the boundary is marked by yellow dots. As shown in Fig. 1.3 F, in mutants, both the arrangement of cells in each ommatidium and the alignment of the ommatidia with respect to the eye is influenced.

An important model system to study planar cell polarity (PCP) is the *Drosophila* wing, in which the polarity is readable from the hair pattern in the adult wing. Studies started in 1980s led to the identification of what is now called the *Frizzled* pathway for the development of tissue polarity [44]-[49]. The core PCP pathway consists of the cell-surface proteins *Frizzled* [50], *Strabismus* (or *Van Gogh*) [43], [51], and *Flamingo* (or *Starry night*) [52], [53]. There are

also cytoplasmic proteins *Dishevelled* [54], [55], *Prickle* (or *Spiny legs*) [56] and *Diego* [57], that control tissue polarity. Mutants of these proteins generate different patterns of hairs in the wing. In mutants of the core PCP proteins, wing hairs initiate from a central location on the apical cell surface and point in the wrong direction. However, in mutants of the cytoplasmic proteins, the hairs grow from the distal part of the cell but global orientation is affected and swirling patterns form (see Fig. 1.3 B).
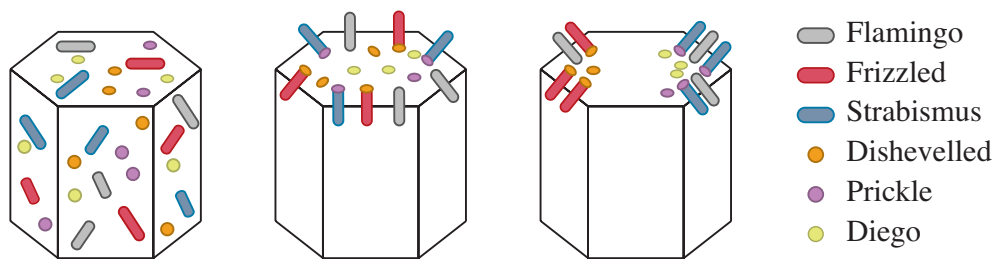
Figure 1.4: Schematic of planar cell polarity proteins. Proteins involved in establishment of planar cell polarity fall into two main categories: core PCP proteins and surface proteins. These proteins are recruited to the apical surface of cells at early development. They are sorted out preferentially towards the distal and proximal sides of the cell, which requires the activity of all polarity proteins. Strabismus, and Prickle localize at the proximal cell surface, and Frizzled, Dishevelled, and Diego localize at the distal surface, while Flamingo exists on both sides of the cell (adapted from [35]).

Formation of hairs in the *Drosophila* wing requires an underlying molecular polarity that includes an asymmetric distribution of core PCP proteins. The core PCP proteins are first recruited to the apical cell surface and subsequently segregate into complementary apical subdomains before the onset of hair formation. Flamingo localizes at proximal and distal surfaces [53] and [58], whereas Frizzled, Dishevelled, and Diego localize at specifically the distal surface [59]-[61]. Prickle and Strabismus localize at the proximal surface [56] and [62]. Frizzled can interact directly with Dishevelled [63], and Strabismus can associate with Prickle [62] and [64]. This indicates that proximal and distal cell domains consist of at least two protein complexes. The Flamingo cadherin, which is capable of mediating homophilic adhesion [53], recruits the other core PCP proteins to the region of the adherens junctions [60]. Once at the surface, the activity of all six core PCP proteins is required for any of them to achieve a planar polarized distribution [60], indicating that these proteins participate in a regulatory loop rather than a strict linear pathway [35]. In Fig. 1.4, a schematic illustrating the distribution of these proteins in the cell is shown.

During the global organization of polarity in tissues the asymmetric localization of PCP proteins is sensitive not only to the activity of PCP proteins in the same cell but also to PCP

activity in adjacent cells. Frizzled activity in one cell is required for Prickle localization in its distal neighbor, whereas Prickle is required for the localization of Dishevelled in the adjacent proximal cell, suggesting that Frizzled and Prickle interact indirectly across cell boundaries [56]. Within a cell, there is evidence that Prickle can block the association between Frizzled and Dishevelled [56], although other studies find that Prickle over-expression does not disrupt Dishevelled membrane localization [62]. Conversely, the Diego protein can associate with Prickle and Strabismus [61] and may counteract Prickle activity to allow Frizzled-Dishevelled complexes to form at the distal surface [64]. These interactions suggest a mechanism by which proximal Strabismus-Prickle complexes and distal Frizzled-Dishevelled complexes form in mutually exclusive cellular domains. These proteins could come into contact when they are first recruited to the apical surface of wing cells during the establishment of polarity.

Currently there are two types of model that have been proposed to explain how polarity is established throughout a tissue. The first model is based on the gradient of a diffusible molecule and individual cells might determine their polarity in accordance with the direction of the slope of the gradient. This model is motivated by experiments carried out in insects other than *Drosophila*. In these experiments, sections of larval epidermis were rotated or moved to different positions in a segment, resulting in reproducible alterations in polarity of the adult cuticle [65]. Any experiment leading to an alteration in the direction of this slope would cause polarity to be inverted [66]-[68]. In the second type of model, polarity information is propagated via a cell-cell interaction, whereby signals are passed directly between adjacent cells, without any necessary role for longer range diffusible signals. One example of this class of models involves each cell polarizing in response to a local secreted ligand and then, in turn, locally secreting a ligand to signal to its neighbors, thus progressively propagating polarizing information throughout a tissue [69].

The second model has been discussed more rigorously recently in [70]. In this "feedback" model, planar polarity could occur through an asymmetric distribution of Frizzled in cells with comparable levels of Frizzled activity. Frizzled accumulation at the distal surface of a cell would recruit or retain Strabismus on the proximal surface of the adjacent cell, stabilizing their complementary distributions. Strabismus-Prickle and Frizzled-Dishevelled complexes could then segregate into reciprocal domains in both cells through an antagonistic effect of the proximal Prickle protein on Frizzled-Dishevelled association. As a result, Frizzled is predicted to accumulate on the distal surface of the neighboring cell, thus allowing the cycle to continue. This model demonstrates that, given a distal bias in Frizzled localization, local interactions among PCP proteins could provide a robust mechanism for generating planar cell polarity in the absence of a Frizzled gradient. This model can reproduce both wild-type planar polarity and the complex patterns that arise in some mutants.

1.4   Wing Development of the Fruit Fly *Drosophila*
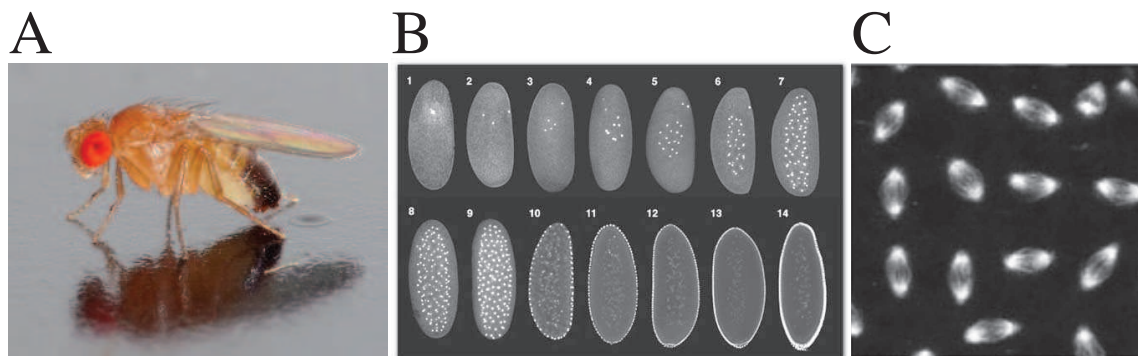
Figure 1.5: *Drosophila* embryonic development. (A) *Drosophila* melanogaster, which is commonly used in biological studies (source Wikipedia photographed by Andre Karwath). (B) Early embryonic development in the fruit fly *Drosophila*, in which rapid DNA replication happen in $\sim$ 3 hours and the nuclei accumulate on the surface of the york sac (adapted from [72]). (C) Part of the *Drosophila* embryo during DNA replication (adapted from [73]).

Drosophila melanogaster is a two-winged insect otherwise known as the common fruit fly or vinegar fly (see Fig. 1.5 A). It is one of the most frequently used model organisms in biology, including studies in genetics, physiology and life history evolution. The developmental period for *Drosophila* melanogaster varies with temperature; the shortest development time (egg to adult), 7 days, is achieved at 28° C and it increases at higher temperatures (30^oC, 11 days). Females lay $\sim$ 400 eggs (embryos) into rotting fruit or other suitable material. The eggs, which are about 0.5 millimeters long, hatch after 12-15 hours. The resulting larvae grow for about 4 days (at 25° C) while molting twice, at about 24 and 48 hours after hatching. During this time, they feed on the microorganisms that decompose the fruit, as well as on the sugar of the fruit itself. The larvae then encapsulate in the puparium and undergo a four-day-long metamorphosis (at 25° C), after which the adults emerge.

Drosophila melanogaster was among the first organisms used for genetic analysis, and today it is one of the most widely-used and genetically best-known of all eukaryotic organisms. All organisms use common genetic systems, therefore comprehending processes such as transcription and replication in fruit flies helps in understanding these processes in other eukaryotes, including humans. There are several reasons, to use *Drosophila* as a model system:

(i) The care and culture requires little equipment and uses little space even when studying large cultures, and the overall cost is low.

(ii) It is small and easy to grow in the laboratory and its morphology is easy to identify once they are anesthetized.

(iii) It has a short generation time (about 10 days at room temperature) so several generations can be studied within a few weeks.

(iv) It has a high fecundity (females can lay more than 800 eggs in a lifetime, i.e. one egg every 30 minutes with sufficient food).

(v) Males and females are readily distinguished and virgin females are easily isolated, facilitating genetic crossing.

Embryogenesis in *Drosophila* has been extensively studied. After fertilization of the oocyte the early embryo undergoes rapid DNA replication, until approximately 5,000 to 6,000 nuclei accumulate in the unseparated cytoplasm of the embryo. By the end of the 8th division most nuclei have migrated to the surface, surrounding the yolk sac. After the 10th division the pole cells form at the posterior end of the embryo, segregating the germ line from the syncytium (a large cell-like structure filled with cytoplasm containing many nuclei). Finally, after the 13th division, cell membranes slowly invaginate, dividing the syncytium into individual somatic cells. In Fig. 1.5 B, we show the embryonic development in the fruit fly *Drosophila* and in Fig. 1.5 C, we show part of the embryo with microtubules stained. Once this process is completed, gastrulation starts.
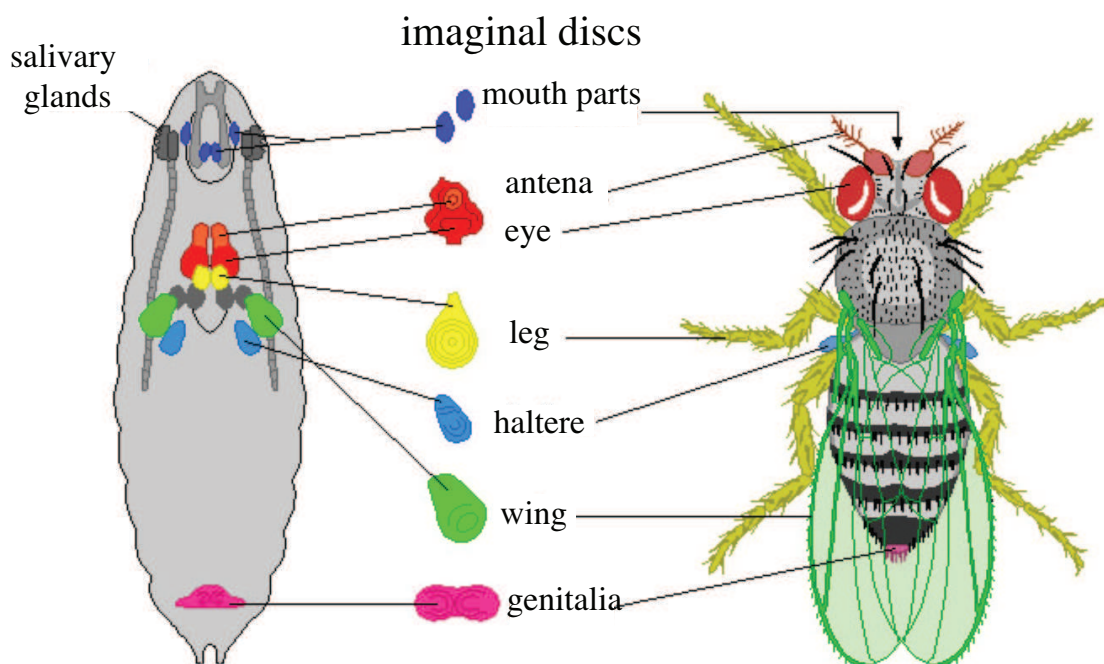
Figure 1.6: *Drosophila* imaginal discs. Schematic of *Drosophila* imaginal discs during metamorphosis. Each external part of the insect develops from a small number of cells which grows via cell division (adapted from [74]).

The embryo undergoes well-characterized morphogenetic movements during gastrulation and early development, including germ-band extension, formation of several furrows, ventral

invagination of the mesoderm, posterior and anterior invagination of endoderm (gut), as well as extensive body segmentation until finally hatching from the surrounding cuticle into a 1st-instar larva. During larval development, tissues known as *imaginal discs* grow inside the larva. An imaginal disc is one of the parts of a insect larva that will become a portion of the outside of the adult insect during the pupal transformation (see Fig. 1.6). Contained within the body of the larva, there are pairs of discs that form, for instance, the wings or legs or antennae or other structures in the adult. During the pupal stage, adult structures including the discs undergo rapid development. Each disc everts and elongates, with the central portion of the disc becoming the distal part of whichever appendage it is forming, such as wing, leg, antenna, etc.
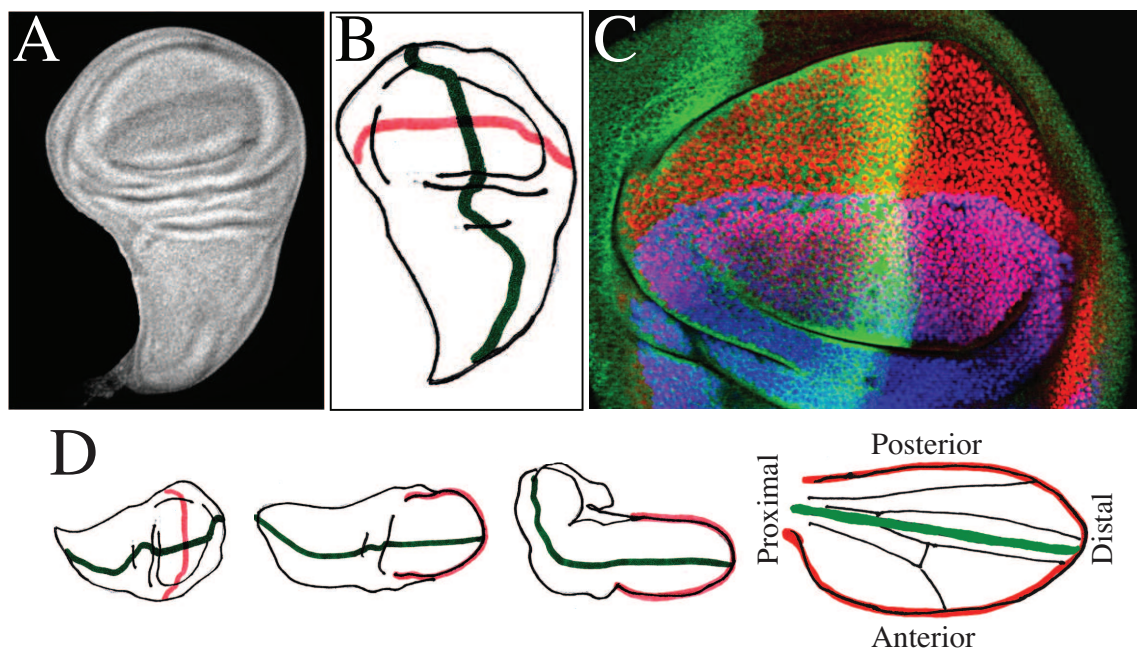
Figure 1.7: *Drosophila* wing development. (A) Wing disc of the fruit fly *Drosophila*. The wing disc grows from ~ 50 to $50,000$ cells in five days (taken by O. Wartlick). (B) Schematic of the anterior-posterior (green) and dorsal-ventral (red) compartment boundary in the wing disc (adapted from [3]). (C) Example of the *Drosophila* wing disc labeled with apterous in blue, vestigial in red, and Cubitus interruptus (which only expresses in anterior cells) in green (adapted from [75]). (D) Schematic of development of the *Drosophila* wing during metamorphosis (adapted from [3]). Initially dorsal and ventral parts of the wing are in the same plane. During metamorphosis, the wing disc folds and extends, so that the dorsal and ventral compartments come into contact with each other.

The wing imaginal disc is an excellent system for analyzing pattern formation. The wing disc is initially specified in the embryo as cluster of $20-40$ cells. During larval development, the disc

grows ~ 1000 fold. The wing disc is divided by a compartment boundary that separates it into the anterior and posterior developmental regions. There is also a second compartment boundary between the dorsal and ventral region, which develops during the second larval instar. When the wing forms at the metamorphosis, the future ventral surface folds under the dorsal surface in the distal region to form the double-layered wing. In Fig. 1.7 A, we show an example of the *Drosophila* wing disc. A schematic of the anterior-posterior and dorsal-ventral compartment boundaries are shown in Fig. 1.7 B as green and red lines, respectively.

In the wing disc, signaling regions are set up along the compartment boundaries. Cells at the anterior-posterior compartment boundary form a signaling region that specifies pattern along the anteroposterior axis of the wing. A cascade of events sets up this signaling center. It begins with the expression of the *engrailed* gene in the posterior compartment of the disc, which reflects the pattern of gene expression in the embryonic segment from which the discs derive. Cells expressing *engrailed* also express the segment polarity gene, *hedgehog*. At the compartment boundary, the secreted *hedgehog* protein acts over about 10 cell diameters and induces adjacent cells in the anterior compartment to express the *decapentaplegic* (or Dpp) gene. The dorsal-ventral compartment boundary is also a source of signaling region. Cells in the dorsal compartment express the gene *apterous*, which induces the synthesis of the proteins *fringe* and *Serrate*. Their action leads to the *Notch* receptor protein being activated in a discrete band of cells that later leads to expression of the gene *wingless*. Both Dpp and wingless act as morphogens whose concentrations provides cells with positional information. The formation of gradients of morphogen activity is not due to simple diffusion, but rather set up by active transport of the morphogen and involves endocytosis. Both Dpp and wingless can regulate the expression of their receptors. In Fig. 1.7 C, we show an example of the *Drosophila* wing disc labeled with apterous in blue, vestigial in red, and Cubitus interruptus (which only expresses in anterior cells) in green, which indicates the position of compartment boundaries. By the end of growth, the wing disc folds and extends, so that the dorsal and ventral surfaces come into contact with each other, as illustrated in Fig. 1.7 D.

2 Physical Description of Cell Packing
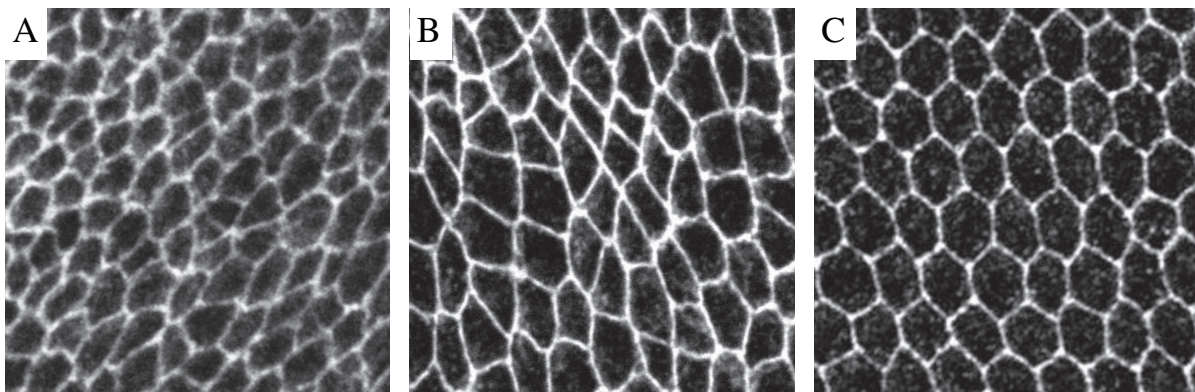
Figure 2.1: Examples of the apical junctional network in the wing epithelia of the fruit fly for different stages of development: (A) wing disc stage, (B) pupal stage and (C) before hair formation (provided by [3]).

Cell packing in epithelia has fascinated scientists for more than a century. In the early 1900s, D'Arcy Wentworth Thompson presented in his famous book, "On Growth and Form", how forces arising from surface tensions can result in hexagonal packing of epithelial cells. The mechanisms governing cell shape and epithelial packing are still unclear. Cell packing is tightly controlled during epithelial development by a complicated network of genes and can vary from an irregular packing geometry to a very specific one; we show in Fig. 2.1 three examples of epithelial packing for different stages of development of the wing of the fruit fly *Drosophila*. Although cells have irregular packing and shape in the wing disc stage (Fig. 2.1 A), they form an almost perfect hexagonal packing in the late stage before hair formation (Fig. 2.1 C).

Cell shape and cell packing is influenced mostly by cell mechanics. Thus to address the question of how cell packing geometry is controlled, we need to develop a framework to study cell mechanics. In this chapter we present a model to account for cell mechanics and cell-cell interactions in epithelia. Since the most interesting features of cell packing occur at the level

of the junctional network of cells, our two-dimensional model only considers the mechanics of this network. However, our model accounts for the third dimension indirectly by considering a preferred area for each cell such that deviation from this preferred area requires work to be done. We also account for cell adhesion and perimeter contractility, both of which influence cell shape. We then study the ground states of our model and show that, depending on physical parameters of the model, three different ground states can exist. We calculate the bulk and shear modulus of the network as a function of model parameters. We observe that the model exhibits a phase transition from a solid hexagonal network to a soft irregular one.

2.1 Cell Mechanics in Two-Dimensional Tissues
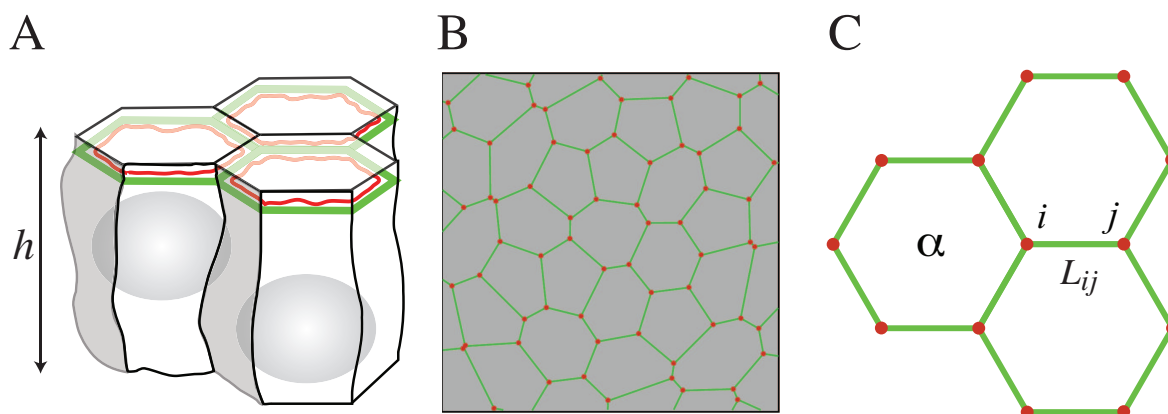
Figure 2.2: Vertex model. (A) Schematic of epithelial cell packing. Epithelial cells are connected to each other in their apical region by adhesion molecules, which are more pronounced along a network of adhesive junctions (green), and which are also associated with actomyosin fibers (red). They are connected to the extracellular matrix in their basal level. (B) Example of cell packing in vertex model. Each cell is represented as a polygon composed of vertices (red dots) which has straight edges. (C) Schematic of the vertex model, where cells are indicated by $\alpha = 1, 2, ..., N_C$, and vertices are indicated by $i = 1, 2, ..., N_V$. N_C and N_V are the total number of cells and vertices in the network, respectively. The length of the cell boundary between vertex i and j is indicated by L_{ij}.

There are many processes that occur within tissues on different time scales, such as the turnover of specific molecules inside the cells and pattern formations throughout the tissues. There are three main time scales regarding tissue dynamics. The shortest time scale is due to relaxation of cell shape in response to local perturbations. This is on the order of seconds to minutes. Cell division and cell rearrangements take one to several hours, and the formation of

tissue shapes and patterns happen on time scales of tens of hours to days. The adheren junctional network of epithelial cells is a stable configuration on time scales shorter than those of cell division, and longer than those of local perturbations. These network configurations obey a force balance (the net force on the junctional network is zero). In general, forces acting on the junctional network need not be derived from an energy function. However, the forces we consider here can, in our simple description, be represented by an energy function.

Here we assume that cells are represented as polygons (straight lines connecting vertices, see Fig. 2.2 B). This is a good approximation for most epithelia, such as the junctional network of cells in the wing of *Drosophila*, which is the subject of our experimental studies in this thesis. Therefore, the energy of the junctional network is a function of position of these vertices: $\mathcal{F} = \mathcal{F}(\mathbf{R}_i)$, where $\mathbf{R}_i = (x_i, y_i)$ is the position of vertex i in the tissue. The force balance then implies that the net force on each vertex is zero: $\mathbf{F}_i = -\partial \mathcal{F}/\partial \mathbf{R}_i = 0$, for $i = 1, ..., N_V$. The energy function $\mathcal{F}$, which corresponds to the work required to deform the junctional network of cells, consists of three terms regarding cell mechanics and cell-cell interactions

$$\mathcal{F} = \sum_{\alpha} \frac{K_{\alpha}}{2} (A_{\alpha} - A_{\alpha}^{(0)})^2 + \sum_{\langle i,j \rangle} \Lambda_{ij} L_{ij} + \sum_{\alpha} \frac{\Gamma_{\alpha}}{2} L_{\alpha}^2. \tag{2.1}$$

The first summation is over all cells $\alpha = 1...N_C$, where N_C is the total number of cells in the network. The area and area elasticity modulus of cell α are denoted by A_{α} and K_{α}, respectively. $A_{\alpha}^{(0)}$ is the preferred area of cell α which is related to the volume, V_{α} and height, h_{α} of the cell: $A_{\alpha}^{(0)} \simeq V_{\alpha}/h_{\alpha}$ (see Fig. 2.2 A). The area elasticity modulus K_{α} is proportional to the Young's modulus of the cells, Y_{α} and the inverse of the preferred area: $K_{\alpha} \simeq Y_{\alpha} h_{\alpha}/A_{\alpha}^{(0)}$. The bulk properties of the cells give rise to this term, which accounts for an effective area elasticity for cells. Any change in the apical area of cells requires that the material in this region flow toward the basal part of the cell. Since the volume of the cell is changing very slowly compared to cell shape relaxations, any changes in the apical area cause bending of the lateral boundaries of the cells, which requires work to be done and this effect is taken into account by this term.

Multiple mechanisms might influence line tension such that it could vary from edge to edge. For example, adhesive interactions between cells may favor cell-boundary expansion, whereas the subcortical actin cytoskeleton might oppose it. The second term in the energy function in Eq. 2.1 accounts for cell-cell interactions along the junctional region of cell boundaries. The summation is over all cell boundaries $\langle i, j \rangle$ and L_{ij} is the length of the boundary (see Fig. 2.2 C). Line tension Λ_{ij} describes forces along boundary $\langle i, j \rangle$, which can be positive or negative depending on the tensile properties of cell boundaries: if the boundary has surface tension properties, then Λ_{ij} is positive; if adhesion predominates then Λ_{ij} is negative. The underlying cellular cytoskeleton mainly contributes to this line tension, but it may also produce an effective perimeter contractility. This perimeter contractility is mimicked by the third term in Eq. 2.1, which is a summation over all cells in the network. The perimeter and perimeter contractility

of cell α are shown by L_α and Γ_α, respectively. This third term tends to shrink the perimeter, and therefore the area of cells, to zero, which is in opposition to the area elasticity term, which tends to keep the area of cells equal to their preferred area.

2.2   Ground States of Cell Packing
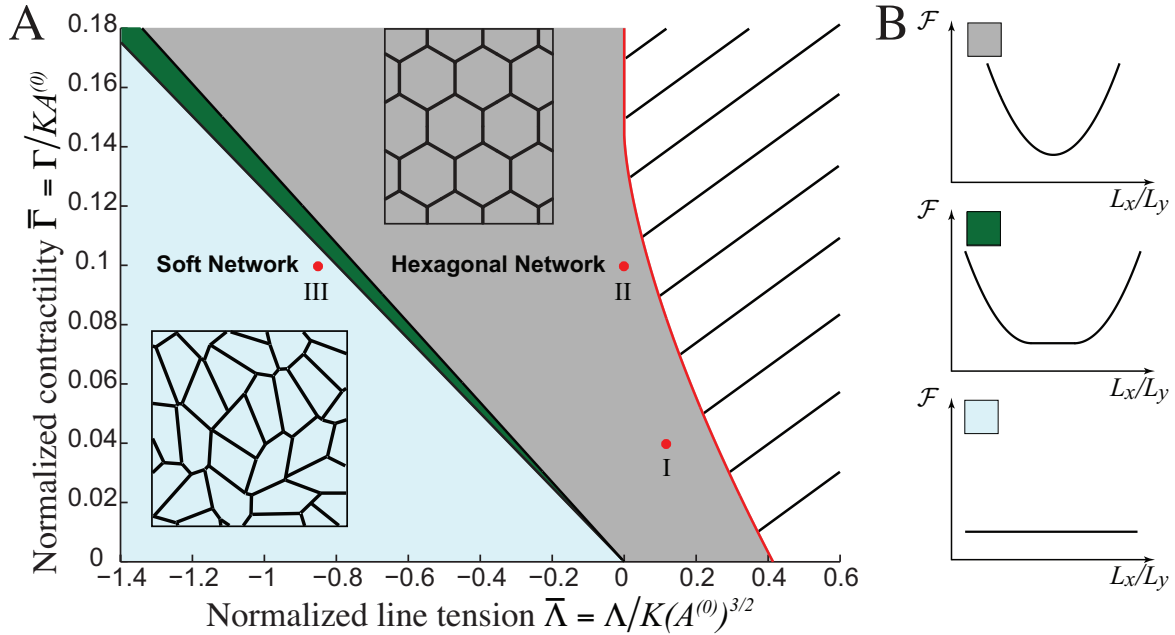
Figure 2.3: Ground-State phase diagram of the vertex model. (A) Phase diagram for the ground state of the vertex model for the energy function given in Eq. 2.1 as a function of dimensionless line tension $\bar{\Lambda}$ and dimensionless contractility $\bar{\Gamma}$. In the gray region the ground state is a hexagonal network with a nonzero shear modulus. In the green region, the network is semisoft and the shear modulus vanishes for limited deformations. The ground state in the green region is degenerate; any hexagonal network configuration where cells are irregular in shape, with area and perimeter of all cells equal to $A^{(0)}$ and $L^{(0)}$, respectively, is a ground state in this green region. The ground state of the energy in the blue region is also degenerate, and any network configuration where the area of all cells is equal to the preferred area $A^{(0)}$ and their perimeter is equal to $L^{(0)}$ is a ground state of the energy. Examples of the ground state in the gray and blue regions are shown as insets. (B) Schematic of energy changes as a function of shear deformation L_x/L_y, for different regimes of the phase diagram.

To study the ground state properties of the model, we consider networks where the parameters

of all cells are identical: $K_\alpha = K$, $\Gamma_\alpha = \Gamma$ and $A_\alpha^{(0)} = A^{(0)}$ for all cells and $\Lambda_{ij} = \Lambda$ for all edges. We will use $K(A^{(0)})^2$ as a unit of energy and $\sqrt{A^{(0)}}$ as a unit of length; dividing both sides of Eq. 2.1 by $K(A^{(0)})^2$, we have a dimensionless work function $f = \mathcal{F}/K(A^{(0)})^2$

$$f = \frac{1}{2}\sum_\alpha (a_\alpha - 1)^2 + \bar{\Lambda}\sum_{\langle i,\, j\rangle} \ell_{ij} + \frac{\bar{\Gamma}}{2}\sum_\alpha \ell_\alpha^2, \tag{2.2}$$

where $a_\alpha = A_\alpha/A^{(0)}$, $\ell_{ij} = L_{ij}/\sqrt{A^{(0)}}$ and $\ell_\alpha = L_\alpha/\sqrt{A^{(0)}}$ are respectively dimensionless area, bond length and perimeter. We are then left with only two free parameters: dimensionless line tension $\bar{\Lambda} = \Lambda/K(A^{(0)})^{3/2}$ and dimensionless contractility $\bar{\Gamma} = \Gamma/KA^{(0)}$. These two parameters then characterize the ground state phase diagram for this simplified model.

We find three different regimes for the ground state of the energy as a function of $\bar{\Lambda}$ and $\bar{\Gamma}$. Parameter regions corresponding to these regimes are shown in Fig. 2.3 A. In the gray region the ground state of the energy is a hexagonal network. In the green region the ground state is degenerate and given by irregular network configurations, for which all cells are six-sided and fulfill the following two constraints:

(i) the area of cells is equal to the preferred area $A^{(0)}$ (or $a_\alpha = 1$).

(ii) their perimeter is equal to a preferred perimeter $L^{(0)} = -\Lambda/2\Gamma$ (or $l_\alpha = -\bar{\Lambda}/2\bar{\Gamma}$).

In the blue region the ground state is also degenerate: any network configuration with arbitrary cell packing and cell shape is a ground state of the energy, given that the area of all cells is equal to $A^{(0)}$ and their perimeter is equal to $L^{(0)}$. An example of such a ground state is shown in Fig. 2.3 A. The striped region on the right-hand side of the phase diagram in Fig. 2.3 A corresponds to a regime where the line tension and perimeter contractility are so high that the ground state is a network with vanishing area. This region is beyond our model in its present form, and can be studied by adding higher order terms of area elasticity to the energy function Eq. 2.1, such as $\bar{K}(A_\alpha - A^{(0)})^4/4$.

2.3   Ground State Phase Transitions

2.3.1   Shear and Bulk Modulus

To have a better understanding about the different regimes of the ground state and phase transitions, we first need to calculate the bulk and shear modulus of the hexagonal network. To simplify the calculations, we introduce a unit box with periodic boundary conditions as shown in Fig. 2.4 A. Repeating this box in the x and y directions, we are able to build an infinite hexagonal lattice. The dimension of the box in x and y directions are L_x and L_y, respectively. The box sizes L_x and L_y are related to the length of the hexagonal network, a: $L_x = \sqrt{3}a$ and
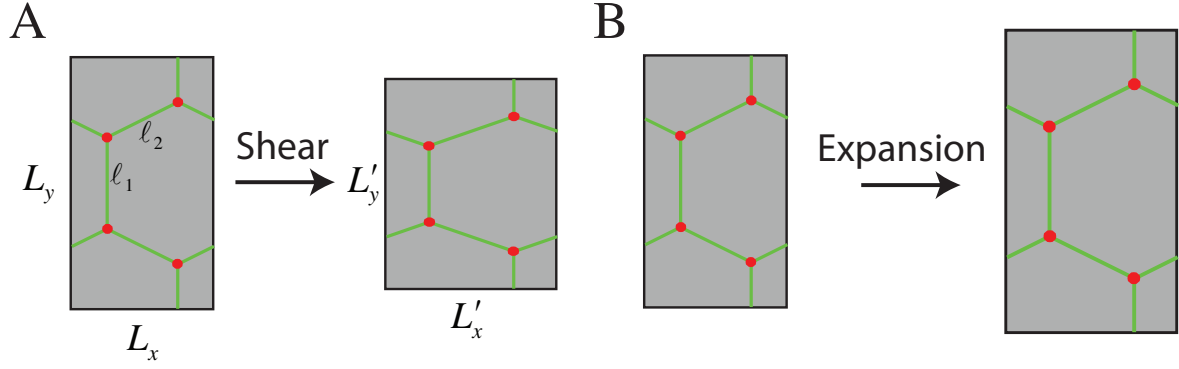
Figure 2.4: Shear and bulk deformations of a hexagonal unit box. An infinite hexagonal network is generated by repeating the unit box in x and y directions. (A) and (B) Schematic of shear deformation and isotropic expansion of the unit box, respectively.

$L_y = 3a$. The energy of the unit box as a function of L_x and L_y is given by

$$
\begin{aligned}
\mathcal{F} &= K\left(\frac{L_x L_y}{2} - A^{(0)}\right)^2 + \Lambda(2l_1 + 4l_2) + \Gamma(2l_1 + 4l_2)^2 \\
&= K\left(\frac{L_x L_y}{2} - A^{(0)}\right)^2 + \Lambda\left(\frac{2L_y}{3} + 2\sqrt{L_x^2 + \left(\frac{L_y}{3}\right)^2}\right) + \Gamma\left(\frac{2L_y}{3} + 2\sqrt{L_x^2 + \left(\frac{L_y}{3}\right)^2}\right)^2,
\end{aligned}
$$
(2.3)

where $\ell_1 = L_y/3$ and $\ell_2 = \sqrt{(L_x/2)^2 + (L_y/6)^2}$ are the length of different sides of the hexagon in Fig. 2.4 A. For an undeformed unit box, $\ell_1 = \ell_2 = a$. However, if we impose an affine deformation, ℓ_1 and ℓ_2 are different.

An affine shear deformation of the unit box is given by $L_x' = L_x(1+\epsilon)$ and $L_y' = L_y/(1+\epsilon)$, where $\epsilon \ll 1$ (see Fig. 2.4). The shear modulus of the hexagonal network is then defined as the second derivative of the energy (2.3) with respect to ϵ

$$
\mu_s = \frac{1}{L_x L_y} \lim_{\epsilon \to 0} \frac{\partial^2 \mathcal{F}(L_x', L_y')}{\partial \epsilon^2}.
$$
(2.4)

The shear modulus μ_s is a function of L_x and L_y. It has a simple form if we rewrite it as a function of a

$$
\mu_s = 12\sqrt{3}\Gamma + \sqrt{3}\Lambda/a.
$$
(2.5)

The bond length a is a function of model parameters K, $A^{(0)}$, Λ and Γ, which is the solution of the minimization of the energy function in Eq. 2.1

$$
\frac{27}{2}Ka^3 + (36\Gamma - 3\sqrt{3}KA^{(0)})a + 3\Lambda = 0.
$$
(2.6)

We can calculate the bulk modulus μ_b, as the second derivative of the work function with respect to ϵ for deformations (see Fig. 2.4 B) $L'_x = L_x(1 + \epsilon)$ and $L'_y = L_y(1 + \epsilon)$. The bulk modulus μ_b as a function of a reads

$$\mu_b = 9\sqrt{3}Ka^2 - 2KA^{(0)} + 8\sqrt{3}\Gamma. \tag{2.7}$$

Along the red line in Fig. 2.3 A, the bulk modulus vanishes and the ground state becomes unstable. Knowing the exact form of the bulk modulus, μ_b, we can derive an analytical expression for the transition line between the solid hexagonal region and the unstable striped region in Fig. 2.3 A. Setting $\mu_b = 0$ in Eq. 2.7, we find an expression for the dimensionless length of a hexagonal network, a_0, with zero bulk modulus: $(24\Gamma - 2\sqrt{3}KA^{(0)})a_0 + 3\Lambda = 0$. Substituting this value of a_0 into Eq. 2.6 we obtain the red boundary line in Fig. 2.3 A

$$\Gamma = \frac{\sqrt{3}}{12}KA^{(0)} - \frac{(9K\Lambda^2)^{\frac{1}{3}}}{8} \qquad \Gamma \leq \frac{\sqrt{3}KA^{(0)}}{12}$$

$$\Lambda = 0 \qquad\qquad\qquad \Gamma > \frac{\sqrt{3}KA^{(0)}}{12}. \tag{2.8}$$

In terms of $\bar{\Lambda}$ and $\bar{\Gamma}$ the boundary line is given by $\bar{\Gamma} = 1/4\sqrt{3} - (3\bar{\Lambda})^{2/3}/8$ (if $\bar{\Gamma} < \sqrt{3}/12$) and $\bar{\Lambda} = 0$ (if $\bar{\Gamma} \geq \sqrt{3}/12$).

2.3.2 Transition from Hexagonal to Soft Networks

The shear modulus of the network decreases for increasing cell-cell adhesion (decreasing Λ). In the gray region shown in Fig. 2.3 A, any shear deformation requires work as shown in Fig. 2.3 B (first panel). In the green region, however, the shear modulus vanishes (see Fig. 2.3 B middle panel). In this region any shear deformation that does not result in changes to the hexagonal packing of the network is admissible at vanishing shear modulus. Further shearing of the network resulting in remodeling of the network requires work. We can calculate an analytical expression for the transition line between the solid gray region of the phase diagram and the semisoft green region. In transition from the solid to the semisoft region, the shear modulus is zero for limited deformations around the perfect hexagonal network. We find $\mu_s = 0$ for $a_0 = -\Lambda/12\Gamma$. Substituting this value of a_0 in Eq. 2.6 gives us the transition line from the gray to the green region in Fig. 2.3 A: $\bar{\Gamma} = -\bar{\Lambda}/\sqrt{32\sqrt{3}}$.

In the blue region in Fig. 2.3 A, the network is soft and large deformations at vanishing shear modulus are admissible. These large deformations consist both of cell shape changes and remodeling of cell boundaries. The latter deformations require the boundaries to shrink to zero and expand in the opposite direction (at vanishing shear modulus) resulting in local changes of cell neighbors, and allowing the network to shear to any extent. As we discussed in Sec. 2.2 the area and perimeter of cells in the green and blue regions are respectively equal to the preferred

area $A^{(0)}$ and preferred perimeter $L^{(0)}$. For a network with $\ell_1 = 0$ (see Fig. 2.4 A), i.e., the ground state of the energy in the blue region, the area and perimeter of a cell are

$$A_\alpha = A^{(0)} = \frac{L_x L_y}{2},$$
$$L_\alpha = L^{(0)} = -\frac{\Lambda}{2\Gamma} = 2\sqrt{L_x^2 + L_y^2}. \tag{2.9}$$

The condition to have positive real solutions for L_x and L_y implies that $L^{(0)} \geq 4\sqrt{A^{(0)}}$ or $\bar{\Gamma} \leq -\bar{\Lambda}/8$, which gives the transition line between the green and blue regions in Fig. 2.3 A.

2.4 Summary

One advantage of using epithelia as model systems in biology lies with their great simplicity compared to three-dimensional tissues. Epithelial cells are connected to each other via adhesive molecules and establish a junctional adheren network near their apical region. In this chapter we develop a two-dimensional vertex model to study the mechanics of the junctional network. In this model each cell is approximated by a polygon (vertices connected by straight bonds). On time scales shorter than the time scale of cell division and longer than that of local perturbations, the junctional network is stable and the total force on each vertex is zero. These forces, which are due to cell mechanics and cell-cell interactions along cell boundaries, can be calculated using a work function (Eq. 2.1). We introduce two dimensionless parameters, $\bar{\Lambda}$ and $\bar{\Gamma}$, to characterize the ground states of the model. We find that there exist three phases as a function of model parameters. In the gray region in Fig. 2.3 A, the ground state is a non-degenerate hexagonal network. However, in the green and blue regions the ground state is degenerate. In the green region, the ground states are networks with hexagonal packing such that the area of all cells is equal to the preferred area $A^{(0)}$ and their perimeter is equal to the preferred perimeter $L^{(0)}$. In the blue region ground states fulfill these two conditions on area and perimeter of cells, with the difference being that the ground state can acquire any packing.

We calculate the bulk and shear modulus of the network using a unit box shown in Fig 2.4. For all parameter values for which the bulk modulus vanishes (for high line tension and contractility), the model breaks down and the network becomes unstable (see striped region in Fig. 2.3 A). For decreasing line tension, the shear modulus of the network decreases. In the green region, the shear modulus vanishes for limited shear deformations while in the blue region, the shear modulus vanishes for any shear deformation. We calculate analytical expressions for the transition line between the gray and green regions. We find that for $-\bar{\Lambda}/8 < \bar{\Gamma} \leq -\bar{\Lambda}/\sqrt{32\sqrt{3}}$ the network is semisoft while for $\bar{\Gamma} \leq -\bar{\Lambda}/8$, the network is soft. To shear the network in the blue region to any extent, remodeling of cell boundaries is required such that a boundary shrinks to zero and expands in the opposite direction. The transition line between the green and blue regions is calculated in a similar fashion.

3 Dynamics of Tissue Growth
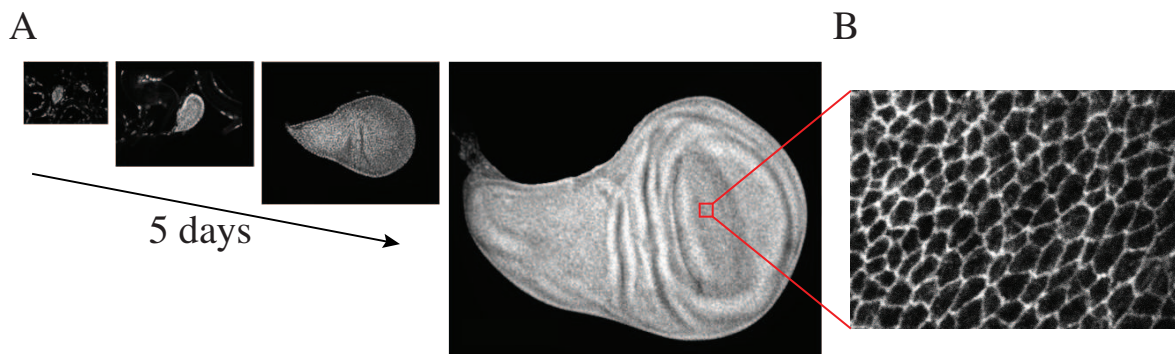
Figure 3.1: Different stages of development of the wing disc of the fruit fly *Drosophila*. (A) Starting with a few cells (~ 50), the epithelia grows in five days to the size of $\sim 50,000$ cells (provided by O. Wartlick). (B) A small portion of the tissue at higher magnification showing cell boundaries (provided by [3]).

Most epithelia develop from a few cells to their final size by cell division (proliferation). We show in Fig. 3.1 A an example of the development of the wing disc of the fruit fly *Drosophila*. The wing epithelia starts from about 50 cells and it grows to roughly $50,000$ cells within five days. Each divides cell on average about 10 times. Spatial patterns of gene expression are set up in the tissue to control growth, packing and morphologies of the epithelia. Although cell division and cell rearrangement happens frequently during growth, the packing geometry of the tissue is highly reproducible, indicating that the underlying mechanisms controlling cell packing and cell shapes in tissue are robust.

In the previous chapter, we introduced a vertex model to describe cell mechanics and cell interactions in two-dimensional tissues. To study how proliferation affects the pattern of the packing geometry of cells in tissues, we introduce cell division in our vertex model. We simulate growth of a tissue starting from a few cells up to a large size. Cell division leads to local rearrangements of the network. This involves changes to the relationship of neighboring cells. We investigate how packing geometry evolves in a growing network. We also study the effect of adhesion and cell contractility on the packing patterns of cells in growing epithelia. We show

that cell division, together with cell mechanics and cell adhesion, control the pattern of cells in tissues. We then study the phase transitions discussed in the previous chapter for growing tissues, and show that there exists a phase transition for non-equilibrium growing networks. Cell division induces local stresses which can relax through the network via neighboring cell shape changes, as well as via the remodeling of cell boundaries. We specifically study how bond remodeling is affected by a local perturbation, such as a cell division, and also how cell mechanics might influence the spatial distribution of remodeling around a dividing cell. Motivated by laser ablation experiments to cut a boundary in the epithelia, we study in our vertex model the displacements that are generated by removing a cell boundary from the network. We show that this perturbation generates anisotropic displacements around the removed boundary, and that the movements are strongly coupled to tissue mechanics.

## 3.1   Cell Division in the Vertex Model

Inhomogeneity in the packing geometry of tissues is generated by three topological changes: cell division, cell disappearance and junctional remodeling. Cell division adds a new cell, and consequently two new vertices to the network (see Fig. 3.2 A). We define a T1 transition as the shrinkage of a cell boundary and the expansion in the opposite direction, which changes the neighbor number relation of surrounding cells (see Fig. 3.2 B). After a T1 transition, the neighbor numbers of the two cells sharing the boundary before the process decrease by one, while the other two cells gain one boundary. A T2 transition describes the situation when a triangle shrinks to a point (see Fig. 3.2 C). This process decreases the number of cells in the epithelia by one and the number of vertices by two. An unstable n-sided cell, goes through a series of T1 transitions until it becomes a triangle. This triangular cell is then replaced by a vertex through a T2 transition. A schematic of these three mechanisms is shown in Fig. 3.2 A-C.

The elastic response of cells typically occurs on time scales of seconds to a few minutes ([20] and [21]). Most morphogenetic processes such as cell division and cell rearrangement develop on longer time scales compared to cell shape relaxation. Therefore the junctional network of cells can be assumed to be a stable and stationary configuration on larger time scales than those associated with cell shape relaxation. We think of a developing epithelium as a sequence of stable network configurations which undergo rearrangements in response to local perturbations affecting the stable configuration. Such perturbations include cell division and apoptosis (cell death), but might also correspond to slow changes in cellular properties. This quasistatic approximation allows us to define a history of stable configurations by slowly and locally modifying model parameters. Thus, a particular packing geometry is the consequence of the history of such perturbations. By using our model, we can numerically simulate the evolution of cell
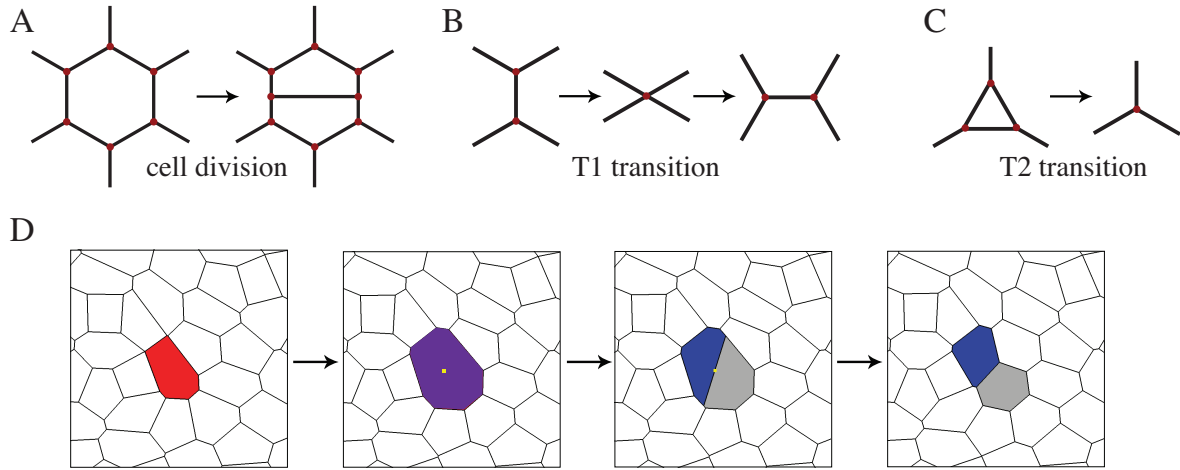
Figure 3.2: Topological rearrangements in vertex model. (A) Schematic of cell division: Two new vertices and a new boundary are added to the network, changing the neighbor number of surrounding cells. (B) T1 transition: A boundary shrinks to zero length and expands in the opposite direction. This changes the neighbor relationship of the surrounding cells. (C) T2 transition: If the area of a triangle vanishes, it is replaced by a vertex. (D) Cell division in the vertex model. The preferred area of a dividing cell is increased quasistatically. A new bond is introduced with a random orientation. Both new cells are assigned the initial preferred area, and the resulting network is relaxed. The yellow dot indicates the center of the original cell through which the new boundary is initially formed.

packing geometry during tissue growth. We randomly select one cell and divide it by the following algorithm: we double the preferred area of the cell quasistatically while relaxing the energy functional with a conjugate gradient method (for details see App. A; see Fig. 3.2 D, first and second panels). After its size is doubled, the cell is divided by generating a new edge at a random angle that passes through the cell center (see Fig. 3.2 D, third panel). Here the cell center is defined as the average of the vertex positions of the cell: $\mathbf{C} = (\sum_{i=1}^{n} \mathbf{R}_i)/n$ where n is the number of vertices of the cell. The two daughter cells that are created by this procedure are assigned the parameters of the other cells, including the preferred area $A^{(0)}$. The new boundary also receives the same tension Λ as other boundaries. The resulting configuration is then relaxed to the nearest stable configuration (see Fig. 3.2 D, fourth panel). Repeating this algorithm, we can start from a small number of cells and grow the tissue to any cell number.
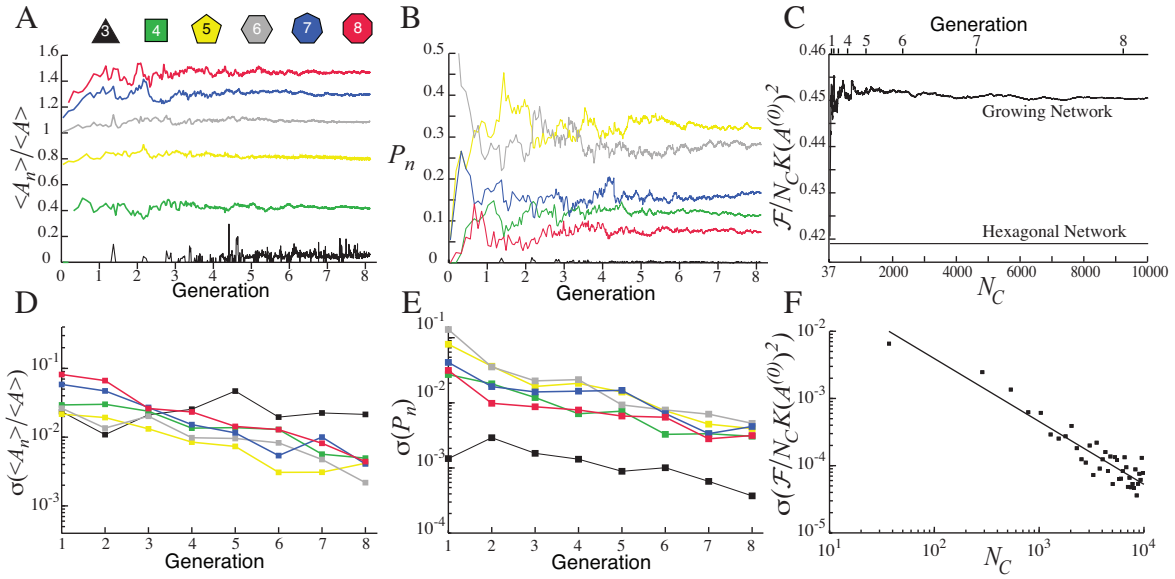
Figure 3.3: Evolution of topology and morphology of a growing tissue. (A) Average area of n sided cells $\langle A_n \rangle$ relative to the average area $\langle A \rangle$ of all cells as a function of generation number. (B) Fraction P_n of cells with n neighbors as a function of generation number in a growing network for case I ($\bar{\Lambda} = 0.12$, $\bar{\Gamma} = 0.04$). (C) Normalized energy per cell of a growing network as a function of the number N_C of cells, for parameter values corresponding to case I, generation number is also indicated. The energy approaches a value greater than the ground-state value of the hexagonal network. (D) Logarithmic plot of standard deviation of $\langle A_n \rangle / \langle A \rangle$ as a function of generation number for the simulation of case I. (E) Logarithmic plot of standard deviation of the frequency of n-sided polygons, $\sigma(P_n)$ as a function of generation number for the simulation of case I. (F) The standard deviation of the energy per cell, averaged over 250 individual divisions as a function of cell number.

3.2 Simulation of Tissue Growth

Starting with a few hexagonally packed cells as an initial configuration, we can simulate tissue growth by dividing randomly selected cells using the algorithm described in Sec. 3.1. During this process, a distinct network pattern emerges that can be characterized by the fraction P_n of cells of different polygon classes (i.e., cells with different numbers of neighbors, n) and by the average areas A_n of n-sided cells. For increasing number of cells, the fraction P_n of n-sided cells, and their average area A_n converge to constant values. In Fig. 3.3 A and B we show the normalized average area $\langle A_n \rangle / \langle A \rangle$ and the distribution P_n for different classes of polygons as a function of generation number, respectively. Here $\langle A \rangle$ indicates the average area of all cells in the tissue. We use different colors for different classes of polygons according to

their neighbor number, n and we use the model parameter values $\overline{\Lambda} = 0.12$ and $\overline{\Gamma} = 0.04$. A representative network grown with these parameter values is shown in Fig. 3.4 A; each cell is colored according to its neighbor number using the same color coding as in Fig. 3.3 A.

In Fig. 3.3 D and E, we show the standard deviations $\sigma(\langle A_n \rangle / \langle A \rangle)$ and $\sigma(P_n)$ of both the area and the fraction of n-sided cells, respectively, which decrease exponentially with generation number. The decay generation time for P_n and A_n are 3.14 and 3.60, respectively. Beyond the larger of these characteristic generation numbers, the tissue patterns become stationary for increasing generation number. After simulating approximately eight generations of cell division (from 36 to $10,000$ cells), the standard deviations $\sigma(P_n)$ and $\sigma(A_n)$ are less than 1%. We also show in Fig. 3.3 C the normalized energy per cell, $\mathcal{F}/N_C K (A^{(0)})^2$ of a growing tissue. The energy per cell first increases with increasing cell number and then fluctuates around a constant value that is larger than the ground-state value of the hexagonal lattice. In Fig. 3.3 F, we show the standard deviation of the energy per cell, $\sigma(\mathcal{F}/N_C K (A^{(0)})^2)$. The standard deviation of the energy density also decays exponentially with cell number. This indicates that the grown tissue is trapped in a local minimum and fluctuations resulting from cell division cannot change the statistical properties of the tissue. By using such an algorithm, we can generate a distinct pattern of cells and characterize them by measuring the stationary values of two sets of numbers: P_n, the fraction of n-sided cells, which is a measure of packing inhomogeneity, and $\langle A_n \rangle / \langle A \rangle$, the average area of n-sided cells normalized by the average area of all cells in the tissue; the latter quantity is a measure of cellular geometry in tissues.

3.3   Statistics of Cell Packing Geometries

In order to study how tissue morphology is influenced by the physical properties of cells, we performed growth simulations by systematically varying parameter values. In addition to case I ($\overline{\Lambda} = 0.12$ and $\overline{\Gamma} = 0.04$), we performed simulations for two more cases. In case II ($\overline{\Lambda} = 0$, $\overline{\Gamma} = 0.1$) contractility is large relative to area elasticity, and the ground state is a hexagonal network, as it is in case I. For case III ($\overline{\Lambda} = -0.85$, $\overline{\Gamma} = 0.1$) line tension is negative, and the ground state corresponds to soft networks (see Fig. 2.3 A). Representative networks illustrating the stationary state for case I, II and III are shown in Fig. 3.4 A, B and C, respectively (colors as in Fig. 3.4 D-I). For these three cases, we start from 36 hexagonally packed cells and grow the tissue for ~ 8 generations ($10,000$ cells). We then calculate the stationary values of packing geometry and tissue morphology as their average values over the last 250 cell divisions (see Sec. 3.2). These specific parameter values corresponding to case I are chosen in order to compare with experiments. We will discuss in Chap. 6 that for these parameter values, the packing geometry and tissue morphology in simulations match best with those observed in the *Drosophila* wing disc.
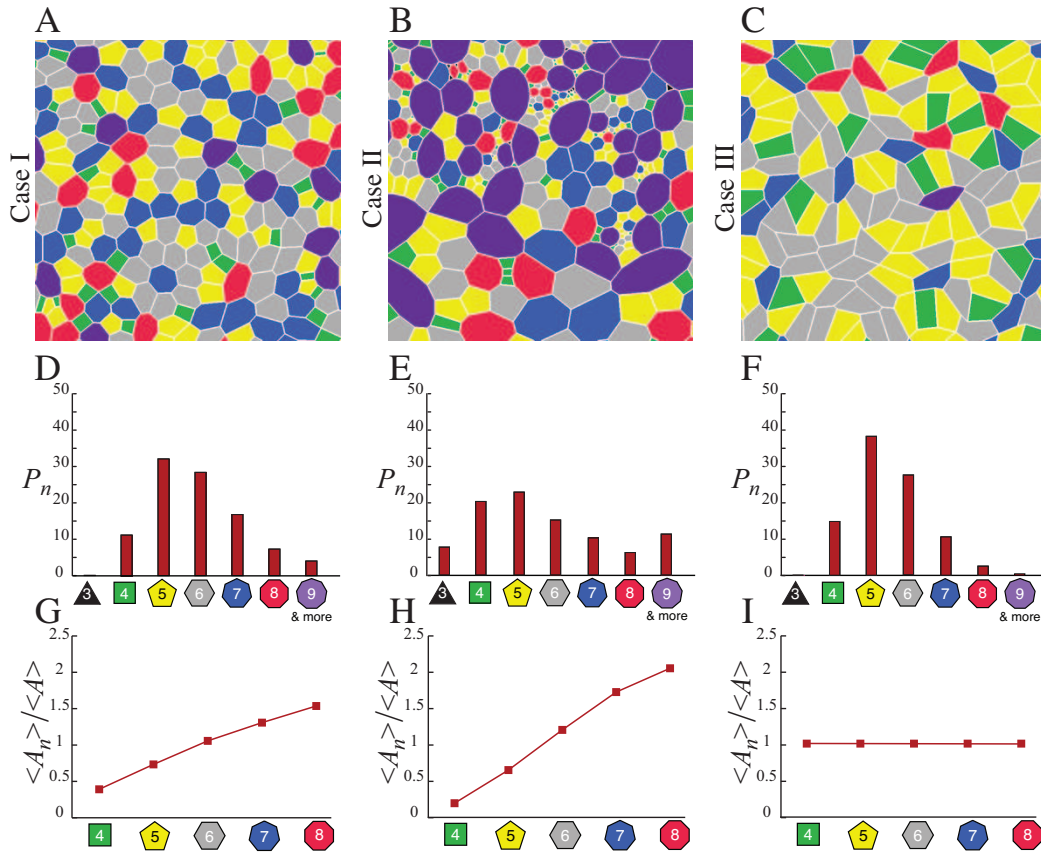
Figure 3.4: Examples of different tissue morphologies. (A)-(C) Examples of stationary network patterns generated by repeated cell division for cases I, II, and III, respectively (case I: $\bar{\Lambda} = 0.12$, $\bar{\Gamma} = 0.04$, case II: $\bar{\Lambda} = 0$, $\bar{\Gamma} = 0.1$, case III: $\bar{\Lambda} = -0.85$, $\bar{\Gamma} = 0.1$). Color code for polygon class is indicated below panels D-I. (D)-(F) Stationary distributions of neighbor numbers P_n for cases I, II, and III. (G)-(I) Average areas of different polygon classes normalized to the average area of cells in the network, $\langle A_n \rangle / \langle A \rangle$, for cases I, II, and III.

To accurately compare theory with experiment we need to slightly modify the above method of quantifying packing geometry. In our simulations all vertices are three-fold vertices: they are connected to three neighboring vertices. In experiment, however, instrumental resolution renders cell boundaries shorter than 20% of the average bond length invisible. Therefore two three-fold vertices that are closer than this distance are seen in experiment as a single four-fold vertex. To mimic this effect in our simulations, after we grow the tissue we replace those vertices that are closer than 20% of the average bond length by a single four-fold vertex, without any further energy minimization; this correction can slightly modify cell packing and tissue morphology.

We present the stationary values of P_n for cases I-III in Fig. 3.4 D-F. For case I, pentagons

form the most common polygon class (see Fig. 3.4 D), and the average neighbor number $\langle n \rangle = \sum_3^\infty n P_n = 5.9$. This implies that 2.44% four-fold vertices exist, which we can estimate using the following method. Using Euler's theorem for polygons covering a two-dimensional manifold, the number of vertices, V, number of edges, E and number of cells, C are related such that $C - E + V = \chi$, where χ is the Euler-Poincaré characteristic of the manifold. For an infinite plane, $\chi = 0$. For a network that includes three- and four-fold vertices ($V = V_3 + V_4$), the number of edges and the number of cells are given by

$$E = \frac{3V_3}{2} + 2V_4$$
$$C = E - V = \frac{V_3}{2} + V_4, \tag{3.1}$$

where V_3 and V_4 are the numbers of three-fold and four-fold vertices, respectively. Therefore the average neighbor number $\langle n \rangle$ is given by

$$\langle n \rangle = \frac{2E}{C} = \frac{6 + 8\alpha}{1 + 2\alpha}, \tag{3.2}$$

where $\alpha = V_4/V_3$ is the fraction of four-fold to three-fold vertices. For a small fraction of four-fold vertices ($V_4 \ll V$), the average neighbor number is $\langle n \rangle \simeq 6 - 4\alpha$, which implies that $V_4/V = (6 - \langle n \rangle)/(10 - \langle n \rangle)$.

As in case I described in Sec. 3.2, the fractions P_n of polygon classes also converge during growth simulations for cases II and III. The resulting network morphologies, however, differ dramatically (compare Fig. 3.4 A, B and C). In case II (see Fig. 3.4 E), the stationary network contains a smaller fraction of hexagonal cells than in case I (see Fig. 3.4 D). Pentagons are most common in this case. However, there is also a large fraction of cells with nine or more sides – even 20 sided polygons occur. In case III, the coefficients $\overline{\Gamma}$ and $\overline{\Lambda}$ are such that the ground state is a soft network (see Fig. 2.3 A). Under these conditions, simulating proliferation generates the stationary network morphology shown in Fig. 3.4 C. Pentagons form the most common polygon class, and the fraction of cells with a large number of neighbors is smaller than in cases I and II (see Fig. 3.4 F).

In addition to the topological disorder reflected in the fractions P_n of polygon classes, cells are geometrically disordered in these three cases. For case I, the average area A_n increases for increasing n as shown in Fig. 3.4 G. However, for case II, the average areas A_n (see Fig. 3.4 H) vary more strongly with neighbor number than in case I. In case III all polygons have the same area $A^{(0)}$ and the same perimeter $L^{(0)} = -\Lambda/2\Gamma$. As a consequence, the cell area does not depend on neighbor number n as shown in Fig. 3.4 I. The average neighbor number, $\langle n \rangle$, also varies for these three cases. For case II: $\langle n \rangle = 5.95$, while for case III: $\langle n \rangle = 5.46$, which indicates that the number of four-fold vertices in case III (by Eq. 3.2) is roughly 10 times greater than the number of four-fold vertices in case II (case II: 1.23%, case III: 11.89%). These results

show that cell proliferation can generate packing disorder with specific reproducible features that depend on the physical properties of the cells, as described by model parameters $\bar{\Gamma}$ and $\bar{\Lambda}$.

3.4 Phase Transitions in Tissue Growth
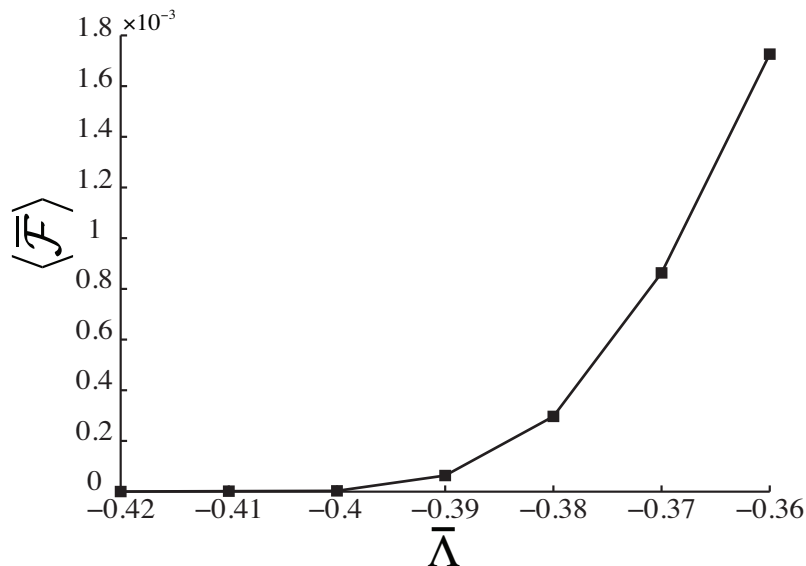
Figure 3.5: Phase transitions for growing tissues. The converged value of the order parameter plotted as a function of dimensionless line tension $\bar{\Lambda}$ ($\bar{\Gamma} = 0.05$). The order parameter vanishes for $\bar{\Lambda} \leq -0.4$.

We discussed in Sec. 2.3 that there exists a phase transition from solid to semisoft networks followed by a transition to soft networks, when varying the line tension $\bar{\Lambda}$. Using a series of analytic arguments, we calculate the transition line between these three regimes. We also introduced in Sec. 3.2 an algorithm to generate irregular packing geometries using repeated cell division and junctional rearrangements. We now investigate phase transitions for non-equilibrium networks, such as growing ones. In order to study phase transitions in growing networks, we first need to define an order parameter. We define an order parameter, $\bar{\mathcal{F}}$, as the dimensionless energy density: $\bar{\mathcal{F}} = \mathcal{F}(\mathbf{R}_i)/N_C - \Lambda^2/8\Gamma$. Since our order parameter is equal to the energy density, as we discussed in Sec. 3.2, it fluctuates for the first few generations of cell proliferation and then converges to a well-defined value, depending on parameter values. The order parameter $\bar{\mathcal{F}}$ vanishes for those network configurations for which all cells have area equal to their preferred area $A^{(0)}$, and those for which all cells have a perimeter equal to the preferred perimeter $L^{(0)} = -\Lambda/2\Gamma$.

To study a potential phase transition we simulate tissue growth for different values of the line tension $\bar{\Lambda}$, keeping the contractility constant ($\bar{\Gamma} = 0.05$). For each set of parameters, we

start from 36 hexagonally packed cells and grow the tissue up to $10,000$ cells. We calculate the average value of the order parameter, $\langle\bar{\mathcal{F}}\rangle$, over the last 250 cell divisions. In Fig. 3.5, we plot the average value of the order parameter, as a function of dimensionless line tension. The average order parameter vanishes for $\bar{\Lambda} \leq -0.4$. We repeat these simulations for different sets of parameter values $(\bar{\Lambda}, \bar{\Gamma})$ and we find that the transition occurs at $\bar{\Gamma} \simeq -\bar{\Lambda}/8$ for $\bar{\Gamma} = 0.01, 0.03, 0.05, 0.07$ and 0.09. However the actual value of $\langle\bar{\mathcal{F}}\rangle$ depends on the accuracy of our energy minimization algorithm. As we described before, we use a conjugate gradient method to calculate the local minimum of the energy function. The algorithm (App. A) searches for a local minimum of the energy function for a given set of variables, and stops if the change in the energy function for two search steps falls below a certain threshold ϵ. Therefore the actual value of the energy density, and consequently the value of the order parameter, depends on the relaxation threshold ϵ. To study if minimization with higher accuracy changes the transition line, we repeat these simulations for the same set of parameter values $(\bar{\Lambda},\ \bar{\Gamma})$ and for different values of ϵ. In Fig. C.1 we plot the logarithm of the average value of the order parameter as a function of the logarithm of ϵ for different sets of parameter value $\bar{\Lambda}$ (given $\bar{\Gamma} = 0.05$). For $\bar{\Lambda} > -0.4$, decreasing the threshold does not change the average value of the order parameter, while for $\bar{\Lambda} \leq -0.4$ this value converges to zero as we decrease ϵ. Our numerical analysis strongly suggests that there is a phase transition from solid to soft networks for growing tissues and that the transition line falls on the line we calculated for the ground state phase transition in Sec. 2.3.

3.5   Junctional Remodeling

As discussed in Sec. 3.1 our cell division algorithm includes a growing phase of the dividing cell and a relaxation phase after division. In the growing phase, we increase the preferred area of the cell to two times the normal value quasistatically in a few steps. After each increment in the preferred area, the tissue is relaxed to its nearest local minimum. When the size of the dividing cell has doubled, we introduce a new boundary at a random angle and relax the tissue. In both phases, local stresses arise in the tissue. These stresses are then relaxed by cell shape changes as well as cell bond remodeling (T1 transitions). It is also possible that a cell disappears from the network during tissue relaxation (T2 transitions). The induced patterns of stress in the network due to cell division depends on the mechanical properties of cells. Here we study statistics and pattern of T1 and T2 transitions for a growing network for three cases. These cases have the same perimeter contractility ($\bar{\Gamma} = 0.05$) but different line tensions ($\bar{\Lambda} = -0.41,\ 0.1,$ and 0.16). The first case corresponds to the soft networks regime (see Fig. 2.3 A), while the other two cases correspond to the solid regime. For the third case ($\bar{\Lambda} = 0.16$), the bulk modulus is significantly smaller than the other two cases. Although the cases I-III introduced in Sec. 3.3 have similar

mechanical behavior, here we restrict ourself to variations in only one parameter (line tension).

For each case, we start from 36 hexagonally packed cells and grow the tissue up to $10,000$ cells, recording the statistics of T1 and T2 transitions during growth. During a single cell division a few topological transitions (T1 and/or T2) occur. The number of T1 transitions per 100 cell divisions, f_{T1}, is then defined as

$$f_{T1} = \sum_{n=0}^{\infty} n p_n, \tag{3.3}$$

where p_n is the probability of having n junctional remodelings after a cell division. In Fig. 3.6 A, we show f_{T1} for the case $\bar{\Lambda} = -0.41$ as a function of the total cell number. After the first few generations, the number of T1 transitions converges to a well-defined value. Although f_{T1} fluctuates for larger numbers of cell divisions, it is significantly different for different sets of parameter values. In Fig. 3.6 B we show the converged value of the rate of T1 transitions, $\langle f_{T1} \rangle$, for these three cases. For $\bar{\Lambda} = -0.41$, $\langle f_{T1} \rangle$ is greater than the other two cases. In the soft network regime ($\bar{\Lambda} = -0.41$), T1 transitions are possible without work being done. However, for the other two cases the network is solid and there is a barrier for T1 transitions. This is a possible explanation for the different rates observed for these three cases.

We define the number of T2 transitions per 100 cell divisions, f_{T2}, as in Eq. 3.3: $f_{T2} = \sum_{n=0}^{\infty} n p_n$, where p_n is the probability of having n T2 transitions after a cell division. In Fig. 3.6 C we show f_{T2} as a function of cell number N_C for $\bar{\Lambda} = 0.16$. Similar to the number of T1 transitions, f_{T2} also converges to a value for larger number of cell divisions. We plot the average value of f_{T2} for different cases. For the soft networks the number of T2 transitions is almost zero ($f_{T2} = 3.92 \times 10^{-4} \pm 2.77 \times 10^{-4}$). However, for more positive values of $\bar{\Lambda}$, the number of T2 transitions, f_{T2}, increases significantly. For $\bar{\Lambda} = 0.16$ it increases up to 0.58 and half of the cells eliminates from the tissue during growth. We conclude that topological rearrangements induced by cell divisions, does depends on the mechanical properties of the cells. The number of T1 transitions is higher for networks with lower shear modulus and the number of T2 transitions is higher for networks with lower bulk modulus.

To test the validity of this idea, we systematically change the parameter value $\bar{\Lambda}$ from -0.41 to 0.16. For each case we grow the tissue up to $10,000$ cells and quantify the average number of T1 and T2 transitions. In Fig. 3.7 A and B, we plot these averages as a function of $\bar{\Lambda}$. The number of T1 transitions increases by a factor of 10 for decreasing $\bar{\Lambda}$. Up to $\bar{\Lambda} = -0.38$, the average number of T1 transitions increases smoothly and converges to $\langle f_{T1} \rangle \simeq 0.6$. However, for smaller value of $\bar{\Lambda}$, the number of T1 transitions changes abruptly and attains its maximum value. Interestingly, this value of $\bar{\Lambda}$, for which abrupt changes in the number of T1 transitions occur, coincides with the phase transition from the semisoft to the soft regimes (see Fig. 2.3 A). The average number of T2 transitions changes more strongly as a function of $\bar{\Lambda}$. For $\bar{\Lambda} < 0.04$, the average number of T2 transitions is negligible. However it increases strongly for higher
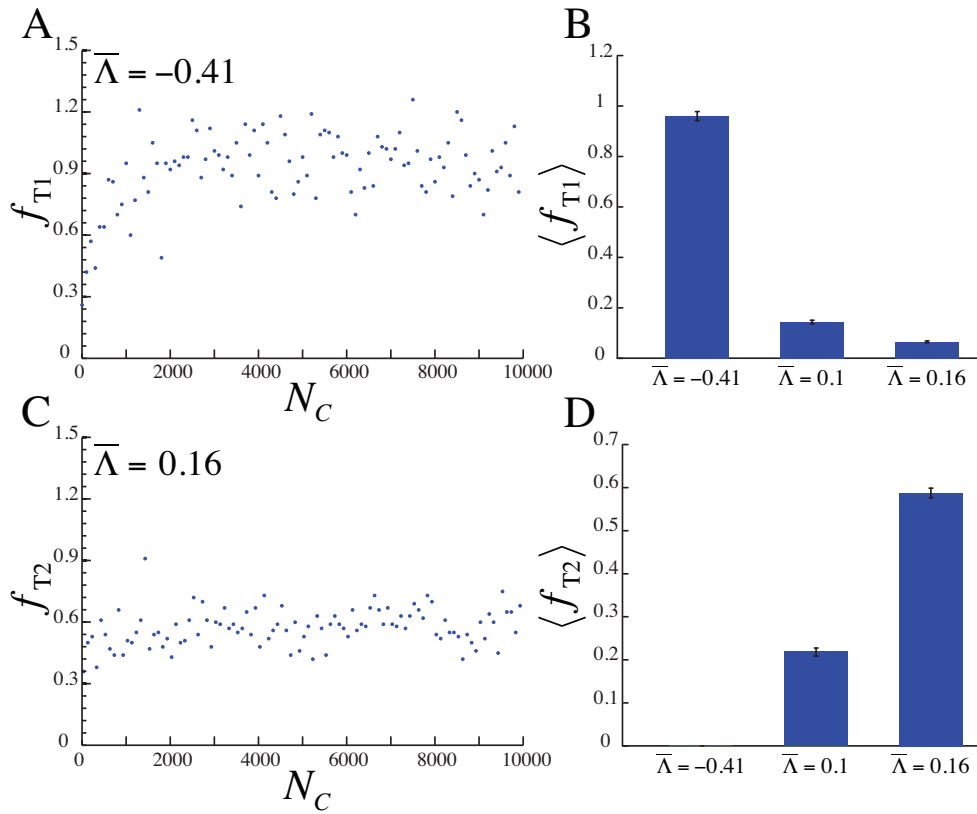
Figure 3.6: (A) Number of T1 transitions per 100 cell divisions for a growing tissue for parameter values ($\bar{\Lambda} = -0.41$, $\bar{\Gamma} = 0.05$) as a function of cell number N_C. (B) The converged value of f_{T1} for three different cases of line tension. (C) Number of T2 transitions per 100 cell divisions for a growing tissue for ($\bar{\Lambda} = 0.16$, $\bar{\Gamma} = 0.05$) as a function of cell number N_C. (D) Average value of f_{T2} for proliferating networks with different line tension.

values of $\bar{\Lambda}$ up to 0.58 for $\bar{\Lambda} = 0.16$.

3.6   Tissue Relaxation due to Local Perturbations

As we will discuss in Sec. 6.2, to investigate the interplay of forces acting at the junctional network of epithelial cells in the wing disc of *Drosophila*, we perturbed this stable junctional network by ablating a section of individual cell boundaries with a UV laser beam. In response to the cut, E-cadherin-GFP fluorescence, which is used to mark the junctional network, disappeared from the center of the cut cell boundary, and the vertices at both ends moved from their initial positions. The vertices subsequently relaxed to new stable positions. Here we study theoretically the model behavior due to local perturbations such as removal of a cell boundary. We will term this process as "laser ablation" and the removed bond as the "cut bond" in our
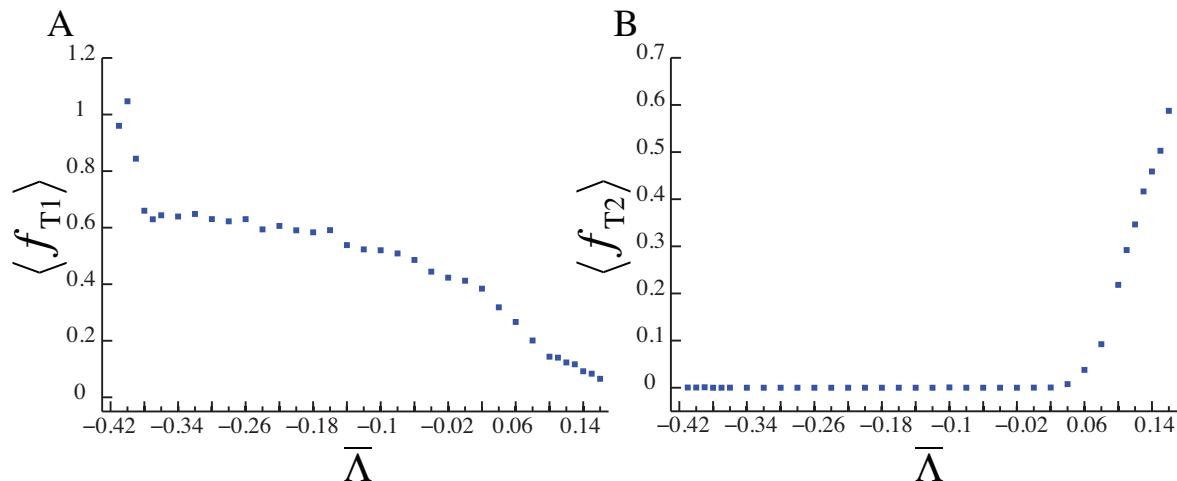
Figure 3.7: (A) Average number of T1 transitions as a function of line tension $\bar{\Lambda}$ for growing tissues ($\bar{\Gamma} = 0.05$). The number of T1 transitions increases for decreasing line tension and there are sharp changes near the transition line between the semisoft and soft regimes of the ground state phase diagram. (B) Average number of T2 transitions as a function of $\bar{\Lambda}$.

theoretical study.

In experiment, we could not say *a priori* that laser ablation affected only localized line tension of cell boundaries, or whether perimeter contractility was affected as well. Thus one can imagine two scenarios to mimic bond cutting experiments. In the first scenario, we assume that laser ablation only affects the tension of the ablated boundary. In the second scenario we assume that both the tension in the ablated boundary and the contractility of the two cells adjacent to the cut boundary is affected by ablation. These two scenarios generate different types of displacements in the vertices surrounding the cut boundary. Removing contractility of the two cells sharing the cut bond would be expected to result in isotropic expansion of these two cells, whereas removing bond tension of the cut bond is expected to produce anisotropic deformations of the cells adjacent to the cut bond. In the idealized case of a perfectly isotropic deformation, the perimeter would increase linearly with an increase in length of the cut bond. In contrast, a strongly anisotropic deformation would result in little or no changes in the perimeter of the two cells sharing the cut bond. Real deformations might comprise a superposition of both anisotropic and isotropic movements. The measurements of changes in the combined area, ΔA_{cut}, and combined perimeter, ΔL_{cut}, of the two cells adjacent to the cut boundary can be used as a measure of anisotropy of the displacements, and therefore can distinguish between these two scenarios. We will discuss in Sec. 6.2 which scenario can best generate the observed displacements in experiments.

To simulate laser ablation, we select bonds for removal and we set to zero the normalized line
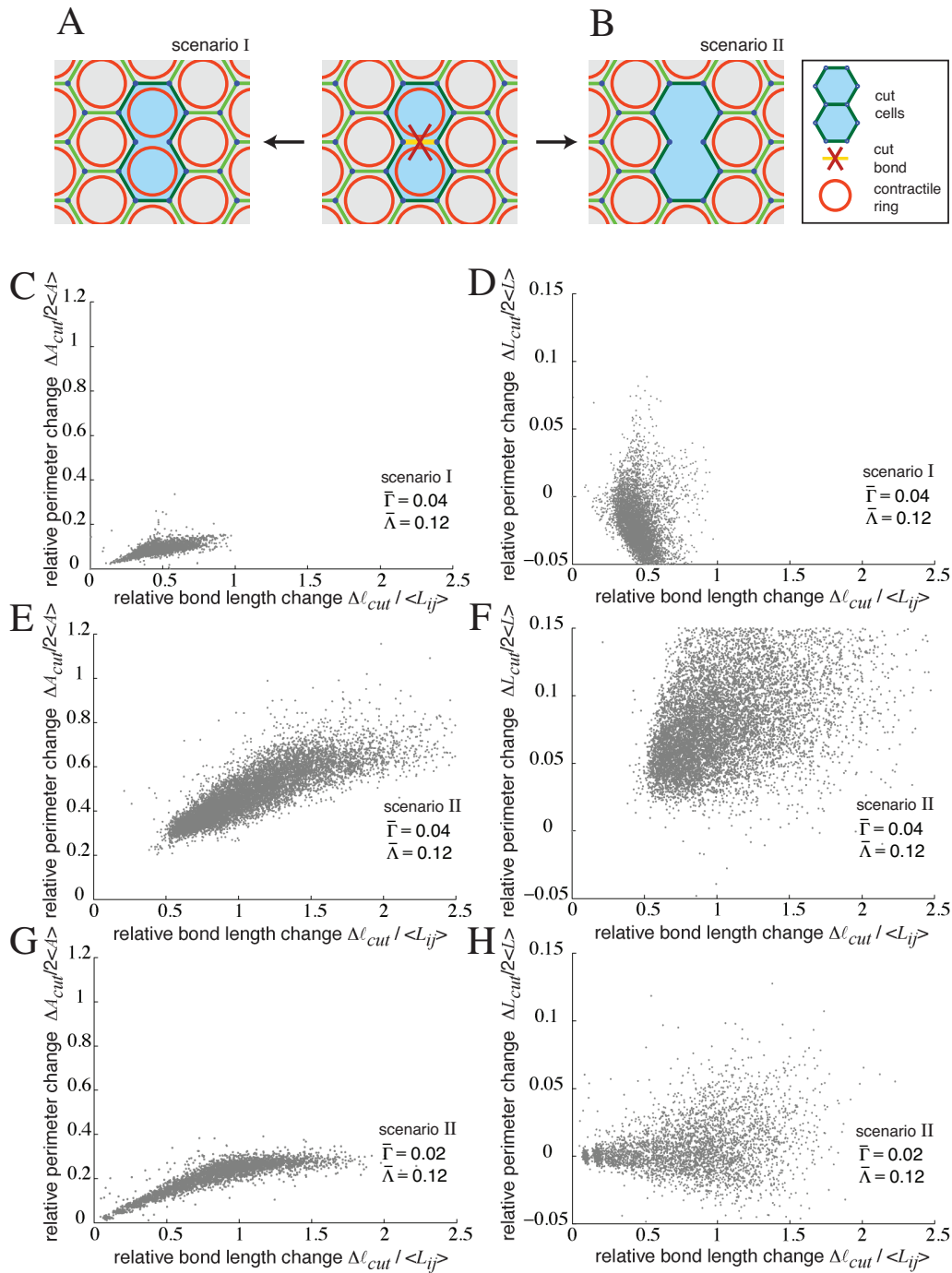
Figure 3.8: Laser ablation in two different scenarios. (A) and (B) In scenario I, ablation is simulated by setting only $\overline{\Lambda}_{ij} = 0$ for the cut bond. In scenario II, ablation is simulated by setting both $\overline{\Lambda}_{ij} = 0$ and also $\overline{\Gamma}_\alpha = 0$ for the two cells adjacent to the cut boundary. (C) and (E) Relative combined area change of cells adjacent to the cut boundary as a function of relative bond length increase for scenarios I and II (for parameter values corresponding to case I). (D) and (F) Relative combined perimeter change of cells adjacent to the cut boundary as a function of relative bond length increase for scenario I and II (for parameter values corresponding to case I). (G) and (H) Relative area and perimeter changes for the case ($\overline{\Lambda} = 0.12, \overline{\Gamma} = 0.02$) in scenario II.

tension $\bar{\Lambda}_{ij}$ of the cut bond for scenario I (see Fig. 3.8 A) and both $\bar{\Lambda}_{ij}$ and the normalized contractility $\bar{\Gamma}_\alpha$ of the two cells sharing the cut bond for scenario II (see Fig. 3.8 B). We start from a stable network configuration generated by a growth algorithm for parameter values corresponding to case I in Sec. 3.3 ($\bar{\Lambda} = 0.12, \bar{\Gamma} = 0.04$). Randomly selecting a boundary for ablation, we quasistatically decrease $\bar{\Lambda}_{ij}$ and/or $\bar{\Gamma}_\alpha$ of the cut boundary in few steps, while relaxing the networks using the conjugate gradient method. For the given pair of parameters $\bar{\Gamma}$ and $\bar{\Lambda}$ for all other cells, we determine the resulting distributions of area and perimeter changes of the pair of cells sharing the removed bonds. In Fig. 3.8 C-F, we show this distribution of the combined area changes, ΔA_{cut} normalized to the average area of all cells and combined perimeter changes, ΔL_{cut}, normalized to the average bond length as a function of normalized bond length increase, for scenario I and II respectively. Our analysis shows that the combined area changes, ΔA_{cut}, vary more strongly in scenario II than in scenario I. The combined perimeter of the two cells adjacent to the cut boundary also changes less in scenario I compared to scenario II.

We also examined how different parameter values ($\bar{\Lambda}$, $\bar{\Gamma}$) affect the results of laser ablation simulations. We perform laser ablation simulations for parameter values that are slightly different from case I, ($\bar{\Lambda} = 0.12, \bar{\Gamma} = 0.02$), such that the tension is the same as case I while the contractility is slightly different. In Fig. 3.8 G and H, we show normalized area and perimeter changes, with respect to the normalized change in bond length, for cells surrounding the cut bond (using scenario II). Our results indicate that even for such small changes in parameter values the results of laser ablation change dramatically. The combined area changes of the cut cells are less than simulations of case I indicating that less anisotropic movements occur due to laser ablation. From these simulations, we conclude that laser ablation is strongly sensitive to the model parameters, line tension and perimeter contractility of cells, and can thus be used for testing precisely forces in the junctional network of cells in epithelia.

3.7 Summary

Tissues in nature experience a growing phase during development with several rounds of cell divisions. The final shape and morphology of the tissue is tightly controlled by a complex gene network. This network controls patterns of cell division in the tissue as well as the morphology of cells. Cell packing and morphology is affected mostly by cell mechanics. In this chapter, we have introduced a cell division algorithm based on quasistatic changes of cell properties. This algorithm has two main steps: (i) A growing phase of the dividing cell during which the preferred area of the cell is doubled in a few steps while minimizing the energy after each increment. (ii) At the end of this growing phase, we introduce a new boundary at a random angle passing through the cell center. We assign the same parameters for the two new cells and new boundaries as in the surrounding tissue. The tissue is then relaxed to the next local

minimum. Repeating this process, we can grow the tissue starting from a small number of cells up to an arbitrary size.

Cell division introduces disorder in the packing geometry of the network, which can be characterized by two sets of numbers: The fraction of n-sided cells, P_n, and the average area of n-sided cells normalized to the average area of cells in the network, $\langle A_n \rangle / \langle A \rangle$. We show that these quantities converge to well-defined values for growing tissues. To study how the packing geometry of a growing network is affected by cell mechanics, we simulate tissue growth for three sets of parameter values. Repeated cell division together with cell mechanics and cell adhesion can generate tissue morphologies that are surprisingly different from one another. For case I ($\bar{\Lambda} = 0.12$, $\bar{\Gamma} = 0.04$), pentagons are the most frequent polygon class and the frequency of six-sided cells is around two times more than case II, where ($\bar{\Lambda} = 0$, $\bar{\Gamma} = 0.1$). For case II, cells with a large number of sides (nine or more) are frequent, and even 20-sided cells are generated during growth. However, for case III ($\bar{\Lambda} = -0.85$, $\bar{\Gamma} = 0.1$), the frequency of nine-sided cells is negligible. The area variability is also different for these three cases. In both case I and II, the area of n-sided cells increases linearly with cell neighbor number, n, but the variation in case II is much stronger than in case I. This is significantly different for case III, in which the area of different class of polygons does not depend on neighbor number.

We then study two questions for these growing, non-equilibrium tissues. We first study phase transitions now for a growing network, which were introduced for the ground state in the previous chapter. We use the energy density of the network as an order parameter and we simulate growth for different sets of parameter values. We show that the order parameter vanishes for parameter values lying in the soft regime of the ground state phase diagram including the line between the semisoft and soft regimes. The value of the order parameter depends on the minimization threshold. Therefore to check whether decreases in the threshold can change our results, we repeat these simulations for different values of the minimization threshold. We find that changing this threshold has no effect on the transition line and this line agrees exactly with the transition line between the semisoft and soft regimes of the ground state phase diagram.

The second question that we study here concerns stresses that are induced during cell division. These stresses can change the shape of surrounding cells as well as resulting in two topological rearrangements: T1 and T2 transitions. In a T1 transition, a boundary shrinks and expands in the opposite direction and consequently changes the neighbor number relation of surrounding cells. T2 transitions correspond to elimination of a cell from the network, such that an unstable triangle is replaced by a vertex. We study the dynamics of T1 and T2 transitions in a growing network. We find that the rate of T1 transitions increases for decreasing line tension (decreasing the line tension results in decreasing the shear modulus of the network). Near the transition line between the semisoft and soft regimes of the ground state phase diagram, the rate of T1 transitions increases abruptly. The rate of T2 transitions increases for increasing line tension

(decreasing bulk modulus). For parameter values ($\bar{\Lambda} = 0.16$, $\bar{\Gamma} = 0.05$), this rate is so high that on average every two cell divisions result in one cell elimination.

We finally studied the displacement field of vertices due to local perturbations such as removal of cell boundaries. We showed that this results in anisotropic movement of vertices around the removed boundary. Vertices in the direction of the cut bond moves outward, however, vertices perpendicular to the cut bond moves slightly inward. We characterize the anisotropy of movements by quantifying the changes in the combined area and perimeter of the two cells that share the removed boundary. In a purely isotropic deformation of the two cells next to the cut bond, perimeter would increase linearly with the increase in length of the cut bond. However, a strongly anisotropic deformation would result in almost no changes in the perimeter of the two cells sharing the cut bond. Since this analysis is motivated most by experiments that a cell boundary is cut by laser ablation, we cannot say a priori how the laser affect mechanics of the two cells next to the cut bond. We therefore studied two scenarios for removal of a cell boundary. In the first scenario, we only remove the tension of the boundary leaving the two cells next to the boundary otherwise unaffected. In the second scenario, we remove both the tension on the boundary and also the perimeter contractility of the two cells adjacent to the cut boundary. In both cases, we decreased the tension (and/or the perimeter contractility) quasistatically, while minimizing the network energy after each quasistatic step. In these scenarios, we studied the anisotropy of displacements due to ablation and we found that the second scenario generates greater anisotropy than the first one. We also studied how mechanical parameters of the tissue might affect the displacements due to removal of a cell boundary. We found that slight changes in the parameter values of the model generate significantly different displacements around the cut bond. The displacements are less anisotropic for the case that we slightly change the perimeter contractility of cells from $\bar{\Gamma} = 0.04$ to $\bar{\Gamma} = 0.02$, while keeping the line tension constant. We conclude that laser ablation analysis is quite sensitive to cell mechanics and cell adhesion in tissues and can be used as a probe to quantify precisely forces in the tissues.

4   Tissue Ordering and Remodeling

Apart from the growing phase of tissue development characterized by frequent round of cell divisions, most epithelia experience a variety of morphological changes lacking cell division. This includes processes such as convergent-extension and epithelial repacking. During convergent-extension, the tissue shears strongly and cells intercalate such that, at the end of the process, the length of the tissue expands in one direction by a factor of two or three while converging in the other direction. An example of convergent-extension in the embryo of *Drosophila* is shown in Fig. 4.1. Another example of tissue remodeling and ordering happens during pupal development in the wing of *Drosophila*, in which the packing geometry of cells changes dramatically toward an almost hexagonal network. This improvement in the hexagonal packing is accompanied by emergence of another feature of the tissue, namely planar polarization. A set of interacting proteins redistribute anisotropically inside each cell, such that it becomes structurally polar. These polarized cells align with one another throughout the tissue, giving rise to global orders. During this process, one round of cell division without growth happen, and the tissue shears dramatically.

In this chapter we address various questions regarding ordering and remodeling of tissues. We first study convergent-extension of tissues due to cell intercalation induced by T1 transitions and show that to have an effective shear flow, we need oriented T1 transitions to occur. We then study the effect of one round of cell doubling without growth on packing geometry, and show that oriented cell doubling without growth can shear the network effectively. We identify two general methods for repacking of a grown tissue: annealing and shear flow of the network. To anneal the network, we randomly change the tension on cell boundaries and continuously relax the network towards the next local minimum. We show that repeating this process significantly results in more regular packing geometry of the tissue. Next we study shear flow of the tissue for no-slip boundary conditions. We show that, similar to annealing, this process can also improve the hexagonal packing of the network. We then introduce a theory for planar polarity of cells, which is coarse-grained on the level of proteins that take part in cell polarization. We introduce a robust mechanism to generate long range order in these systems. Finally we study the effect of shear flow on tissue polarization and we show that the polarity of cells reorients towards the shear direction. This suggests that on large length scales the system behaves similar to a liquid

crystals under shear flow. Using this idea we develop a hydrodynamic theory for polarized tissues, introducing a phenomenological parameter that controls how polarity is affected by shear flow.

4.1 Internal Shear Generated by Remodeling

4.1.1 Ordered Junctional Remodeling
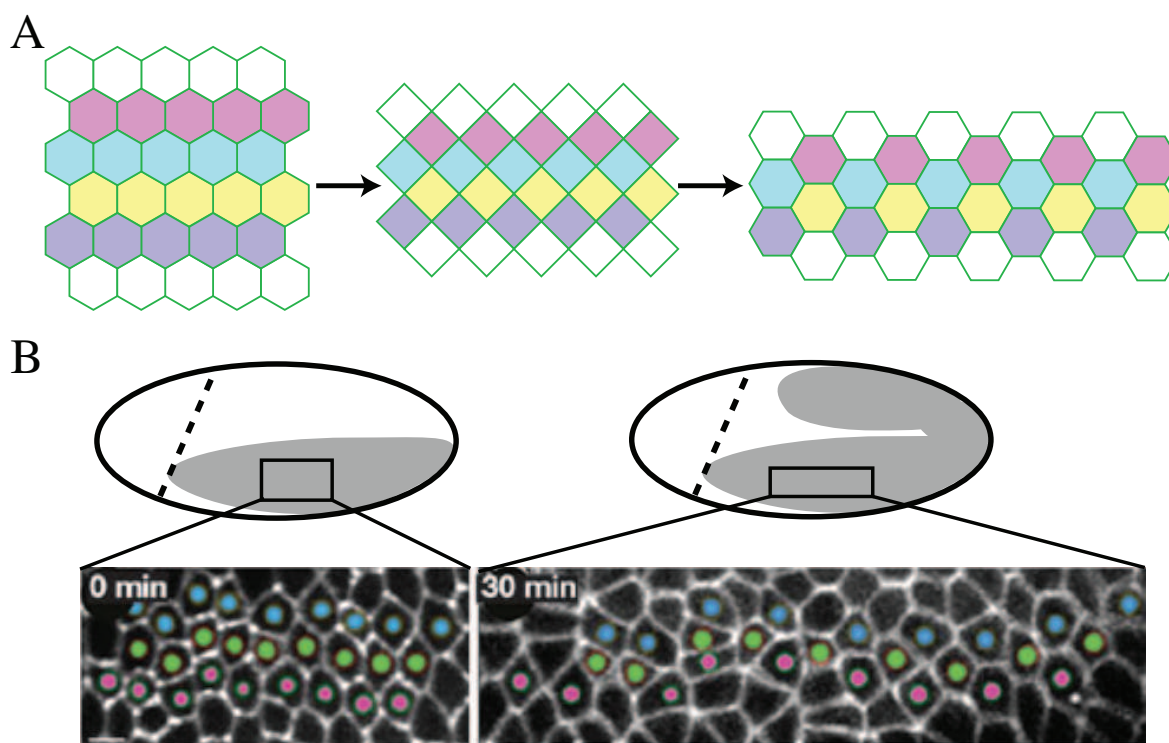
Figure 4.1: Convergent-extension. (A) Schematic of intercalation of cells via junctional remodeling, which results in convergent-extension. (B) Convergent-extension in the *Drosophila* embryo (adapted from [7]). The tissue expands its initial length by a factor of two in the absence of cell shape changes or cell division. Cells strongly intercalate with each other resulting in narrowing of the tissue in one direction and expansion in the other direction.

In the early development of animal embryos, there exists a stage where the morphology of the embryo is dramatically restructured by cell migration. These dramatic changes are governed by convergent-extension processes, in which cells intercalate (change their neighbors via junctional remodeling) with each other and the tissue becomes longer (extends in one direction). This extension is not driven by cell division or cell-shape changes, but rather by a rearrangement of

cells in the epithelium. A schematic of this cell rearrangements, cell intercalation and extension, is shown in Fig. 4.1 A. Note that cells that are in contact before intercalation, loose their contact and acquire new neighbors. One classical example of convergent-extension in biology is the germ-band elongation of the embryo of the fruit fly *Drosophila*, in which the length of the epithelia increases by a factor of two. Here the remodeling of cell-cell junctions is not driven by external forces at the epithelia boundaries, but depends on forces that act locally on cell boundaries. It has been shown experimentally that junctional remodeling during germ-band expansion have certain orientation in the plane of the epithelia [7]. A schematic of germ band expansion in the fruit fly embryo and an image of the tissue is shown in Fig. 4.1 B (adapted from [7]). Here cells are marked with different colors (initially forming rows) and followed with time. It is evident that during convergent-extension, cells intercalate and change their neighbor relations.

In this section, we study the effect of forced junctional remodeling (T1 transitions) on tissue shape and morphology in the absence of cell divisions. In order to study how the orientation of the selected bonds for T1 transition might affect the shear rate of the tissue, we select bonds for junctional remodeling such that their orientation with respect to the x axis is limited to $[\theta, \pi - \theta]$. The angle, θ, can vary between zero and $\pi/2$. If $\theta = 0$ then bonds with random orientation are selected for T1 transitions, and if $\theta = \pi/2$ only vertical bonds are selected for junctional remodeling. Selecting a bond with specific orientation, we then quasistatically increase the tension on the chosen boundary and relaxing the network towards the next local minimum. This results in shrinkage of the length of the boundary. We increase the tension on this boundary until its length falls below a threshold. We then change the neighbor relation of the two vertices at the end of this specific bond and change the tension of that bond to a value equal to the other bonds in the tissue. Finally we relax the network towards the next local minimum.

In Fig. 4.2 A, we show the initial network configuration of $5,000$ cells generated by growth algorithm for ($\bar{\Lambda} = 0.06$, $\bar{\Gamma} = 0.05$). In Fig. 4.2 B and C, we show the network configuration after $10,000$ repeated T1 transitions for two choices of the angle $\theta = 0$ and $\theta = 4\pi/9$, respectively. Selection of bonds with random orientation for T1 transitions ($\theta = 0$) results in almost no shear deformation of the tissue ($L_x/L_y \simeq 1$ after $10,000$ T1 transitions). However, for $\theta = 4\pi/9$, this process can generate a continuous shear flow of the tissue ($L_x/L_y = 2.23$ after $10,000$ T1 transitions). In Fig. 4.2 D, we plot L_x/L_y as a function of convergent-extension steps, N, for these two cases. The shear deformation L_x/L_y increases linearly with N for the first $5,000$ T1 transitions. The nonlinear increment in L_x/L_y after $5,000$ T1 transitions might be due to finite size of the tissue.

These results suggest that a planar organization of T1 transitions is required for an effective convergent-extension of the tissue. To study how this angular ordering might affect shear rate
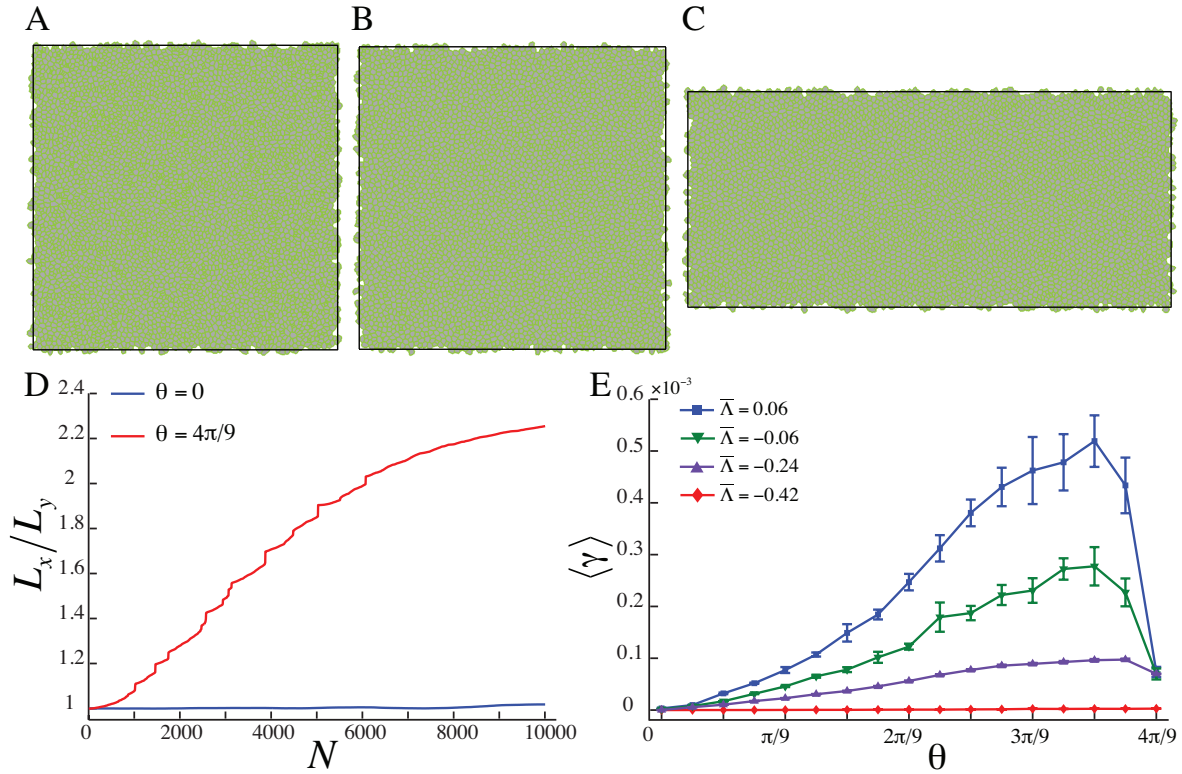
Figure 4.2: Convergent-extension induced by polarized T1 transitions. (A) A grown network for parameter values ($\bar{\Lambda} = 0.06$, $\bar{\Gamma} = 0.05$). (B) Network configuration after $10,000$ T1 transitions, where bonds are selected at random orientations. (C) Convergent-extension after $10,000$ T1 transitions, where bonds are selected with a restricted angle ($\theta = 4\pi/9$). As opposed to the case in (B), the tissue expanded in the x direction by a factor of ~ 2.23. (D) The aspect ratio of the simulating box, L_x/L_y, for cases (B) and (C) as a function of cell number. (E) Shear rate for different sets of parameter values as a function of the angle θ.

of the tissue, we perform simulations while systematically changing the angle θ. For each simulation, we measure the average shear rate as the average of the variation in the box size ratio, L_x/L_y. For parameter values as above we plot the average shear rate in Fig. 4.2 E (blue line) as a function of the angle θ. As discussed previously, for $\theta = 0$ bonds with random orientation are selected for T1 transitions, and this results in approximately zero shear rate. However, if we increase θ, i.e. we select bonds for T1 transition that lie in a limited angular zone, the shear rate increases up to $\theta \simeq 7\pi/18$. Interestingly, for a sharper angular zone ($\theta = 4\pi/9$), the shear rate decreases significantly to a lower non-zero value.

We next study how cell mechanics might affect shear rate during convergent-extension. We repeat simulations similar to the case ($\bar{\Lambda} = 0.06$, $\bar{\Gamma} = 0.05$) for other sets of parameter values; we choose the same perimeter contractility as the previous case, while vary the line tension. For

each set of parameter values, we choose different angles θ and simulate convergent-extension for $10,000$ steps. In Fig. 4.2 E, we plot the shear rate for each angle and each set of parameter values. The two cases $\bar{\Lambda} = -0.06$ and -0.24 are similar to $\bar{\Lambda} = 0.06$ in that they lie in the solid region in the ground state phase diagram. These three cases show similar behavior: the shear rate increases for increasing θ up to a certain value and then decreases for larger θ. The shear rate for these cases is zero for $\theta = 0$. For other values of θ, the shear rate decreases for decreasing line tension $\bar{\Lambda}$. For the case $\bar{\Lambda} = -0.42$, however, the network is soft and for any choice of θ the shear rate is approximately zero. From these results we conclude that shearing a network internally (i.e. as to produce convergent-extension) depends strongly on the system's ability to undergo T1 transitions. The shear rate of the tissue during convergent-extension also depends on the shear modulus of the network. Networks with higher shear modulus have higher shear rates during convergent-extension and for networks with zero shear modulus, the shear rate is almost zero.
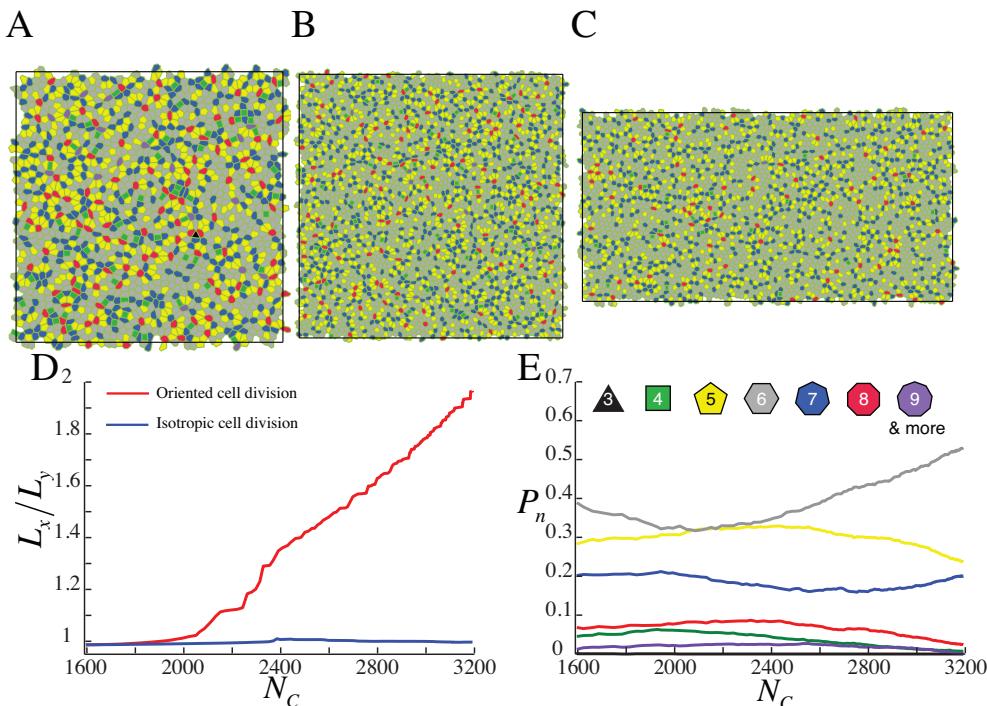
4.1.2 Cell Division without Growth

In this section we introduce another mechanism that can generate shear in tissues internally in the absence of external forces. We use a modified cell division algorithm, such that a cell that has not divided is randomly selected in the tissue. We then introduce the new boundary passing the cell center and assign half of the preferred area of the mother cell to each of the daughters and then relax the network to the next local minimum. Note that this algorithm is different from what we described in Sec. 3.1:

(i) In this algorithm cells only divide once.

(ii) The mother cell does not double its size before division.

(iii) The new daughter cells have half of the preferred area of the mother cell.

Since the preferred area of the daughter cells is half of the mother, the total area of the tissue almost remains unchanged during this process.

We start from a grown tissue of $1,600$ cells for parameter values ($\bar{\Lambda} = -0.12$, $\bar{\Gamma} = 0.04$) and we perform one rounds of cell division without growth. For the case that there is no preferred angle for the new boundaries that are formed during cell divisions, the shear rate of the tissue is negligible. In Fig. 4.3 A and B, we show the initial and final network configurations after one round of cell division without growth, respectively. However, if we assume a preferred angle for the new bonds that are formed during cell divisions, this can generate strong convergent-extension. In Fig. 4.3 C, we show the network configuration after one round of oriented cell division without growth, where the new boundary introduced during cell divisions attains an angle $\theta = \pi/2 \pm \pi/18$. Here, the network shears by a factor of two after one round of oriented cell doubling without growth. In Fig. 4.3 D, we plot the ratio L_x/L_y as a function of N_C for simulations of isotropic and oriented cell division without growth.

Figure 4.3: Cell division without growth. (A) The initial network configuration of 1600 cells
generated by the growth algorithm for parameter values ($\bar{\Lambda} = -0.12$, $\bar{\Gamma} = 0.04$).
(B) Network configuration after one round of isotropic cell division without growth.
(C) Network configuration after one round of oriented cell division without growth.
The new boundaries that are generated by cell divisions have a preferred initial
angle $\theta = \pi/2 \pm \pi/18$. The network shears due to oriented cell division without
growth. In A-C cells are colored according to their neighbor number (for the color
codes see (E)). (D) The tissue aspect ratio L_x/L_y as a function of cell number. (E)
The frequency of n-sided cells during one round of oriented cell division without
growth.

Note that the packing geometry of the network also changes during one round of cell doubling
without growth. We show the frequency of n-sided cells as a function of cell number for a
network with oriented cell divisions without growth in Fig. 4.3 E. The frequency of six-sided
cells decreases for the first half of the process, while the frequency of eight-sided cells increases.
Later the frequency of six-sided cells increases to about 60%. Interestingly, the frequency of five
and seven-sided cells approaches to a similar value by the end of the process indicating that they
appear mostly in pairs. From these two sections, we conclude that oriented T1 transitions and
oriented cell division without growth can generate shear in the network in absence of external
forces. Although for simulations of cell division with growth, we observed that the packing
geometry of the network converges to a specific value and remains unaffected by further cell

divisions, here one round of oriented cell doubling without growth improves the hexagonality of the network.

4.2   Dynamics of Hexagonal Order

4.2.1   Annealing
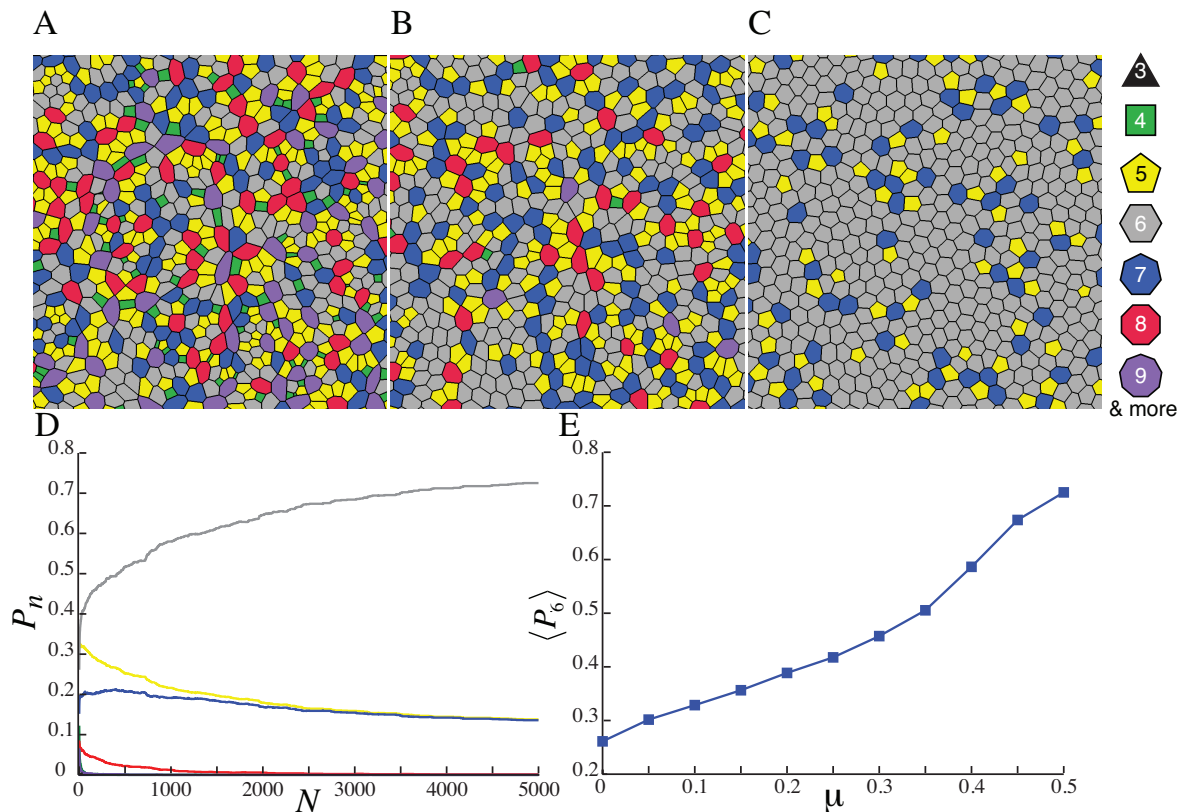
Figure 4.4: Simple annealing of the network results in hexagonal repacking of the network. (A)-(C) Three time points of annealing simulations for a grown tissue corresponding to case I ($\bar{\Lambda} = 0.12$, $\bar{\Gamma} = 0.04$) and noise strength, $\mu = 0.5$. (A) is the initial network configuration generated by growth. Each cell is colored according to its neighbor number. (D) Frequency of n-sided cells as a function of annealing step for $\mu = 0.5$. (E) Converged value of the frequency of hexagons in annealing simulations as a function of noise strength μ.

Apart from the growing phase of tissue development, in which repeated cell division induces disorder in the packing geometry of tissues, there is a phase of development during which the packing of the tissue changes dramatically toward the hexagonal packing. This process happens mostly in the absence of cell division. In this and the following sections, we introduce

two mechanisms that can influence the hexagonal packing of a tissue. In the first mechanism, we introduce fluctuations in cell boundary tension that can result in annealing of the network toward the hexagonal ground state. In the second mechanism, we generate a shear flow in the network that can likewise repack the tissue and increases the hexagonality of the network.

We showed in Sec. 3.2 that cell division introduces disorder in the packing geometry of tissues. During repeated cell division, the tissue becomes trapped in a local minimum of the energy function and the packing geometry converges toward a specific pattern. Although cell division generates fluctuations in packing geometry of the network, these fluctuations are not sufficient to drive the tissue towards the hexagonal packing. Here we introduce fluctuations in cell boundary tension that induce rearrangements, which are then biased by the energy function toward the hexagonal ground state. This is analogous to annealing, during which crystalline order is approached. We start with an irregularly packed network configuration, in which proliferation had ceased and introduce stochastic changes of line tensions Λ_{ij} at randomly chosen cell boundaries. The line tension of the boundary is then modified as $\Lambda_{ij} = \Lambda(1 \pm \mu)$, where μ is the noise strength and $\langle \Lambda_{ij} \rangle = \Lambda$ is unchanged.

We start from a grown tissue with irregular packing geometry using parameter values corresponding to case I ($\bar{\Lambda} = 0.12$, $\bar{\Gamma} = 0.04$) (see Fig. 4.4 A). We then change the tension of each bond stochastically as described above and relax the network toward a local minimum. During this process, a number of T1 transitions occur. We repeat this process for many steps until the network packing converges to a specific distributions. In Figs. 4.4 B and C we show two snapshots of an annealing simulation for $\mu = 0.5$, where the tissue rearranges to hexagonal packing by the end of this process. In Fig. 4.4 D we plot the frequency of different polygon classes as a function of annealing steps, N. The frequency of six-sided cells increases and converges to a value, higher than the initial value generated by growth. Consequently the frequencies of other polygon classes decrease. Interestingly, the frequency of pentagons, which is the highest at the beginning of annealing, approaches to a similar value as the frequency of heptagons. Pentagons and heptagons appear mostly as pairs during annealing simulations (see Fig. 4.4 C).

We wonder if the stationary frequency of hexagons depends on the noise strength μ. We systematically change the value of μ from 0.05 to 0.5 and simulate annealing for the given noise strength. In Fig. 4.4 E, we plot the converged frequency of hexagons, $\langle P_6 \rangle$ for simulations of annealing with different noise strength. The converged value of $\langle P_6 \rangle$ increases linearly with noise strength. We conclude that the disordered geometry of the proliferating tissue represents a local minimum of the energy function. Because the global minimum in case I is a perfect hexagonal lattice, the energy function would bias fluctuations to bring the initially irregular network closer to the hexagonal ground state. Our simulations show that introducing fluctuations in line tension (which could correspond to fluctuations in adhesion and contractility in real tissues) is sufficient to drive remodeling.
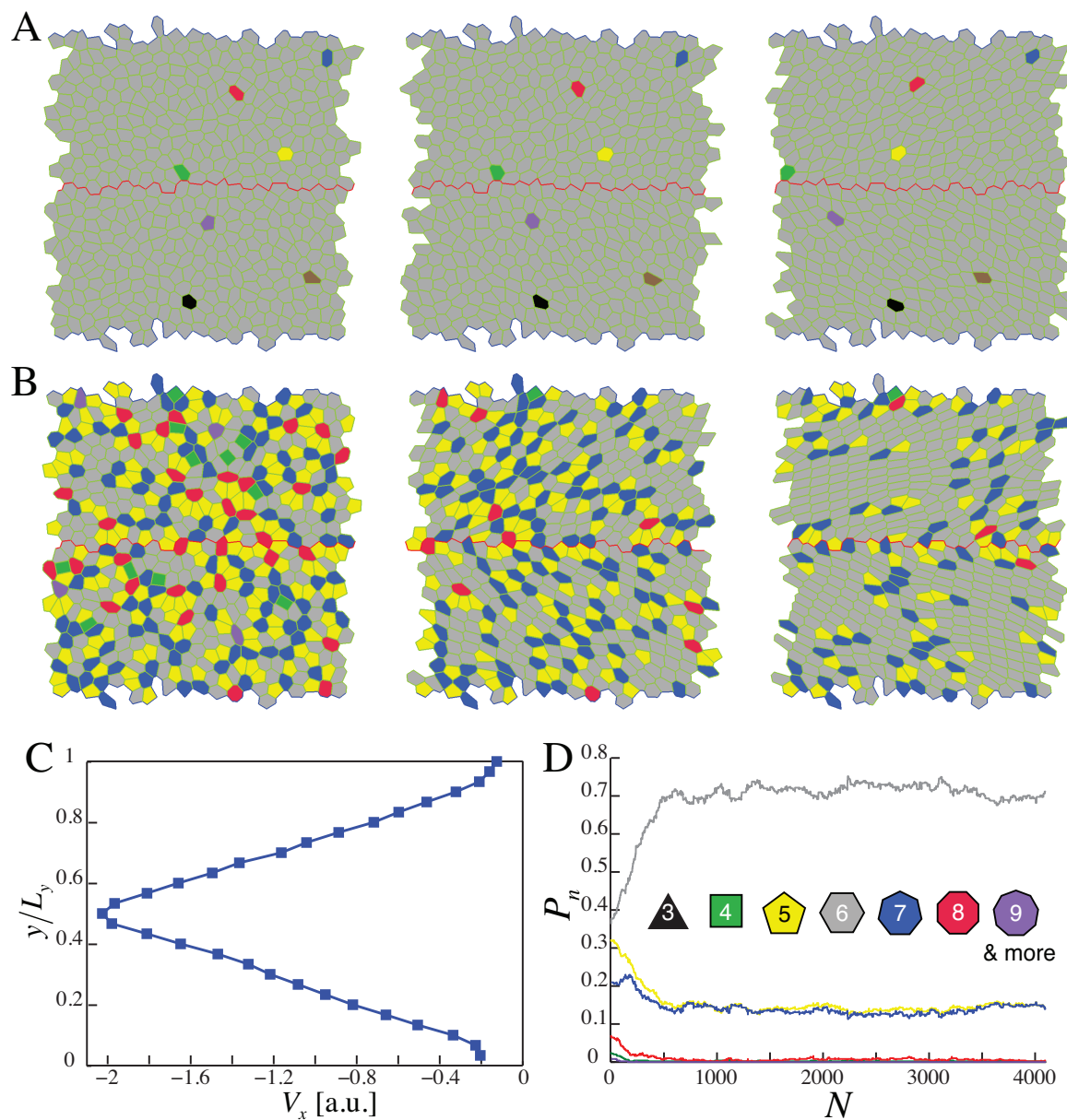
4.2.2 Shear Flow

The second mechanism that affects tissue packing geometry is shear flow. To generate shear flow in tissues, we use different boundary conditions than ones used in growth simulations. We introduce no-slip boundary conditions by fixing the position of vertices on the lower and upper parts of the simulating box. We also fix L_y, the length of the simulating box in the y direction. This is different from growth simulations, where we minimize the energy function with respect to box sizes, L_x and L_y, i.e. we impose no external forces on the boundaries. Here we select vertices in the middle of the tissue such that their connecting bonds make a horizontal line (red line in Fig. 4.5 A). We then impose a small displacement to these vertices in the middle of the network, relaxing other vertices while keeping the position of vertices on the boundary and in the middle fixed.

One difficulty in generating shear flow on tissues is the existence of soft elastic modes associated with large-scale shear deformations. We use the following algorithm to generate shear flows, which has three main steps; by repeating these steps we can generate continuous flow of the tissue. We first increase slightly the x position of the middle vertices. We then minimize the energy function using the conjugate gradient method (using higher precision than in other simulations). During this step, we only minimize the energy function with respect to the position of vertices, while preventing any topological rearrangements (we prevent T1 transitions from happening). We then search for those bonds that are shorter than a threshold, impose a T1 transition on those vertices, and relax the network using the conjugate gradient method. We repeat this last step until no T1 transitions happen. We then increase the position of the middle vertices slightly and repeat these steps. We show in Fig. 4.5 A three time steps of the shear flow of a grown tissue, marking a few cells in the tissue with different colors to illustrate their movements.

In Fig. 4.5 B we plot the x component of the velocity field in the tissue, V_x, (averaged over the x direction) as a function of y. The velocity is maximum in the middle of the tissue and decreases linearly to zero towards the boundary. Small velocities reported for $y = 0$ and $y = L_y$ are artifacts due to binning. During the shear flow, the packing of the tissue changes dramatically. The number of hexagons increases while the number of other n-sided cells decreases. We show three time points of tissue flow in Fig. 4.5 C where each cell is colored according to its neighbor number (for color codes see Fig. 4.4). As the cells stretch in the shear direction, T1 transitions happen, which increases the number of hexagons. We quantify the proportions of n-sided cells in the tissue and plot them as a function of shear steps, N, in Fig. 4.5 D. Similar to the annealing case, the percentage of pentagons decreases and converges to a value similar to the percentage of heptagons, which again indicates that five-sided cells and seven-sided cells appear as pairs during tissue flow. This is evident in the third panel in Fig. 4.5 C. Note that there is a transition from shear flow to shear banding depending on the magnitude of the increment

Figure 4.5: Shear flow in the vertex model. (A) Three time points of shear flow in the vertex model. Vertices lying on the red line in the middle of the tissue move to the left with constant velocity using no-slip boundary condition . Few cells are colored differently to illustrate the flow. (B) Packing geometry of the tissue for three time points of tissue flow (color codes as D). (C) Average of the x component of the velocity, V_x, over the x direction as a function of normalized y coordinate. (D) Frequency of different polygon classes as a function of shear step, N.

in the x position of the middle vertices during each step. We do not study shear banding in this thesis.

4.3 Theory of Planar Cell Polarity

As we discuss in Sec. 1.3, planar cell polarity (PCP) is a tissue-level phenomenon that coordinates cell behavior in epithelia. A particular example of planar cell polarity at work is revealed in the orientation pattern of hairs, which form on the wing of the fruit fly *Drosophila*. Planar polarity is established by a molecular organization that includes asymmetric distribution of PCP proteins within cells. The distribution of these proteins in a given cell determines of the polarity of neighboring cells. At the end of wing development, a specific pattern of PCP orientational order is established. Here we present a coarse-grained description of cell polarity and discuss how such a cell-size model can result in large range order of the PCP distribution. We also discuss how a polarized tissue responds to various deformations such as shear flow.

4.3.1 Planar Polarity in the Vertex Model
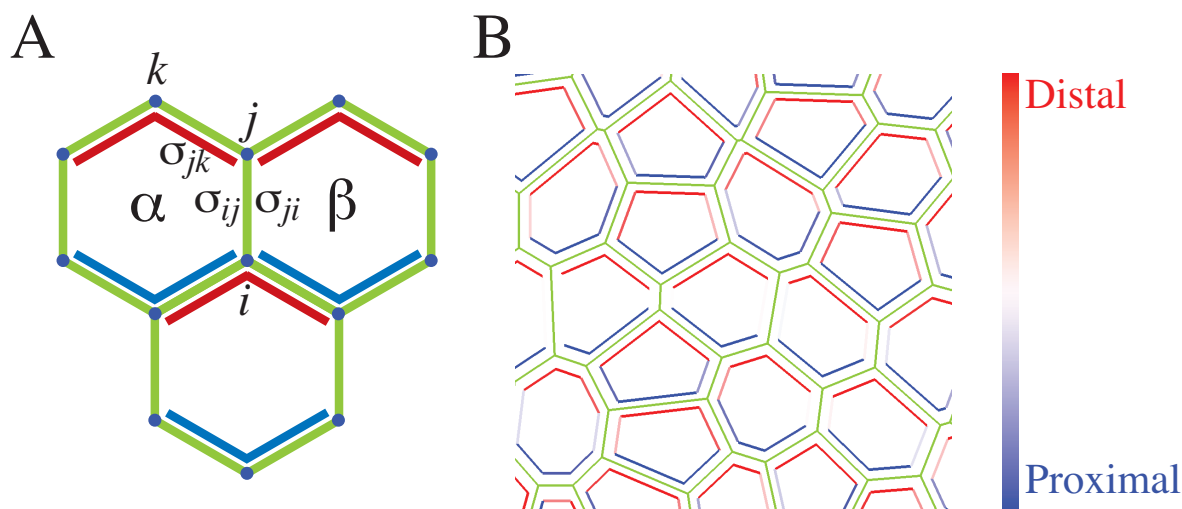
Figure 4.6: Schematic of PCP proteins within the vertex model. (A) The level of proximal or distal proteins on each side of a cell boundary between vertex i and j is denoted by σ_{ij}^{α} and σ_{ji}^{β}. (B) Example of PCP configuration for a randomly packed cellular network.

The vertex model that we described in Chap. 2 could predict packing geometry and tissue morphology, but contains no information about planar polarity of cells. To explain cell polarity dynamics and tissue mechanics consistently and within one model we add a PCP subsystem

to the vertex model. Here we coarse-grained our PCP model over different proteins that are involved in planar polarization of cells, such that we only consider two type of interacting proteins. We name these two interacting proteins as "proximal" and "distal" proteins. In this coarse-grained description of the PCP system each bond between vertex i and j is assigned two variables, σ_{ij}^{α} and σ_{ji}^{β}, where α and β are indices of the two cells sharing the boundary $\langle i, j \rangle$ (see Fig. 4.6 A). These variables, σ_{ij}^{α}, describe the level of PCP proteins on either side of a boundary and can take values between -1 and 1. Positive values of σ_{ij}^{α} correspond to high levels of proximal proteins (shown by blue in Fig. 4.6 A and B) while negative values correspond to the presence of distal proteins (shown by red in Fig. 4.6 A and B). Proximal and distal PCP proteins form complexes in cells that interact differently across cell boundaries and within the cell. These complexes attract each other across cell boundaries, while each locally inhibits the presence of the other within a cell.

These effects can be mimicked by an energy function for the PCP system

$$E(\{\sigma_{ij}^{\alpha}\}) = J_1 \sum_{\langle i,j \rangle} \sigma_{ij}^{\alpha} \sigma_{ji}^{\beta} - J_2 \sum_{\langle i,j,k \rangle} \sigma_{ij}^{\alpha} \sigma_{jk}^{\alpha}, \tag{4.1}$$

where J_1 and J_2 are interaction parameters. The first term in Eq. 4.1 describes interaction of PCP proteins across cell boundaries, separating cells α and β. The sum is taken over all cell boundaries $\langle i, j \rangle$. For positive values of J_1 the energy is minimal when proximal and distal proteins interact (proximal and distal proteins accumulate on different sides of a boundary). The second term, with positive J_2, describes inhibition of proximal and distal proteins within cell α; the sum is over all pairs $\langle ijk \rangle$ of adjacent bonds $\langle ij \rangle$ and $\langle jk \rangle$, implying that inhibition can reach to neighboring bonds. In Fig. 4.6 B, we show an example of distribution of proximal and distal proteins in a randomly packed network. We consider two additional constraints for the variables σ_{ij}^{α}:

(I) equal amounts of proximal and distal proteins are found in each cell.

(II) these amounts do not change with time.

These two constraints can be fulfilled using Lagrange multipliers. These constraints are mathematically given by

$$
\begin{aligned}
(I) &\quad\rightarrow\quad \sum_{\langle i,j;\alpha \rangle} \sigma_{ij}^{\alpha} = 0 \\
(II) &\quad\rightarrow\quad \sum_{\langle i,j;\alpha \rangle} (\sigma_{ij}^{\alpha})^2 = C,
\end{aligned} \tag{4.2}
$$

where C is a constant and the summation $\langle i, j; \alpha \rangle$ is over all bonds $\langle i, j \rangle$ of cell α. Using these additional constraints, we define the energy function $F(\{\sigma_{ij}^{\alpha}\})$

$$F(\{\sigma_{ij}^{\alpha}\}) = E(\{\sigma_{ij}^{\alpha}\}) - \sum_{\alpha} \lambda_1^{\alpha} \sum_{\langle i,j;\alpha \rangle} \sigma_{ij}^{\alpha} - \sum_{\alpha} \lambda_2^{\alpha} \sum_{\langle i,j;\alpha \rangle} ((\sigma_{ij}^{\alpha})^2 - C), \tag{4.3}$$

where λ_1^α and λ_2^α are the Lagrange multipliers and the summation $\langle i, j; \alpha \rangle$ is over all bonds $\langle i, j \rangle$ of cell α. Using such an energy function, we can define a set of dynamic equations for the PCP level of each cell bond

$$\frac{d\sigma_{ij}^\alpha}{dt} = -k_p \frac{\partial F(\{\sigma_{ij}^\alpha\})}{\partial \sigma_{ij}^\alpha},$$

(4.4)

where $k_p = 1/\tau J_1$ is a kinetic coefficient and τ is the relaxation time for proximal and distal proteins. To fulfill the additional constraint (that the PCP level of each bond is limited to $[-1, 1]$), we introduce a new variable ϕ_{ij}^α, such that $\sigma_{ij}^\alpha = \cos(\phi_{ij}^\alpha/2)$. We can then write the dynamic equations in Eq. 4.4 for the new variables ϕ_{ij}^α.

4.3.2   Origin of Large-Scale Polarity

Before studying the dynamics of the PCP model, we need to define concepts to analyze the pattern of PCP proteins in tissues. For a given distribution of proximal and distal proteins inside each cell, we define a polarity vector $\mathbf{P}_\alpha$ for that cell, where P_x^α and P_y^α, the x and y components of the vector are defined as
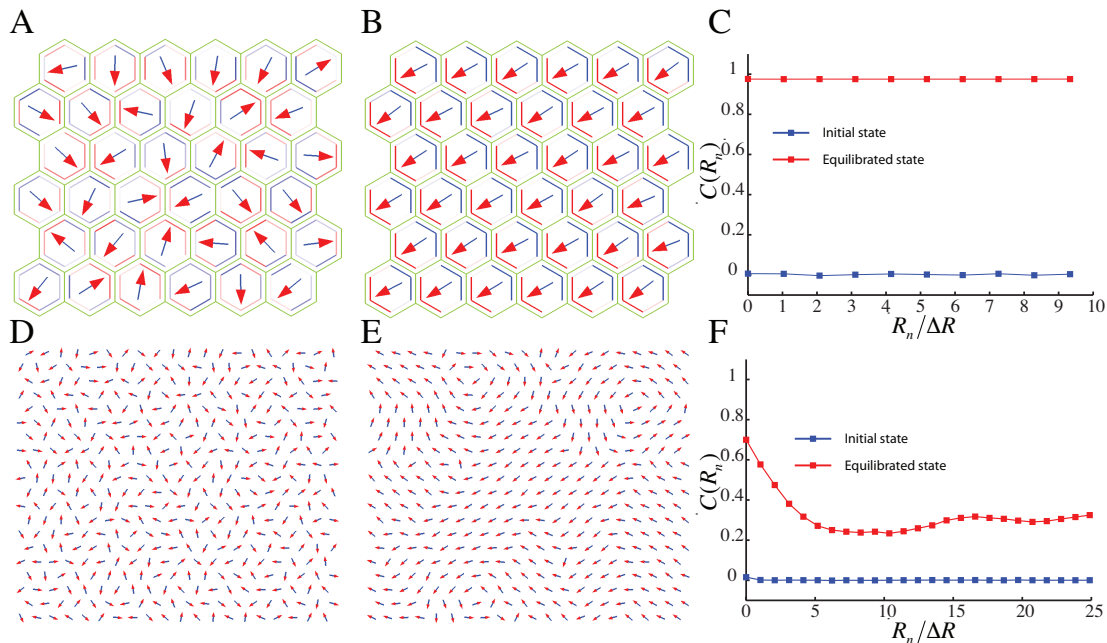
$$P_\alpha^x = \frac{1}{2\sqrt{3}} \int_0^{2\pi} \sigma(\theta) \cos\theta d\theta$$

$$P_\alpha^y = \frac{1}{2\sqrt{3}} \int_0^{2\pi} \sigma(\theta) \sin\theta d\theta.$$

(4.5)

The PCP distribution, $\sigma(\theta)$, is the level of proximal and distal proteins on cell boundaries at the angle θ with respect to the x axis. In our model, the PCP distribution is constant over each boundary and we can do the integration in Eq. 4.5 analytically

$$
\begin{aligned}
P_\alpha^x \quad &= \frac{1}{2\sqrt{3}} \int_0^{2\pi} \sigma(\theta) \cos\theta d\theta \\
&= \frac{1}{2\sqrt{3}} \sum_{\langle i,j \rangle} \sigma_{ij}^\alpha \int_{\theta_{ij}}^{\theta_{jk}} \cos\theta d\theta \\
&= \frac{1}{2\sqrt{3}} \sum_{\langle i,j \rangle} \sigma_{ij}^\alpha (\sin\theta_{jk} - \sin\theta_{ij}) \\
P_\alpha^y \quad &= \frac{1}{2\sqrt{3}} \sum_{\langle i,j \rangle} \sigma_{ij}^\alpha (\cos\theta_{ij} - \cos\theta_{jk}),
\end{aligned}
$$

(4.6)

where θ_{ij} is the angle between vertex i and its neighbor j. We define the orientation correlation function

$$C(R_n) = \frac{1}{N_n} \int_{R_n}^{R_n + \Delta R} d\lambda \sum_{\alpha, \beta} \mathbf{P}_\alpha \cdot \mathbf{P}_\beta \, \delta(|\mathbf{R}_\alpha - \mathbf{R}_\beta| - \lambda)$$

(4.7)

Figure 4.7: Large-scale polarity. (A) Network of hexagonal packing of 36 cells with a randomly distributed proximal and distal proteins. The arrows show the direction from the proximal to the distal sides of cells. (B) Equilibrated PCP configuration of A. (C) Spatial correlation function of cell polarity, $C(R_n)$, for the networks shown in A and B. (D) Randomly distributed PCP configuration for a network of 400 cells in hexagonal packing. For plotting purpose, we only show the polarity vector of cells. (E) Equilibrated PCP configuration of D, in which few defects remain in the network after the equilibration. (F) The correlation function of cell polarity for the networks shown in D and E.

with the normalization factor

$$N_n = \int_{R_n}^{R_n+\Delta R} d\lambda \sum_{\alpha,\beta} \delta(|\mathbf{R}_\alpha - \mathbf{R}_\beta| - \lambda). \tag{4.8}$$

We bin cells according to their center-center distance and $R_n = n\Delta R$ denotes bin boundaries and ΔR is bin size. $\mathbf{R}_\alpha$ and $\mathbf{R}_\beta$ indicate the position of the center of cells α and β, respectively, and the sum is over all pairs of cells in the network. In the following sections we choose bin size ΔR as the average cell diameter in the tissue.

To study the behavior of the PCP model described in Sec. 4.3.1, we solve numerically the dynamic equations for the PCP variables, $\{\sigma_{ij}^\alpha\}$, for a hexagonal network packing. We use a fourth-order Runge-Kutta method to solve the dynamic equations given by Eq. 4.3, with interaction parameters $J_1/J_2 = 2$ and relaxation time $\tau = 1$. We use a random distribution of proximal and distal proteins as our initial PCP configuration. For small lattices, the PCP system

equilibrated toward a state where the polarity arrows of the cells point in the same direction and long range order appears in the network. Since there is no preferred direction for the polarity of the network, the final direction of the polarity arrows is random and pointing in one of the six-fold symmetric directions specified by the hexagonal network. In Figs. 4.7 A and B we show an example of initial and equilibrated states for a lattice of 36 cells, respectively. In Fig. 4.7 C we plot the correlation function $C(R_n)$ for the initial and equilibrated pattern of PCP . For the initial PCP pattern (chosen randomly) the correlation function is almost zero, while for the equilibrated state the correlation function reaches its maximum.

   During equilibration of the PCP system for larger networks polarity defects appear in the network that are stable for long time scales; the system is trapped in a local minimum, which requires large fluctuations to pass the barrier towards the global minimum. These defects destroy the long range order in the system. In Figs. 4.7 D and E, we show an example of initial and long time equilibrated PCP system for a hexagonally packed network of 400 cells, respectively (to show defects in the network more clearly, we only show the polarity arrows of cells and not cell boundaries). We also plot the correlation function $C(R_n)$ for the initial and equilibrated PCP system in Fig. 4.7 F. The correlation is high for small distances, while it decreases over large distances due to the presence of defects.
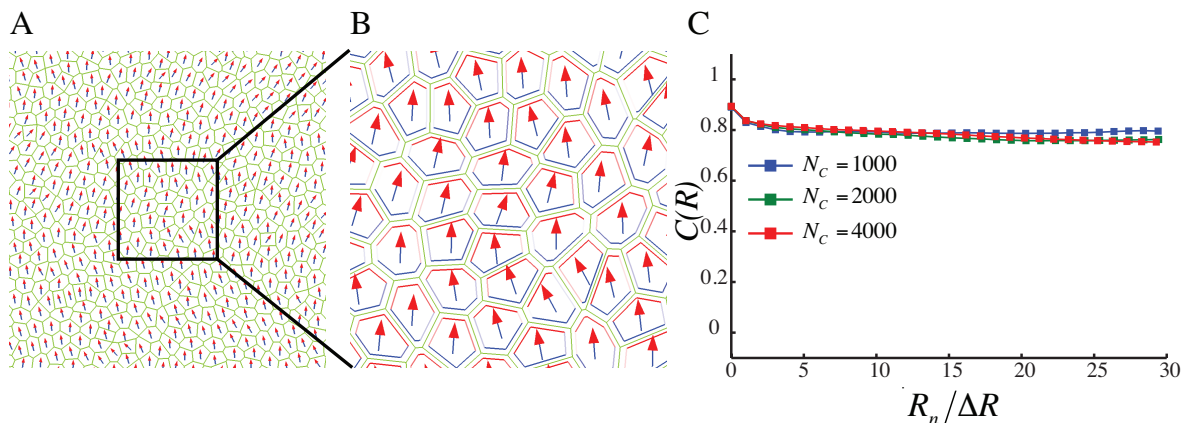

Figure 4.8: Large-scale PCP order in growing tissues. (A) Part of a grown tissue in presence of PCP proteins. Arrow indicate the direction of polarity of cells. (B) Small portion of the tissue in (A). (C) Correlation function of cell polarity for a growing network as a function of cell-cell distance normalized to bin size, $R_n/\Delta R$, for three stages of tissue growth. The total number of cells, N_C, is indicated.

   Thus far we cannot generate polarized tissues of arbitrary size starting with a random distribution of PCP proteins and relaxing the system toward the minimum. The fact that the PCP system in networks with a small number of cells relaxes spontaneously to its global minimum

suggests that we can add one more cell to this small polar network by cell division and then relax the new PCP configuration, while maintains long-range order. Even if the polarity of the new cell is different from the global polarity of the tissue, due to neighbor interactions they will align their polarity with the global direction of the tissue polarity. Repeating this process, we can generate arbitrary large polarized tissues. In Fig. 4.8 A, we show an example of such a polarized grown tissue. In Fig. 4.8 B, we show a smaller section of the network together with distribution of proximal and distal proteins on each bond. We plot the correlation function $C(R_n)$ for different cell number N_C for a growing tissue in Fig. 4.8 C. For increasing cell number, N_C, the shape of the correlation function remains similar and qualitatively converges to one, indicating that the polarity is essentially preserved during growth.

4.3.3 Reorientation of Polarity by Shear
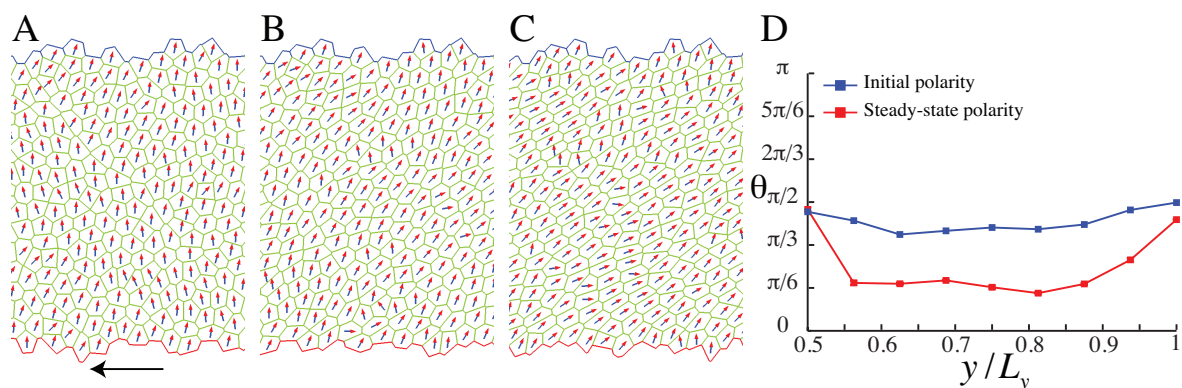
Figure 4.9: Polarity reorientation due to shear flow. (A)-(C) Three time points of shear flow of a polarized network. (A) is the initial polarity configuration. Vertices located on the top blue boundary are fixed and vertices laying on the lower red boundary move to the left with constant velocity. Due to the shear flow, polarity vector of cells reorients towards the flow direction. (D) Average angle of polarity vector of cells over the x direction as a function of normalized y coordinate for simulations shown in A and C.

In Sec. 4.2.2, we proposed a method to generate shear flow in the vertex model. Later, in Sec. 4.3.2 we proposed a mechanism to generate long range order of PCP pattern by growing a small polar network using repeated cell division. We now wonder how a polarized tissue behaves under shear flow. To simulate shear flow of these polar networks, we should consider separation of time scales for the PCP relaxation and the cell shape relaxation. Cell shape relaxation happens at about several minutes, while PCP relaxation time is about several hours; here we assume that cell shape relaxes instantaneously due to local perturbations compared to PCP

relaxation. Therefore for a time step Δt, we solve the dynamic equations for the PCP variables and then impose a shear step as described in Sec. 4.2.2 while the time is not changed during the later step.

In Fig. 4.9 A-C, we show part of the network for three time points of tissue flow, where the polarity of cells is indicated by arrows. Here, we only show cells whose centers are located above the middle line. Vertices lying on the upper blue boundary are fixed and vertices locating on the lower red boundary move to the left with a constant velocity. Note that Fig. 4.9 A represents the initial condition at $t = 0$. Also note that we have imposed periodic boundary conditions for the PCP variables in both x and y directions. Due to the shear flow, the polarity vector of cells reorient, while the global polarity order is preserved. In Fig. 4.9 D, we show the average of the polarity angle θ with respect to the x direction, as a function of the normalized y coordinate, y/L_y. The polarity of those cells that are close to the boundaries at ($y/L_y = 0.5$ and 1) is affected strongly by the boundary conditions and dose not reorient effectively due to the flow. However, for the cells located between these two boundaries, the polarity vectors converge to a well-defined steady sate value. We conclude that shear flow can reorient the polarity vector of cells to a specific orientation with respect to the shear direction.

4.3.4 Hydrodynamic Description of Tissue Polarity

The fact that the polarity vector of cells reorient during shear flow of the network and reaches a steady state value, suggests that we can use a multi-scale approach and describe the dynamics of polarity order for larger scales. This behavior of the PCP model in shear flow, is well known in liquid crystal physics as *nematodynamics*. A nematic flow is very similar to normal liquid flow with a difference that the orientational motion of the molecules are coupled to their translational motions. Here we consider two mechanisms that can change the orientation of nematic molecules during flow: vorticity and shear. Vorticity can clearly rotate the orientation of the molecules, however, the influence of shear component of the flow on orientation of the molecules is less obvious. This later effect of flow on the molecular orientation is characterized in liquid crystal physics by a phenomenological coefficient ν that couples the orientation of molecules with shear [76].

Here, we develop a simple model to describe polarity reorientation of cells in shear flow. The dynamics of the polarity vector of a cell, $\mathbf{p}$, is given by

$$\partial_t p_\alpha = -\nu v_{\alpha\beta} p_\beta - \omega_{\alpha\beta} p_\beta, \tag{4.9}$$

where $v_{\alpha\beta} = (\partial_\alpha v_\beta + \partial_\beta v_\alpha)/2$ is the strain rate tensor and $\omega_{\alpha\beta} = (\partial_\alpha v_\beta - \partial_\beta v_\alpha)/2$ is the vorticity of the velocity field $\mathbf{v}$. We sum over repeating indices. For $|\nu| > 1$, there is a critical angle θ_0 between the velocity direction and the polarity direction of cells. This angle is given by $\cos(2\theta_0) = 1/\nu$. Thus far from the boundaries, the polarity vector of cells tend to lie precisely

at this angle. In the vicinity of the boundaries, since the polarity vectors of cells must adjust to the boundary conditions, their orientation changes. For $|\nu| < 1$, the polarity vector of cells are very strongly deformed. We found in Sec. 4.3.3, that the steady state angle of the polarity vector is $\theta_0 \sim \pi/6$, which implies that the $\nu \sim 2$.

4.4   Summary

There are many developmental processes that affect tissue shape and morphology in the absence of growth. Two examples of such processes have been studied in this chapter: convergent-extension and hexagonal repacking. Convergent-extension is mostly studied in embryos, such as the embryo of the fruit fly *Drosophila*. During convergent-extension the shape of the tissue changes dramatically; it narrows in one direction and expands in the other direction by a factor of about two. This process is governed internally and there is no external force on the boundaries of the tissue. In this chapter, we proposed two mechanisms that can generate convergent-extension. In the first mechanism, we impose T1 transitions in the tissue; a randomly selected cell boundary is forced to shrink continuously to a four-fold vertex and expand in the opposite direction. We found that the shear rate of the tissue depends on the orientation of cell bonds that go under T1 transitions. For the situation that selected bonds are randomly oriented, the shear rate is zero, however, for the case that only bonds with certain orientation are selected for T1 transitions, the shear rate is positive. In the second mechanism, we study how cell division without growth generates internal shear. This process is different from what described in Sec. 3.1; the preferred area of the diving cell dose not increase before division and the two daughter cells will have half of the preferred area of the mother cell. After one round of cell division without growth, the total area of the tissue remains unchanged. We show that, similar to the previous case, oriented cell division without growth generates strong convergent-extension and also affect the packing geometry of the network: the percentage of hexagons increases to $\sim 60\%$ during this process.

During development of the *Drosophila* wing, the packing geometry of the tissue changes dramatically. The percentage of hexagons in the tissue increases to $\sim 80\%$. Here, we studied two mechanisms that can change the hexagonal packing of cells significantly. The first mechanism is based on annealing of the grown tissue by changing adhesion on different bonds stochastically. This can result in fluctuation of cell boundaries. For those networks with hexagonal ground state, these fluctuations are biased by the energy minimization toward the hexagonal packing. The percentage of hexagons increases during this process by a factor of two. We also studied how the packing geometry of the tissue changes during shear flow. We impose shear flow in the vertex model by selecting a set of vertices that lie one a line and displace them with constant velocity while relaxing the other vertices in the network. Here, we use no-slip bound-

ary condition which is different from the boundary conditions used for the growth algorithm. This generates a shear flow with a linear velocity profile that is maximum in the center. The percentage of hexagons increases during this process to $\sim 70\%$.

It is proven experimentally that both convergent-extension and hexagonal repacking of tissues, require organization of a set of molecules that assemble asymmetrically in the cells. Cells then become polar in the plane of the tissue due to this asymmetric distribution of molecules, and the polarity of each cell is also aligned with a global direction in the tissue. In this chapter, we developed a theory for the planar cell polarity which includes two interacting molecules. We introduce an energy function to mimic their interactions, which has two terms: The first term describes preferential sorting of these molecules in the cells, and the second term mimics their interactions across the cell boundaries. We showed that starting with a small network and random distribution of these molecules, they assemble such that global order appears in the tissue, however, for larger networks defects of cell polarity appear. We introduced a method to generate long range order in arbitrary large networks using the growth algorithm described in Sec. 3.1. We start with few polar cells and growth the network by repeated cell division. The initial order preserves during growth.

We then study how these polar networks behave under shear flow. We found that the polarity vector of cells reorients, while the general global order is preserved. The angle of the polarity vectors converges to a well-defined steady state value. This suggests that our PCP system together with the vertex model behaves similar to a liquid crystal under shear flow. We introduced a general coarse-grained model for the polarity of cells which is governed by two mechanisms: vorticity and shear. Although vorticity can reorient polarity vector of cells, the shear might influence the orientation of polarity vectors differently. We introduce a phenomenological coefficient describing the coupling between shear and orientation of the polarity vector of cells and give a quantification.

# 5 Compartment Boundaries: Interfaces in Epithelia
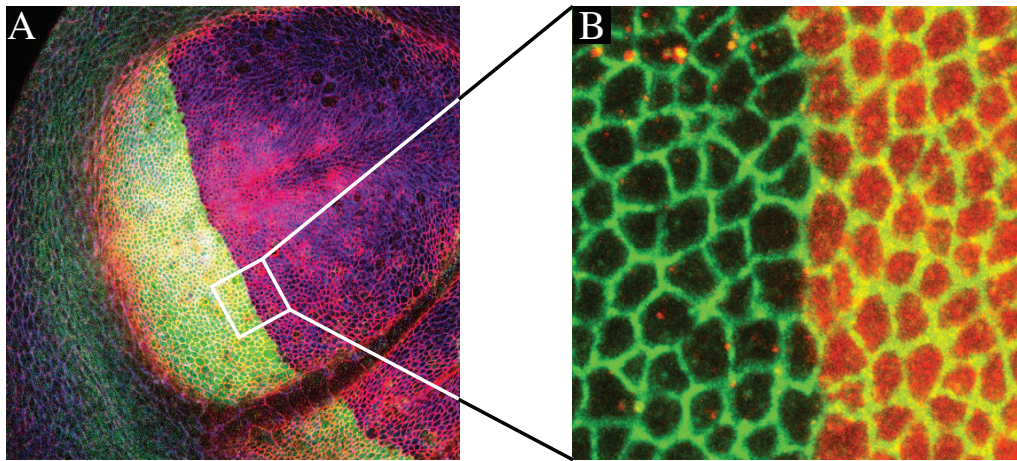
Figure 5.1: Anterior-Posterior compartment boundary. (A) Large scale image of the wing disc marked for engrailed-lacZ reporter activity (red) to identify the posterior compartment. Anterior compartment is shown to the left. (B) Small section of the wing disc near the anterior-posterior compartment boundary. The compartment boundary is straight on both small and large scales (Provided by K. Landsber).

As we discussed in Sec. 1.4, the wing disc of the fruit fly *Drosophila* is subdivided into anterior and posterior compartments. Cells in these compartments remain unmixed during development and are separated by a sharp and straight boundary. As shown in Fig 5.1 A and B, the compartment boundary is straight on both the large-scale and also on the scale of individual cells. Signals produce by cells at the compartment boundaries can result in the local expression of secreted proteins that organize, at long-range, growth and patterning of tissues. Sharp and straight interfaces between compartments are crucial for stabilizing the position of such organizers, and therefore for the precise regulation of tissue growth. Maintaining these boundaries in proliferating tissues requires mechanisms to counteract cell rearrangements caused by cell division; however, the details of such mechanisms remain unclear. In this chapter, we will study

a mechanism that can generate sharp interfaces between two cell populations in proliferating tissues. We will show that increased bond tension along the compartment boundary is sufficient to prevent mixing of the two cell populations. We will show that this mechanism is robust in establishment and maintenance of a sharp boundary on the cell-size length scale, however the overall large-scale shape of the boundary is not well controlled. We will quantify the shape and morphology of the boundary for difference tensions along the compartment boundary and compare them in detail.

5.1 Two-Population Tissue Growth

N=36   N=1152   N=4608
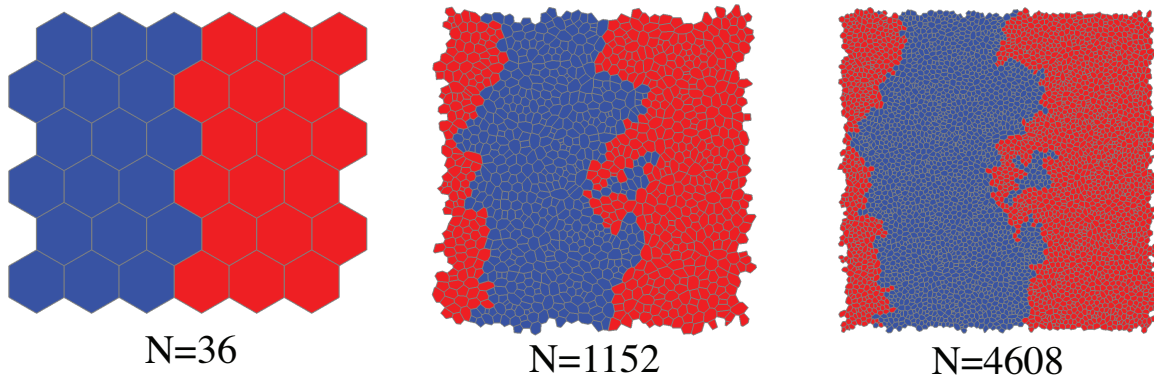
Figure 5.2: Two-population tissue growth. We show three time points of a growth simulation for a two-population cell network. The initial network consists of 36 cells in hexagonal packing divided into two equal compartments, which we label blue for anterior (A) cells and red for posterior (P) cells . As the tissue grows, the two cell populations mix with each other. For plotting purpose each panel is rescaled.

To study compartment boundaries in proliferating tissues, as shown in Fig. 5.2, we choose to label cell populations in our simulations of the vertex model. We will refer to the two resulting populations as 'A' and 'P', and to their dividing interface as "compartment boundary". When a cell divides in this framework, the two daughter cells attain the same linage (A or P) as the mother cell. For simplicity, we assign indices to cells according to their distance from the compartment boundary. Cells that share a boundary with the other population are named A_1 and P_1 and cells that share a boundary with A_1 (or P_1) cells are named A_2 (or P_2).

We can imagine a situation where these two cell populations have different cell mechanics and cell adhesion, and where the tension along the compartment boundary might be different from the tension on the other bonds. Here, we simulate two-population tissue growth for the situation that the tension along the compartment boundary, Λ_{AP}, is the same as the tension on

other bonds in the tissue ($\Lambda_{AP} = \Lambda$) and two cell types have the same parameter values. Starting with 36 cells in hexagonal packing (18 cells of each type) we grow the tissue up to $5,000$ cells. We use parameter values corresponding to case I in Sec. 3.3 ($\bar{\Lambda} = 0.12$, $\bar{\Gamma} = 0.04$). In Fig. 5.2, we show three time points ($N_C = 36$, $N_C = 1152$ and $N_C = 4608$). For this situation the two growing cell populations progressively intermingle as they grow in size, and the interface becomes more and more irregular. Even islands of cell type can be found (surrounded by the other cell type). Note that due to periodic boundary conditions we must have two compartment boundaries in our simulations. These two boundaries are always identical in our simulations and the tension on both boundaries are the same.

5.2   Differential Adhesion in Two-Population Growth
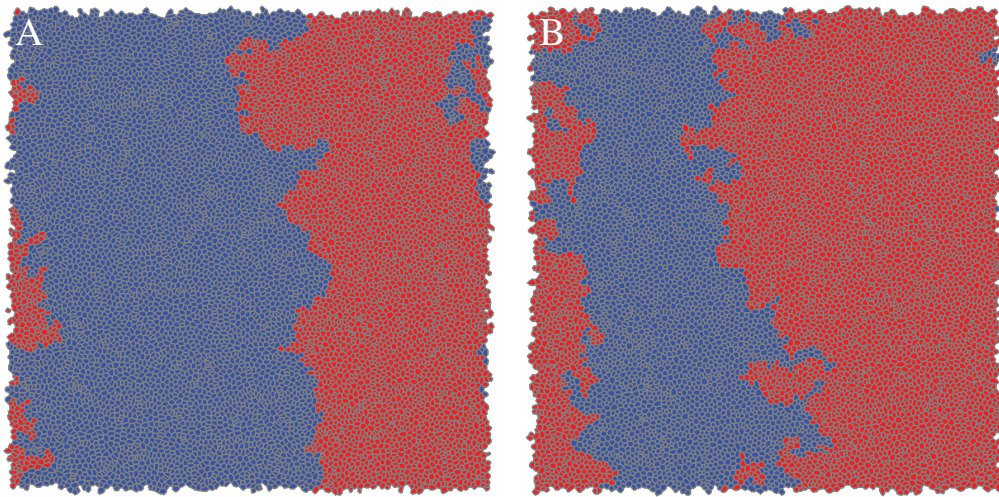
Figure 5.3: Two-population tissue growth such that cell mechanics is different for the two compartments. (A) The parameter values in the anterior compartment (blue) are ($\bar{\Lambda} = -0.12$, $\bar{\Gamma} = 0.08$) and in the posterior compartment are ($\bar{\Lambda} = 0.12$, $\bar{\Gamma} = 0.04$). (B) The parameter values in the anterior compartment (blue) are ($\bar{\Lambda} = 0.24$, $\bar{\Gamma} = 0.02$) and the parameter values in the posterior compartment is similar the posterior compartment in A. In both A and B, the tension along the compartment boundary is the sum of the tension in the A and P compartments.

It is proposed in early 1960s [77]-[79], by Steinberg that difference in cell adhesion between two cell populations can result in cell sorting. This idea is later generalized by Dahmann and Basler [80] to explain formation of compartment boundaries in the *Drosophila* wing disc. This differential adhesion hypothesis might refer to differences in bond tension, as well as differences in perimeter contractility of cells. We do not know *a priori* if cells in the anterior and

posterior compartments of the wing disc have similar adhesion or contractility. We therefore simulate tissue growth for situations that the two compartments have different cell adhesion and perimeter contractility. In these simulations, all cells belonging to the A compartment have similar line tension, $\bar{\Lambda}$ and perimeter contractility, $\bar{\Gamma}$, which are different from the parameter values of cells in the P compartment. Here for simplicity, we assume that the tension along the compartment boundary is the sum of the tensions in the A and P compartments.

Among many possibilities discussed in [98], we show two cases. In both cases, we assume that the line tension and perimeter contractility in the P compartment (red compartment in Fig. 5.3 A and B), are the same as case I discussed in 3.3 ($\bar{\Lambda} = 0.12$, $\bar{\Gamma} = 0.04$). In Fig. 5.3 A and B, we show simulations of two-population tissue growth such that the parameter values in the anterior compartment are ($\bar{\Lambda} = -0.12$, $\bar{\Gamma} = 0.08$) and ($\bar{\Lambda} = 0.24$, $\bar{\Gamma} = 0.02$), respectively. In both cases, differences in adhesion and contractility of cells do not result in formation of a sharp boundary between these two populations. Even for the second case, island of one type forms and cell sorting neither in small-length scales nor in large-length scales emerges in these simulations. Based on these two examples and more detailed studies in [98], we conclude that although differential adhesion between two cell populations can result in cell sorting in some situations, in our simulations of two-population tissue growth, this mechanism can not prevent cell intermingling.

5.3   Increased Interfacial Tension Results in Cell Sorting

As we showed in Sec. 5.1, for two-population tissue growth where all cells are identical and the tension on the compartment boundary is the same as the other bonds in the tissue, these two populations (spatially separated at the beginning of growth) mix together due to cell rearrangements. We also discussed in Sec. 5.2 situations that the two populations have different mechanical properties such as different adhesion and perimeter contractility. This also results in intermingling of cells during growth. Here we introduce a simple mechanism that results in cell sorting during two-population tissue growth. Similar to Sec. 5.1, we assume that the anterior and posterior cells have similar mechanical properties, while the tension along the compartment boundary is higher than the other bonds. This tension is characterized by $\lambda = \Lambda_{AP}/\Lambda$, which is the relative tension along the compartment boundary with respect to the other bonds in the tissue.

We start from initial conditions with two populations (18 cells of each type) in hexagonal packing and grow the tissue for a few generations, varying λ from two to five. In Fig. 5.4, we show the grown networks for different values of λ. Increasing the tension along the compartment boundary by a factor of two is sufficient to establish and maintain a boundary be-
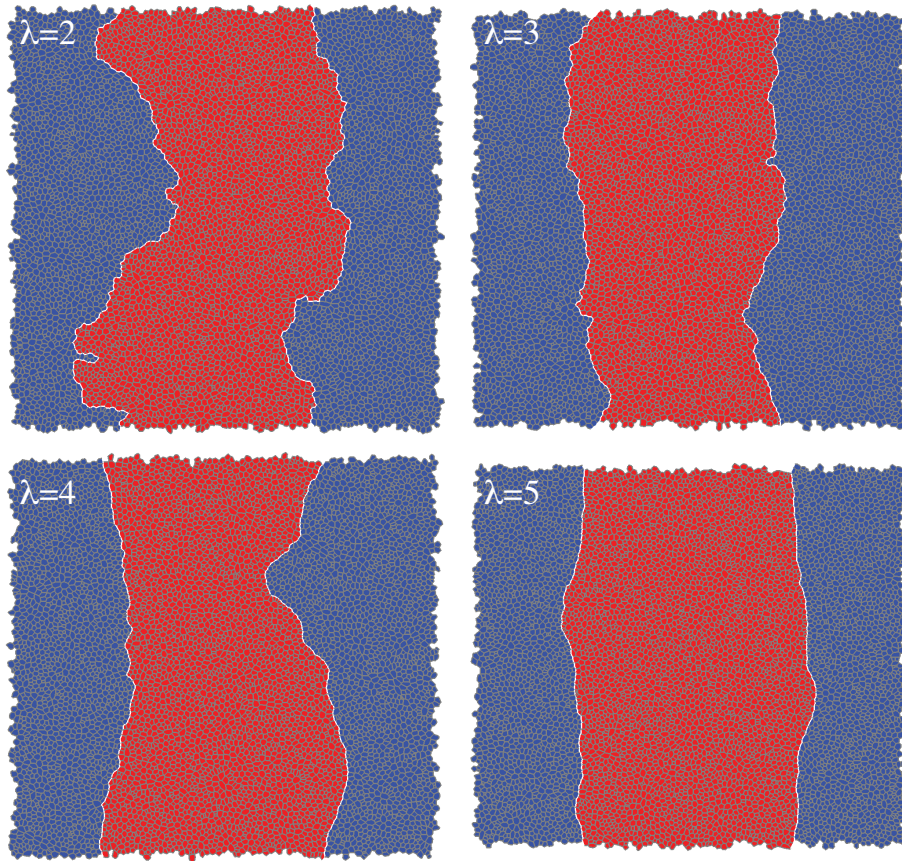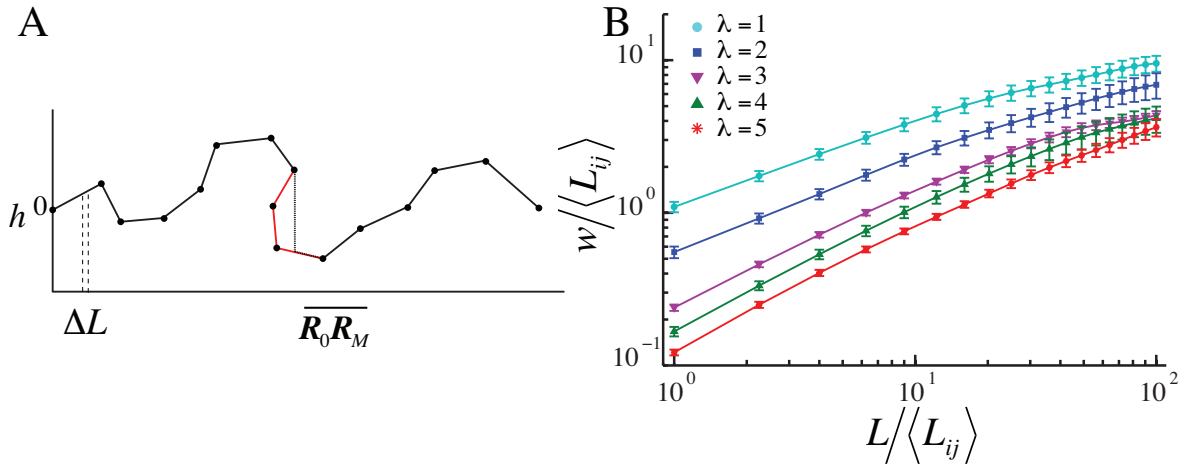
Figure 5.4: Compartment boundaries in growing tissues. Grown tissues of $5,000$ cells where the A and P compartments have the same cell mechanics and line tension ($\bar{\Lambda} = 0.12$, $\bar{\Gamma} = 0.04$). Then tension along the compartment boundary is increased for each case ($\lambda = \Lambda_{AP}/\Lambda$). Increased line tension along the compartment boundary can result in cell sorting as the boundary becomes straighter for higher tensions (larger λ). The boundary is colored in white.

tween two cell populations. However, increasing the tension along the compartment boundary to higher values can generate straighter boundary. For the case $\lambda = 5$, this generates almost straight boundary, however, the boundary fluctuates on large-scales. Note that decreasing the tension along the compartment boundary clearly results in cell mixing; the two cell populations tend to expand their region of contact. Also note that increasing the tension along the compartment boundary has effect on cell morphology near the boundary; the angle between two adjacent compartment cell boundaries is higher than the angle between two adjacent A/A or P/P cell boundaries, which is 120°. In [98], we studied two-population growth with increased tension along the compartment boundary for other choices of parameter values ($\bar{\Lambda}$, $\bar{\Gamma}$). We found that for the same increment in the tension along the compartment boundary, the boundary is straighter for situations that the shear modulus of the network is lower. We conclude that in-

creased tension along the compartment boundary is a robust mechanism that can generate sharp and straight boundaries.

5.4   Shape and Roughness of Interfaces in Developing Tissues

Figure 5.5: (A) Schematic of quantification of roughness for the compartment boundaries. The compartment boundary is divided in equal intervals ΔL. Regions of overhangs (red part) in the compartment boundary are replaced by a single bond bypassing the overhang (dotted line). (B) Roughness of the compartment boundaries. Normalized roughness of the compartment boundary to the average bond length, $w/\langle L_{ij} \rangle$, as a function of normalize distance $L/\langle L_{ij} \rangle$ for different tensions along the compartment boundary, $\lambda = \lambda_{AP}/\Lambda$.

We introduced in the previous section, a mechanism that can generate interfaces in two-population tissue growth. To study the shape and morphology of these boundaries, we quantified the roughness of the compartment boundary. We measure the roughness of an interface by the variance w^2 as a function of the distance L along the interface axis over which the variance is determined. The shape of the interface is defined as a series of vertex positions $\mathbf{R}_i = (x_i, \ y_i)$, with $i = 0, ..., M$, along the compartment boundary that are connected by straight bonds. The axis $\overline{\mathbf{R}_0 \mathbf{R}_M}$ of the compartment boundary is the line connecting the end points $\mathbf{R}_0$ and $\mathbf{R}_M$. The piecewise linear boundary line is discretized in equal intervals ΔL along the axis $\overline{\mathbf{R}_0 \mathbf{R}_M}$. This defines the orthogonal distances h_k from the axis at the discretization points. Here $k = 1 \cdots N_0$ where N_0 is the number of discretization points. For averaging length $L = N \Delta L$, the height

variance is

$$w^2 = \frac{1}{N_0 - N + 1} \sum_{k=1}^{N_0-N+1} \left(\frac{1}{N} \sum_{i=0}^{N-1} (h_{k+i} - \overline{h_k})^2 \right), \tag{5.1}$$

where $\overline{h_k} = (\sum_{i=0}^{N-1} h_{k+i})/N$ is the average height at the segment of length L starting with discretization point k. The value of w as a function of L characterizes interface roughness. Note that for situations with an overhang in the shape of the compartment boundary, we replace the overhang by a single bond bypassing the overhang. In Fig. 5.5 A, we plot the roughness of the compartment boundary for the mechanism described in Sec. 5.3 in a log-log plot for different values of the relative tension, along the compartment boundary, $\lambda = \Lambda_{AP}/\Lambda$. Our data suggests that the roughness scales as, $w = w_0 L^\eta$, where η is the roughness exponent. For $\lambda \geq 2$, the roughness exponent is similar for different values of tension along the compartment boundary ($\eta \sim 0.7$), however, w_0 is different. For increasing tension λ, w_0 decreases, which indicates that the boundary becomes straighter.

5.5 Summary

In this chapter we introduce a mechanism that can prevent cell mixing in two-population tissue growth. For the condition that all cells are mechanically identical, stochastic cell division results in mixing of these two populations. However, if the tension along the compartment boundary increases with respect to the other bonds in the tissue, cells sort out during growth and a sharp interface forms. Higher tension along the compartment boundary results in the formation of a straighter boundary. We characterized the shape of the compartment boundaries by measuring the roughness of the boundary. We observed that the roughness scales as power-law with respect to the length of segments of the compartment boundary. Although this mechanism can generate straight compartment boundary at small-length scales, on large scales the shape of the boundary fluctuates. This suggest that other mechanisms are involving in shaping the compartment boundaries in developing tissues.
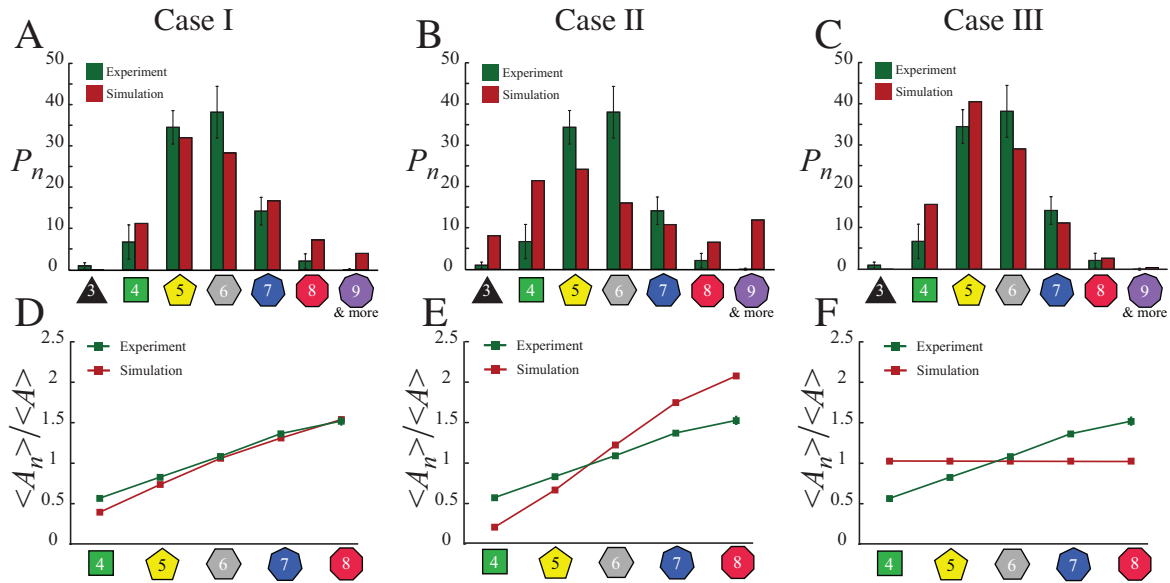
6 Comparison Between Theory and Experiment

In the previous chapters we have developed a vertex model to study cell mechanics and cell adhesion. We introduced a growth algorithm and we showed that repeated cell division generates a specific pattern of cells. The stationary pattern generated by this method depends on the biophysical parameters of the model. We introduced two sets of numbers to characterize these patterns. These numbers, which count the frequency and area variability of different classes of polygons, show significant differences for simulations with different parameters $\bar{\Lambda}$ and $\bar{\Gamma}$. This indicates that comparing these numbers with ones measured in experiments may help us to quantify biophysical parameters of tissues using the methods introduced in App. E to quantify cell packing geometries in experimental images.

In this chapter we will compare experiments with our theoretical results. We first will compare cell packing between experiment and simulations and we will determine a parameter region in our phase diagram for which the packing geometry of simulated tissues is similar to ones observed in the *Drosophila* wing disc. We then will compare the area variability of cells in experiment and theory, showing that there is a smaller region, which has an overlap with the packing region, such that the cell morphology is similar in experiments and simulations. Finally, we will compare displacements of vertices due to laser ablation of cell boundaries, and we will show that the agreement between theory and experiments is limited to a very small region in the phase diagram (which has an overlap with the other two regions). Case I, which is discussed in previous chapters, lies in the overlap of all regions.

Having developed such a quantitative method to measure cell mechanics in tissues, we will test our hypothesis about increased tension along the compartment boundary. We will first quantify cell mechanics in the anterior and posterior compartments of the wing disc. We then will quantify the tension along the anterior-posterior compartment boundary, and show that the tension along the boundary is greater by a factor of four than the other boundaries in the network. We will finally simulate clone cells in proliferating tissues and show that, similar to the experiments, the cells will remain cohesive during growth.

# 6.1   Cell Shape and Cell Packing

Figure 6.1: Comparison of cell packing and tissue morphology between theory and experimental measurements of the wing disc. (A), (B) and (C) Red bars are stationary distributions of neighbor numbers P_n. The green bars in each panel indicate the experimentally determined distribution of neighbor numbers in the wing disc. (D), (E) and (F) Average areas of different polygon classes normalized to the average area of cells in the network, $\langle A_n \rangle / \langle A \rangle$, for cases I, II, and III (red lines). These lines are compared to the experimentally determined values for the wing disc (green lines).

As we discussed in Sec. 3.2, repeated cell division generates disorder in cell packing that leads to the formation of specific patterns of cells. We showed in Sec. 3.3 that these patterns are significantly different for different sets of biophysical parameters; namely line tension and perimeter contractility. We simulate tissue growth for three choices of $\bar{\Lambda}$ and $\bar{\Gamma}$ (case I: $\bar{\Lambda} = 0.12$, $\bar{\Gamma} = 0.04$, case II: $\bar{\Lambda} = 0$, $\bar{\Gamma} = 0.1$ and case III: $\bar{\Lambda} = -0.85$, $\bar{\Gamma} = 0.1$). Each pattern is then characterized by two set of numbers: P_n, the fraction of n-sided cells and $\langle A_n \rangle / \langle A \rangle$, the average area of n-sided cells normalized to the average area of all cells. Cell shape and packing geometry are different in these three cases and the quantified characteristic numbers show the differences clearly. This suggests that by comparing the values of P_n and $\langle A_n \rangle / \langle A \rangle$ for each case with values measured in an epithelia (such as the wing disc of the fruit fly *Drosophila*), we can estimate biophysical parameters of the tissue. To quantitatively describe cell packing geometry in the wing disc, we analyzed 1738 cells from different confocal images of living wing discs expressing E-cadherin-GFP by using an automated image-processing algorithm to outline the network of apical junctions. From this network, we identify individual cells, cell

boundaries, and three and four-fold vertices. We define a four-fold vertex as a region of contact between four cells, the size of which does not exceed the average width of cell boundaries in the image. This cutoff corresponds to 2 pixels – approximately 20% of the average cell-boundary length. We use this information to determine the fraction of cells with different numbers of neighbors. In Fig. 6.1 A-C these data are shown by green bars alongside the values obtained by simulations. Comparing the experimental values for the wing disc of *Drosophila* and the simulation values for cases I-III, we conclude that case I and III have almost the same packing geometry as the wing disc, but that case II has a clearly different distribution of n-sided cells compared to experiment. In case II, the frequency of six-sided cells is half of the observed one in experiments, and the frequency of three-sided and cells with nine or more neighbors is much higher than experimental measurements.

We also calculate the average area of n-sided cells, normalized to the average area of all cells for the wing disc epithelium. In the wing disc, average cell areas increase with neighbor number (see Fig. 6.1 D-F, green lines). The average area of hexagonal cells is slightly larger than the average area of cells in the epithelium (108%). The average area of five-sided cells is 82% of the average area of all cells and that of seven sided cells is 136%. Area variation, as a simple measure of tissue morphology, shows clear differences in experiment from those obtained by simulations in cases II and III. In case III, cell areas apparently do not correlate at all with neighbor number, unlike those of the real tissue. In case II the average areas vary more strongly with side number than observed in experiment. Of these three cases, case I produces morphologies and packing geometries closest to that of the real tissue.

We now wonder which parameter regions in our phase diagram generate packing geometry and tissue morphologies similar to the wing disc. To do this, we first perform growth simulations for different sets of parameters (black dots in Fig. 6.2) to generate stable network configurations. For each pair of parameter values we calculate the converged values of the fraction P_n for different class of polygons, as well as the normalized area variation $\langle A_n\rangle/\langle A\rangle$. We quantify the differences between theoretical and experimental results by the quantities Δ_P and Δ_A. The difference between the experimentally observed neighbor number distribution P_n^{exp} and the one obtained by simulations P_n^{sim} is characterized by the sum of the squared deviations, $\Delta_P = \sum_{n=3}^{\infty}(P_n^{sim} - P_n^{exp})^2$. The red region in Fig. 6.2 indicates those parameter values for which $\Delta_P < 0.004 \simeq 0.1(\Delta_{max} - \Delta_{min})$, which Δ_{min} and Δ_{max} denote the minimal and maximal values of Δ_P found in our simulations. Similarly, the difference between experimentally determined average areas of n-sided cells and those obtained in simulations $\langle A_n^{sim}\rangle$ is quantified by $\Delta_A = \sum_{n=3}^{\infty}(\langle A_n^{sim}\rangle/\langle A^{sim}\rangle - \langle A_n^{exp}\rangle/\langle A^{exp}\rangle)^2$. The blue region in Fig. 6.2 corresponds to $\Delta_A < 0.07$. Those parameter values that lie in the overlap of the blue and red regions in Fig. 6.2 generate similar tissue morphology and cell packing to the wing disc of the fruit fly *Drosophila*.
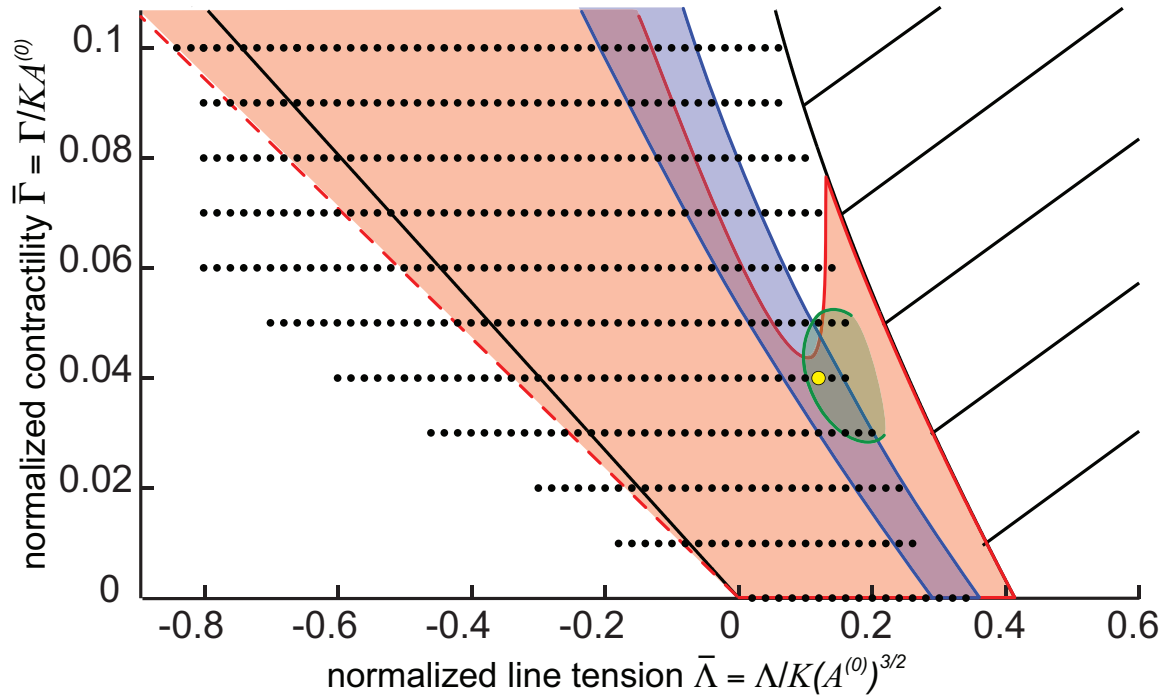
Figure 6.2: Parameter regions matching observed tissue properties. Properties of cell packing
for different values of the parameters $\overline{\Lambda}$ and $\overline{\Gamma}$ (line tension and contractility). Simu-
lations of tissue growth were performed for different parameter values (black dots).
In the red outlined region, the distribution P_n of n-sided cells in simulations is sim-
ilar to the one observed in the wing disk of *Drosophila*. In the blue outlined region,
the relative areas of n-sided cells match those observed in experiments. Comparing
simulations of laser ablation with experiments, we find quantitative agreement in
the green outlined region. The yellow dot indicates case I.

6.2   Displacements Upon Laser Ablation

To investigate the interplay of forces acting at the junctional network of epithelial cells in the
wing disc of *Drosophila*, we perturb the stable network by ablating a section of individual
cell boundaries with a UV laser beam (focused on a spot of 1.3 μm diameter in the plane
of epithelial junctions). A single cell-boundary was cut, and the resulting movements of the
network, visualized with E-cadherin-GFP, were observed over several minutes (see Fig. 6.3
A). In response to the cut, E-cadherin-GFP fluorescence disappeared from the center of the
cut cell boundary, and the vertices at both ends moved from their initial positions, increasing
their distance from the cut point. Subsequently, the vertices relaxed to new stable positions.
The distance between the vertices at the ends of the cut-bond increased as $d - d_0 = d_1(1 - \exp(-t/\tau))$ for which $d_0 + d_1$ is the final distance and d_0 is the initial distance between vertices.
In Fig. 6.3 B, the change in distance $d - d_0$ as a function of time is shown (average over 20
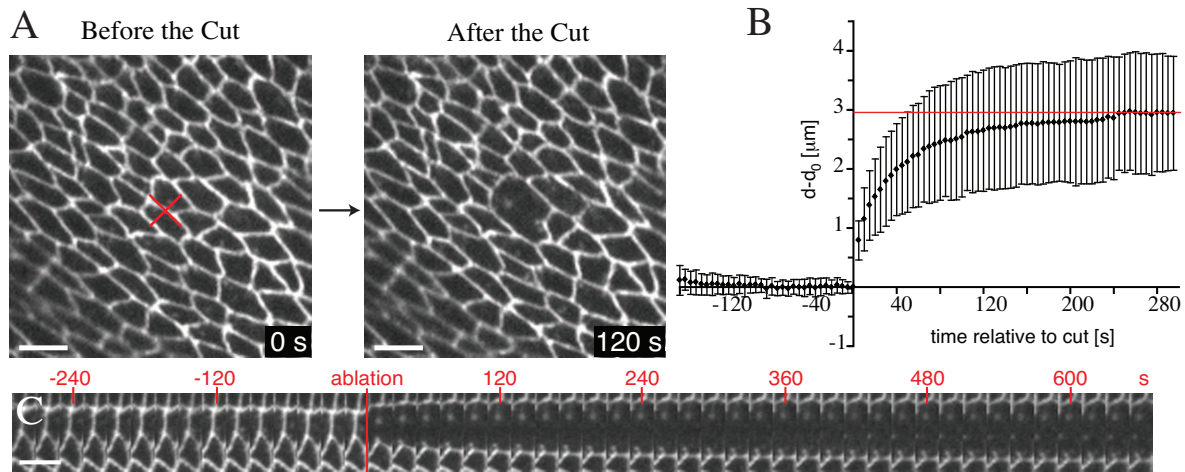
Figure 6.3: Laser ablation of cell boundaries in the wing disc. (A) Single confocal images of a
GFP-E-cadherin-expressing wing disc during a laser-ablation experiment. The first
image shows the epithelial network before the cut, and the second one shows the
same network 120 s after the cut. The red cross in the first image of (A) indicates
site of ablation. (B) Change in distance $d - d_0$ between vertices at the ends of the
ablated bond as a function of time, averaged over 20 experiments. (C) A sequence
of cropped images of the ablated region, separated by 20 s. The time in seconds is
indicated; scale bars represent 5 μm.

experiments). The relaxation time τ varied between 13 and 94 s for different experiments. In
Fig. 6.3 C, a sequence of cropped images near the ablation region is shown to illustrate how the
distance between vertices increases after ablation.

   We discussed in Sec. 3.6 that, due to removal of a cell boundary, vertices surrounding the
cut-bond move in an anisotropic manner. To quantify the anisotropy of the displacements, we
measure the normalized combined area changes and normalized combined perimeter changes
of the two cells sharing the cut-bond. Due to uncertainty in experiment about the effect of laser
ablation on the contractility of the two cells sharing the cut-bond, we introduced two scenarios
to mimic laser ablation in simulations. In scenario I, we assume that laser ablation only results
in removal of the cut-bond and the contractility of the cut cells remains unaffected. In scenario
II, we assume both the tension of the cut-bond and the perimeter contractility of the cells sharing
the cut-bond is affected by the ablation. We also discussed in Sec. 6.1 that for parameter values
corresponding to case I the growth algorithm generates cell packing geometries similar to the
wing disc epithelium. We ask wether the parameter values corresponding to case I can generate
the same type of movements as ones observed in experiment and which scenario can mimic best
the ablation experiment. We quantify the combined area changes and the combined perimeter
changes of the cut cells in experiments and plot them in Fig 6.4 as a function of normalized
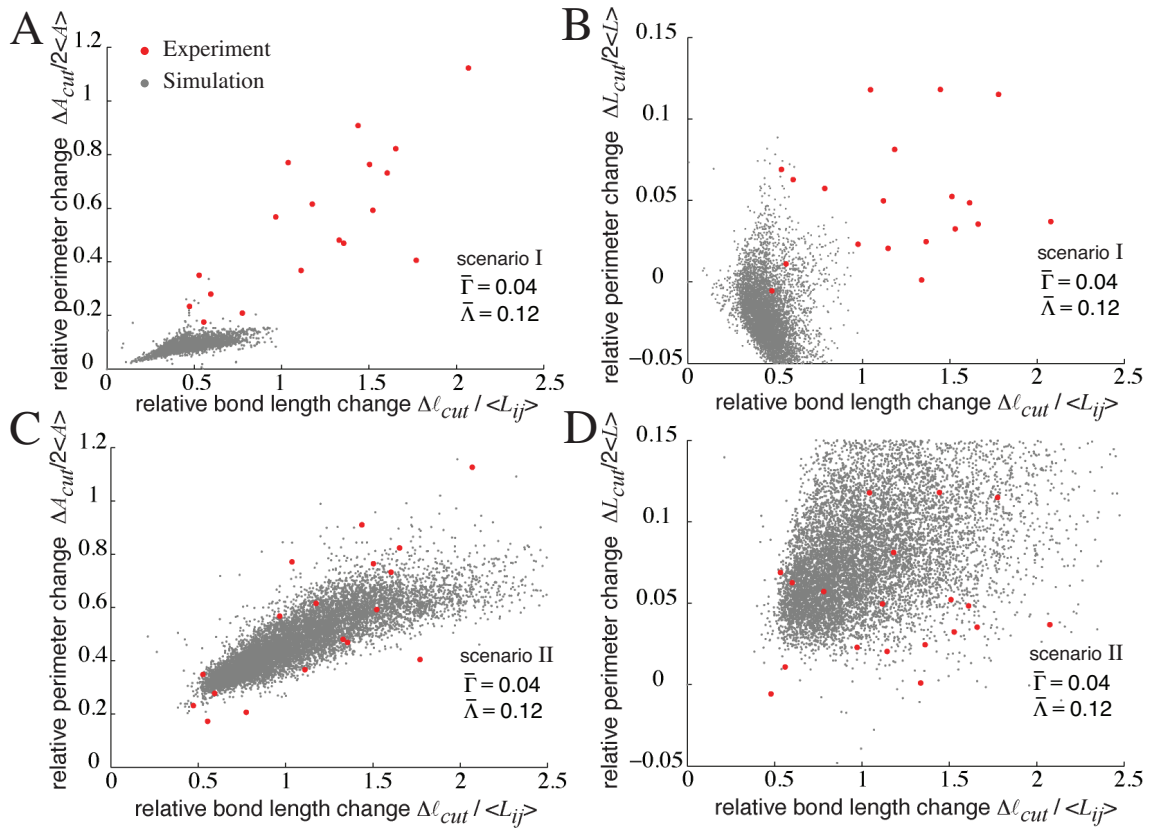
Figure 6.4: (A and C) Changes in the combined areas ΔA_{cut} of cells adjacent to an ablated bond, relative to twice the average cell area $2\langle A \rangle$, are plotted as a function of the relative increase in the distance between the vertices of the cut-bond $\Delta \ell_{cut}/\langle L_{ij} \rangle$. (B and D) Relative change of the perimeter $\Delta L_{cut}/2\langle L \rangle$ of the cells adjacent to the cut-bond; $\langle L \rangle$ is the average cell perimeter. In (A)-(D), red dots show results from 20 experiments and gray dots show the results of simulations with different parameter values for laser ablation.

bond length changes (red dots) together with the data for case I (gray dots) for two different scenarios. It is evident that scenario II (which assumes both the tension in the cut boundary and the contractility of the two cells adjacent to the cut-bond affected by ablation), can mimic the experimentally observed anisotropic movements due to laser ablation.

We are wondering if the vertex model can reproduce not only the displacement of vertices of the two cells sharing the cut-bond, but in general the displacement field of all vertices in the tissue due to ablation of a cell boundary. To quantify the displacement of vertices in the field of cells surrounding the cut site, we used a polar coordinate system in which r denotes the radial distance from the cut point and θ denotes the angle with respect to the orientation of the cut boundary. The angle of the cut boundary thus corresponds to $\theta = 0$ and π. For each vertex, we determined the radial and tangential components D_r and D_θ of the displacement

vectors $\boldsymbol{D}$ (see Fig 6.5 A). As shown in Fig 6.5 A, we group vertices with different colors according to their normalized distance from the cut center $\bar{r} = r/\langle L_{ij} \rangle$. We first measure the displacements D_r and D_θ of vertices before ablation (for $0 < \bar{r} < 8$) to quantify the level of fluctuations and plot them in Fig. 6.5 B and Fig. D.1, respectively. We then quantify the position of vertices before and after ablation when they relax to their new positions and determine the displacements D_r and D_θ. They are plotted in Fig. 6.5 C and Fig. D.1 (colors as in Fig. 6.5 A). The radial displacement D_r depends on the angle θ relative to the orientation of the cut boundary. Displacements are maximal for vertices lying along the cut-bond axis. The radial displacements D_r of those vertices lying in a direction perpendicular to the cut boundary (i.e., near $\theta = \pi/2$ or $3\pi/2$) were small and did not exceed background noise. Radial displacements decreased quickly for increasing distance r from the cut-bond. At distances beyond six average edge lengths, they only marginally exceeded the background noise (compare the top and bottom panels in Fig. 6.5 C). Tangential displacements D_θ were smaller and decreased more quickly with increasing distance from the cut site (see Fig. D.1).

We then simulate laser ablation using scenario II for parameter values corresponding to case I, calculating radial displacements of vertices at different distances from the bond with respect to the polar angle θ, and comparing them to observed displacements. Like the area and perimeter changes, the radial and tangential displacements of vertices D_r and D_θ in the surrounding network were quantitatively reproduced by our simulations (compare Fig. 6.5 C and D; Fig. D.1 A and B). As in the experimental data, maxima of D_r occur at angles 0 and π, whereas maxima of D_θ occur at $3\pi/4$ and $7\pi/4$ (Fig. 6.5 D; Fig. D.1 B). For radial displacements, the magnitude of maximal average displacements, as well as their scatter, agreed quantitatively with those found in experiments, decreasing by similar amounts over similar distances. For tangential displacements, agreement was also good. Note, however, that for small r the average of the amplitudes differs by a factor of two. More experimental data points would be necessary for determining whether this difference is significant or not.

We showed in Sec. 3.6 that for the case that the parameters of the tissue are slightly different from case I ($\bar{\Lambda} = 0.12, \bar{\Gamma} = 0.02$), the laser ablation simulations result in significantly different values of ΔA_{cut} and ΔL_{cut}. We conclude that the laser ablation simulation is very sensitive to the physical parameters of the model. To study the range of parameter values in our phase space that can generate the same type of movements due to laser ablation as ones observed in experiment, we simulate laser ablation for all parameter values in Fig. 6.2. To compare the result of simulations and experiment, we fit a straight line to the determined variation of normalized area change ΔA_{cut} as a function of normalized bond-length increase $\Delta l_{cut}/\langle L_{ij} \rangle$. We quantify the difference that is between experiment and simulation by Δ_L; it is the absolute difference between the slopes of the fit. For scenario I (see Fig. 3.8 A) that we only set to zero the line tension $\overline{\Lambda}_{ij}$ of the cut boundary, there is no agreement between experiment and simulations for
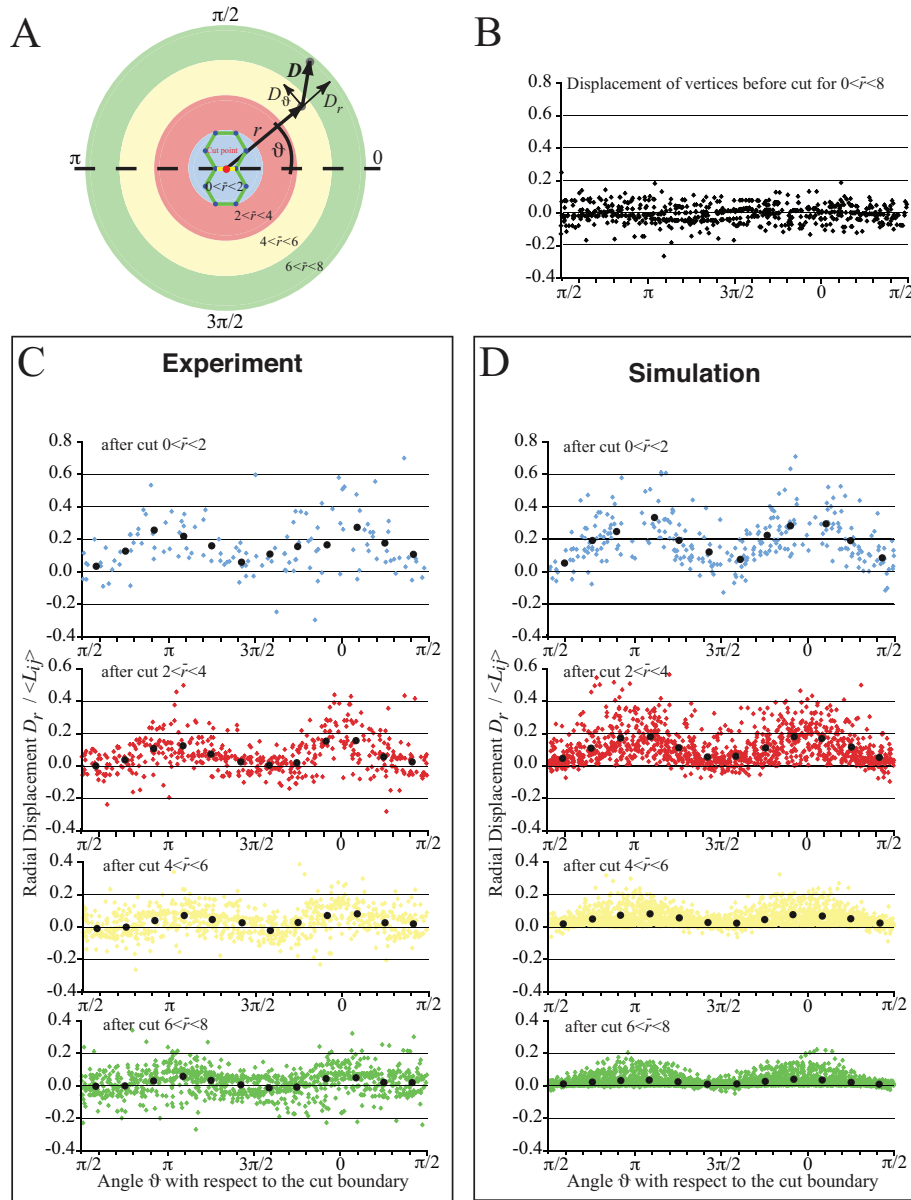
Figure 6.5: (A) Schematic representation of positions and displacements during a laser ablation experiment. The direction of the cut boundary is indicated by a dashed black line. The position of a vertex before ablation is described by its radial distance r from the cut point and its angle θ with respect o the cut-bond orientation. The movement of the vertex from its initial position to its new position after the cut is described by its displacement vector $\boldsymbol{D}$. This vector can be decomposed in radial and tangential components D_r and D_θ. Vertices are grouped in concentric rings according to their normalized distance from the cut point $\bar{r} = r/\langle L_{ij} \rangle$ relative to the average bond length $\langle L_{ij} \rangle$. (B) Experimental radial displacement of vertices before laser ablation. (C) Radial displacements D_r of vertices normalized to the average bond length $\langle L_{ij} \rangle$ observed in 20 laser ablation experiments shown as a function of θ. The colors correspond to the distance ranges. Black dots show the average displacements determined by grouping vertices in bins of $\pi/6$ radians. (D) Normalized radial displacements obtained in 50 simulations of bond ablation with a network corresponding to case I, scenario II.

any $(\overline{\Lambda}, \overline{\Gamma})$. Removal of both line tension of the cut boundary and the contractility of adjacent cells sharing the cut boundary is necessary for achieving quantitative agreement between simulations and experiments (scenario II). The green region in Fig. 6.2 corresponds to $\Delta_L < 0.07$, with an additional constraint that average perimeter change is positive.

6.3   Morphology of Compartment Boundaries
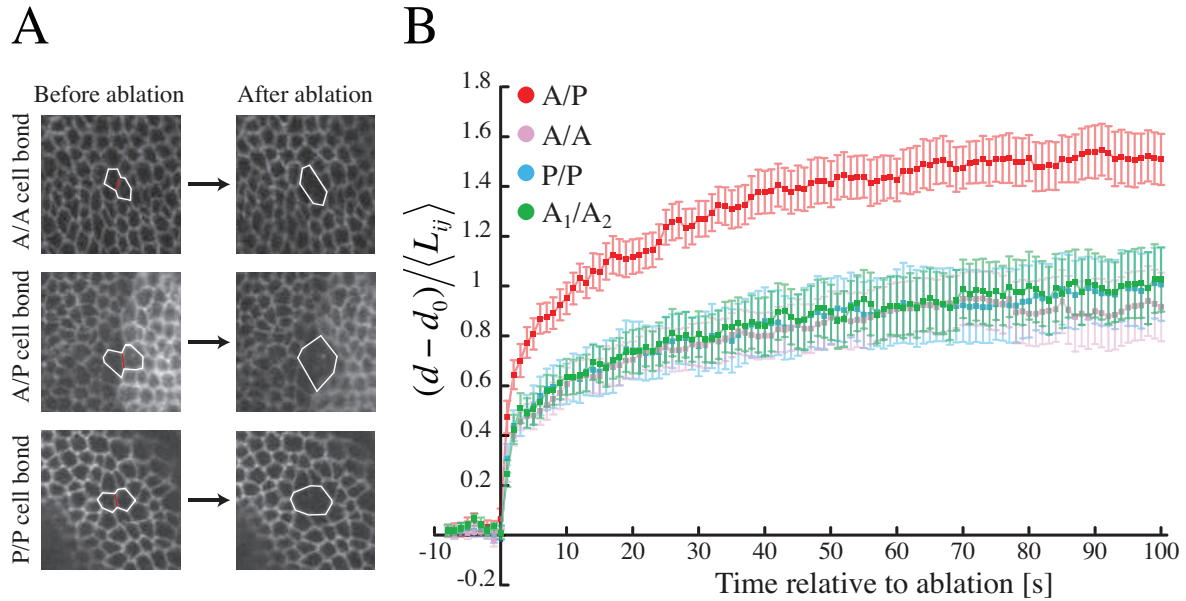
Figure 6.6: Laser ablation of compartment boundaries. (A) Images of E-Cadherin-GFP expressing wing discs before and after single cell bonds were ablated. Cells of the posterior compartment are labeled by another marker (GFP-gpi under the control of engrailed-GAL4) to distinguish from anterior cells. (B) Change in distance between vertices at the ends of ablated cell bonds (normalized to the average cell bond length in the tissue) , $(d - d_0)/\langle L_{ij} \rangle$, as a function of time for bonds between cells of the population indicated. A_1/A_2 refers to cell bonds between A1 cells and their anterior cell neighbors. Mean and standard error of the mean are shown. Number of experiments were: A/P, $n = 24$; A/A, $n = 24$; P/P, $n = 18$; A1/A2, $n = 16$.

Quantification of tension along the anterior-posterior compartment boundary

We showed in Sec. 5.3 that increased tension along the compartment boundary can result in establishment and maintenance of sharp interfaces between two cell populations in growing tissues. We also showed that using the laser ablation technique we can precisely quantify tensions in the tissue. To test whether the tension on the anterior-posterior compartment boundary in the wing disc is different from other bonds in the tissue, we performed laser ablation experiments

for bonds along the compartment boundary. Single cell bonds were cut and the displacement of vertices of neighboring cells, visualized by E-cadherin-GFP, were recorded over several minutes. The posterior compartment was visualized by expressing other proteins (GFP-gpi under control of the engrailed gene using the GAL4/UAS system).

In Fig. 6.6 A, we show the network of cells before and after ablation for bonds that are shared between A/A cells, P/P cells and A/P cells (bonds along the compartment boundary). We highlight boundaries of the two cells sharing the cut-bond in white and the cut bond in red. For A/A and P/P cuts, the displacements is anisotropic, however for A/P cuts it generates stronger anisotropic movements of the vertices surrounding the cut-bond. The displacements of the two vertices of the cut-bond were analyzed. The rate and extent of vertex displacement was indistinguishable for ablation of bonds between A/A cells and P/P cells located away from the anterior-posterior compartment boundary (see Fig. 6.6 B pink and blue lines). By contrast, ablation of the bonds between adjacent anterior and posterior cells gave rise to significantly larger displacements (see Fig. 6.6 B, red lines). To test whether the increased line tension is localized along the A/P compartment boundary or whether there exist a more complex pattern of tension in the tissue, we performed laser ablation for boundaries between A_1/A_2 cells, shown in Fig. 6.6 B (green line). There is no significant difference between A_1/A_2 cuts and the normal A/A and P/P cuts. These results indicate strongly that the anterior-posterior compartment boundary is under more tension than normal bonds in the tissue, and that this higher tension is only present along the compartment boundary.

We introduced a dimensionless parameter $\lambda = \Lambda_{AP}/\Lambda$ in Sec. 5.3 that is the ratio of the tension along the anterior-posterior compartment boundary to the tension of all bonds in the tissue (here bonds in the anterior and posterior compartments have the same tension). To quantify the value of λ in experiment, we calculate the displacements of vertices surrounding the cut-bond before and after ablation, as done in Sec. 6.2. We only consider those vertices with distances from the cut site less than two times the average bond length ($\bar{r} = r/\langle L_{ij} \rangle \leq 2$). In Fig. 6.7 A, B and C, we plot the radial component of the displacement field normalized to the average bond length in tissue (see Sec. 6.2 for details) as a function of the angle with respect to the cut-bond for A/A, A/P and P/P cuts, respectively (red dots; the average of the scatter is shown by black dots). Laser cuts of the compartment boundaries clearly generate greater anisotropic movements of the vertices surrounding the cut-bond. In Fig. 6.7 D-F we show the normalized radial displacement, $D_r/\langle L_{ij} \rangle$, for simulations of the A/P compartment boundary for three cases: $\lambda = 1$, 4 and 7, respectively. The case $\lambda = 1$ is identical to A/A and P/P cuts in the wing disc. For $\lambda = 7$ the anisotropy of the movements is much stronger than that observed in the wing disc. However, $\lambda = 4$ generates anisotropic movements in good agreement to movements observed in ablation of the A/P compartment boundary in the wing disc, and we thus conclude that the tension along the compartment boundary is increased four times compared to
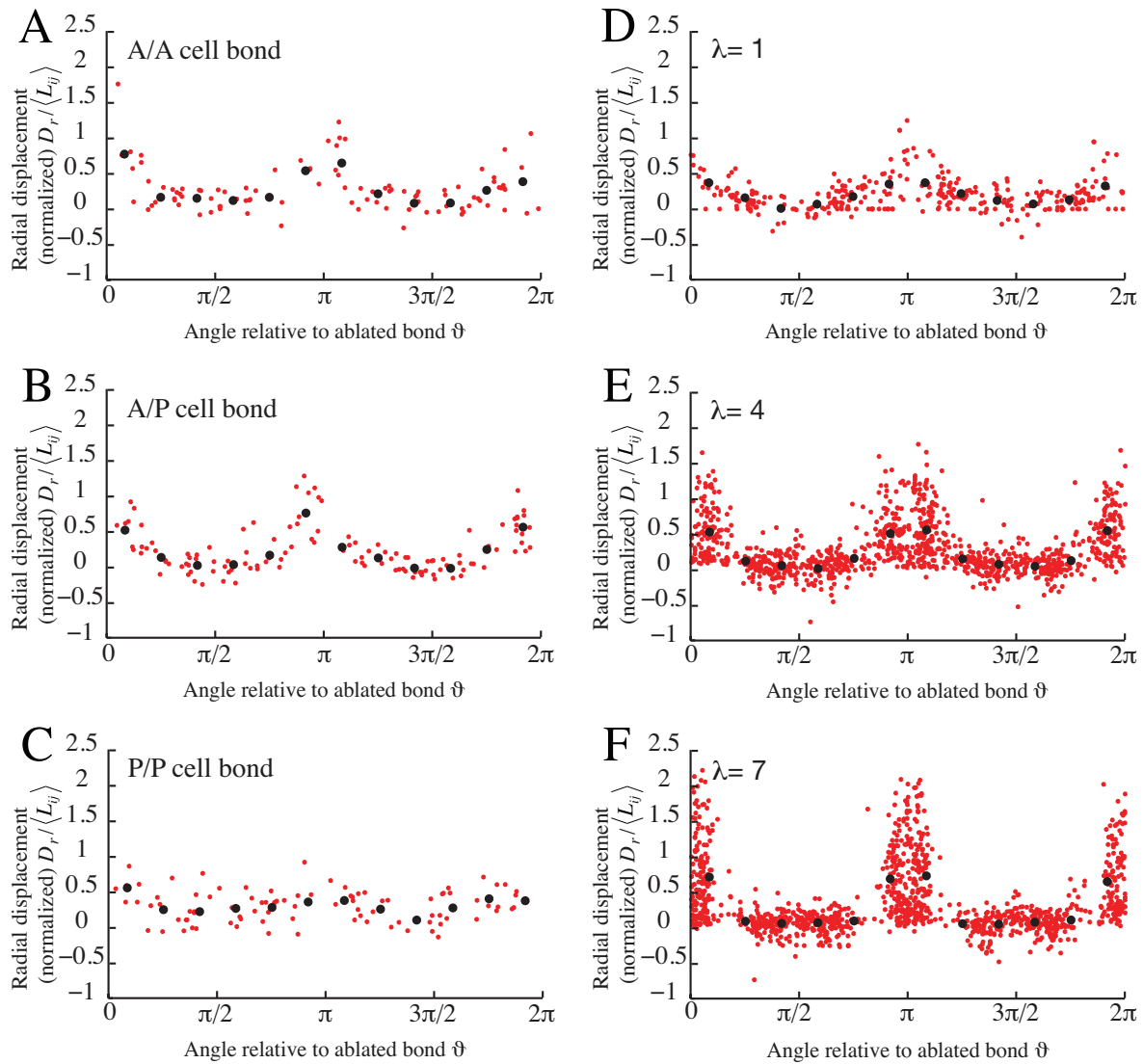
Figure 6.7: Anisotropic displacement upon laser ablation for the compartment boundary. (A), (B) and (C) Radial displacement of vertices due to laser ablation of cell bonds, normalized to the average bond length, $D_r/\langle L_{ij}\rangle$, as a function of the angle with respect to the cut-bond for bonds shared between two anterior cells, A/A, an anterior and a posterior cells, A/P, and two posterior cells, P/P, respectively. (D), (E) and (F) Radial displacement of vertices normalized to the average bond length in laser ablation simulations of the compartment boundary for $\lambda = \Lambda_{AP}/\Lambda = 1, 4$ and 7 as a function of the angle with respect to cut-bond. The black dots indicate the average. Only vertices that their distance from the cut site is less than two times the average bond length are plotted.

the tension of other bonds in the tissue.
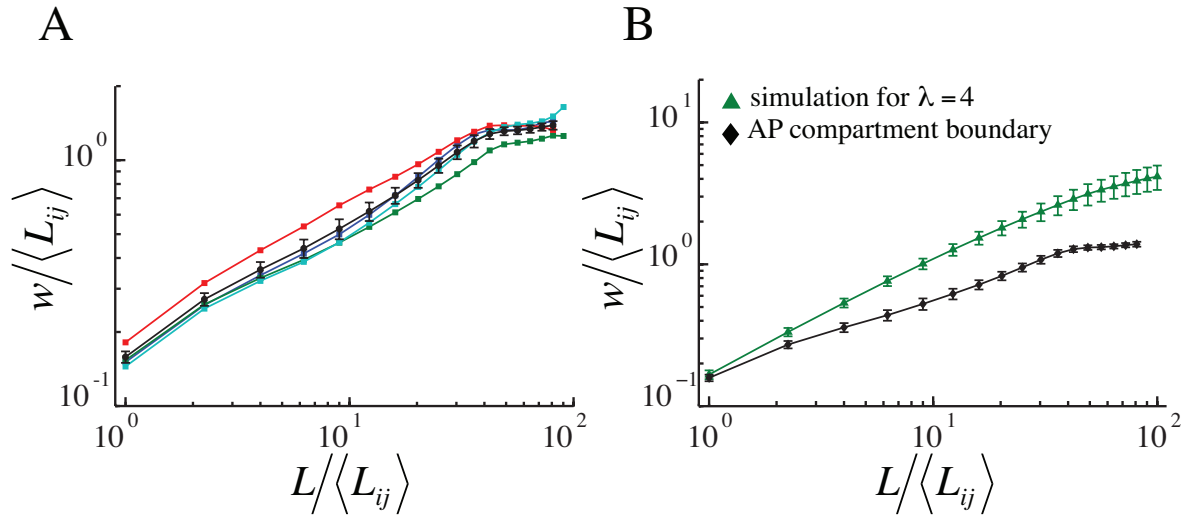
Figure 6.8: Roughness of the compartment boundary. (A) Roughness of the anterior-posterior compartment boundary for four different experiments. The average is shown in black. (B) Comparison of the roughness of the compartment boundary between experiment and simulation for $\lambda = 4$.

We now wonder if increased tension along the compartment boundary by a factor of four is sufficient to generate an interface with the same morphology as ones observed in experiments. In Sec. 5.4, we introduced a method to quantify the roughness and shape of compartment boundaries. We processed four wing discs and extract the shape of the anterior-posterior compartment boundaries throughout the tissue. In Fig. 6.8 A, we show the width of the compartment boundary normalized to the average bond length, $w/\langle L_{ij}\rangle$, as a function of the normalized length along the boundary, $L/\langle L_{ij}\rangle$, for each wing disc. We show the average of the normalized width for these four discs in black. The morphology of the anterior-posterior compartment boundary is highly reproducible among these discs. In Fig. 6.8 B, we show the roughness of the compartment boundary in simulations of $\lambda = 4$ together with the average of the roughness of anterior-posterior compartment boundary in the *Drosophila* wing disc. At small scales (the length of few cell bonds), the roughness of the anterior-posterior compartment boundary is remarkably similar to the roughness obtained in the simulations for $\lambda = 4$. However, for larger scales, the anterior-posterior compartment boundary is more straighter than the simulated one for $\lambda = 4$; even it is straighter than simulations of $\lambda = 7$, where the tension along the compartment boundary is increased by a factor of seven. Our results, then indicate that a four-fold increase in cell bond tension along the compartment boundary, can largely account for the sorting of the cells at the anterior-posterior compartment boundary and determines the small length-scale behavior. Additional mechanisms might operate to improve the straightness of this boundary at large

scales.

6.4 Cell Clones in Growing Tissues
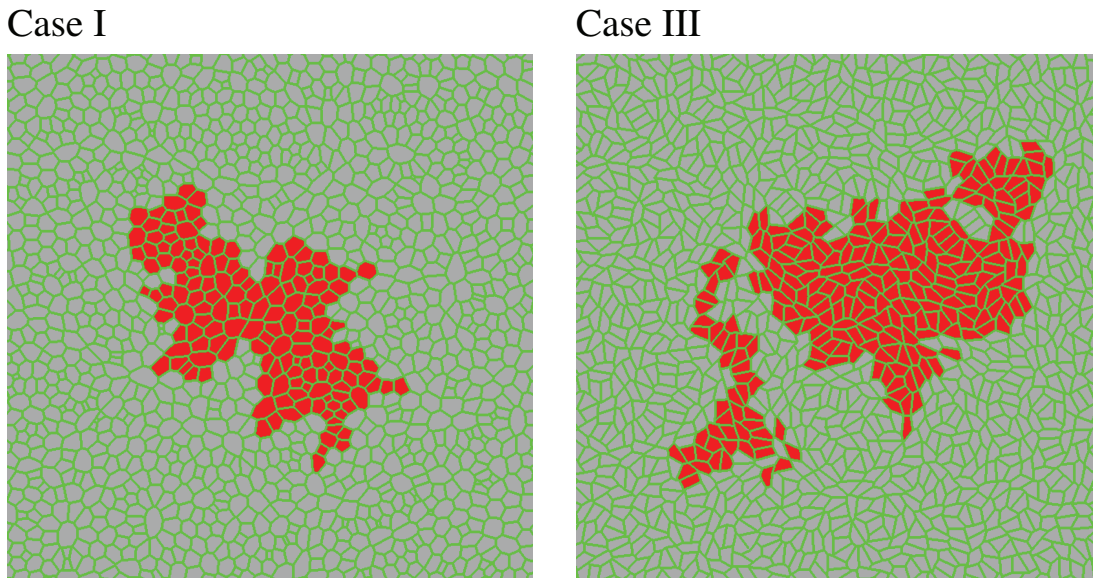
Case I   Case III

Figure 6.9: Example of clone cells in growing networks for case I and III. In case I, clone cells remain contiguous during growth, in contrast to clone cells in case III, where they disperse and are invaded by unrelated cells.

A clone of cells is generated in biology by modifying a single cell at an early stage of development such that it expresses a certain fluorescent molecule, while all other cells in the tissue are not able to produce this specific molecule. These molecules are not diffusible to other cells and therefore they only transfer to daughter cells of a cell having this molecule, through cell division. In the wing disc it is shown that clones of cells do not disperse from each other during proliferation [89]-[90]. T1 transition is the most important mechanism that can disperse clone cells. The fact that clone cells are not dispersed in the wild-type wing disc suggests that T1 transitions do not happen very frequently.

We now wonder if the parameter values that we find for case I (Sec. 3.3) can predict this experimental observation. We also wonder if our model predicts disperse clones for case III, where the model parameters are such that the network is liquid, and the rate of T1 transitions is higher compared to case I. We perform growth simulations for cases I and III during which we keep track of the identity of cells that originate from a specific cell in the initial hexagonal network. We color these cells in Fig. 6.9 red. In simulations of case I, few T1 transitions occur as the network grows (37 transitions per 100 cell divisions), and clones remain cohesive. In contrast, in the case of a soft tissue (case III), 146 T1 transitions occur per 100 cell divisions,

clones are invaded by unrelated cells (see Fig. 6.9). This suggests that the tendency for clones to remain contiguous during proliferation is a consequence of physical cellular properties.

6.5 Summary

We introduced in Sec. 3.3, three cases with distinct cell shape and packing geometries. These cases correspond to different set of parameter values indicating that cell shape and packing geometry is determined by biophysical properties of cells. In this chapter, we used our theoretical results to quantify tension and perimeter contractility of cells in the *Drosophila* wing disc. We compared the packing geometry of these three cases with the quantified packing of the wing disc and we found that, case I ($\bar{\Lambda} = 0.12$, $\bar{\Gamma} = 0.04$) and case III ($\bar{\Lambda} = -0.85$, $\bar{\Gamma} = 0.1$) generate similar packing geometries. However, comparing the area variability of polygon classes of these cases with experiments, we found that only case I generates cellular morphologies similar to the wing disc. We conclude that of these three cases, only case I generates similar cell shape and packing geometries to the ones observed in the wing disc. To study how cell shape and packing geometry are influenced by the physical parameters of the model and find regions of parameter values corresponding to the wing disc, we systematically change these parameter values and performed growth simulations. For each set of model parameters we compare neighbor number distribution between experiment and simulation and we find that for those parameter values lie in the red region in Fig. 6.2, the packing geometry is similar in simulations and experiment. From this analysis , we conclude that the distribution of neighbor numbers does depend on physical parameters, but there is an extended region that is consistent with experiments. Comparing area variability in simulations and experiment, we find that only a subset of parameter choices is consistent with the cell shapes and network morphologies observed in the proliferating wing disc, which is outlined in blue in Fig. 6.2. Area variability constrains parameter values corresponding to the wing disc more than neighbor number distribution.

We have performed laser-ablation experiments of cell boundaries to study the force balances described by our vertex model and to independently determine parameter values. Laser-induced cutting of cell junctions causes the vertices at either end to move apart. This results in anisotropic displacements of vertices in the surrounding network; displacements are maximal for those vertices lying along the axis of the cut bond. Comparing these experiments to simulations shows that only a small range of parameters (green outlined region of Fig. 6.2), which includes those of case I, is consistent with the observed movements. We conclude that laser-ablation experiments constrain parameter values corresponding to the wing disc the most among the other measurements. Moreover, we showed that our vertex model can well reproduce displacements of all vertices in the tissue. We compared the displacement field in experiment and simulations of case I and we found that our theoretical results match well with the exper-

imental displacements. We also showed that simulations of laser ablation can be mimicked by removing both the tension in the ablated boundary and the contractility of the two cells adjacent to the cut boundary.

We introduced a mechanism in Chap. 5 to establish a compartment boundary between two cell populations in growing tissue, by increasing the cell-bond tension along the compartment boundary. We examined this hypothesis in experiment for the anterior-posterior compartment boundary in the wing disc using laser ablation. We performed ablation for bonds that are shared between two anterior cells, two posterior cells as well as the bonds shared between an anterior and posterior cells. We found that the tension is indeed increased along the compartment boundary. To quantify the tension along the compartment boundary, we compared the displacement field of vertices surrounding the cut bond in experiment and simulations. We found that ablation of the compartment boundary generates more anisotropic movements compared to the ablation of other bonds, and we found that simulations with increased tension by a factor of four along the compartment boundary can well reproduce the displacements observed in experiment. We then compared the shape and morphology of the anterior-posterior compartment boundary with the ones generated in simulations for four-fold increase tension along the compartment boundary. We found that on small scales, our model generates remarkably similar morphologies to experiment, however, on larger length-scales the anterior-posterior compartment boundary is straighter than our simulations. We conclude that other mechanisms are also involved in establishment of the compartment boundary and influence largely the overall shape of the boundary.

7 Conclusions and Outlook

Most species develop from a fertilized egg cell and during development, different organs with variety of shape, size and functionality form. Mechanisms that control shape and morphology of different organs are still not clear. For the past decades, biologist identified complex networks of signaling molecules that are involved in development of tissues. However, the response of cells to such a signaling network is only limited to processes such as cell division, cell death, cell growth, cell migration and cell shape changes. These mechanisms are tightly controlled by cell mechanics and cell adhesion, which requires careful study of cell mechanics in tissues.

In this thesis, we developed a framework to study cell mechanics and cell interactions in two-dimensional tissues, so called epithelia. Epithelial cells are connected to each other via adhesive molecules and establish a junctional adheren network near their apical region. In order to describe such a network, we used a vertex model, in which each cell is approximated by a polygon (vertices connected by straight bonds). Since cell shape relaxes much faster than other developmental processes such as cell division and cell rearrangement, on time scales shorter than cell division time scale and longer than cell-shape relaxation, the junctional network is stable and the total force on each vertex is zero. The forces we consider here can in our simple description be represented by an energy function. Our energy function has three terms regarding area elasticity, perimeter contractility and cell-cell adhesion. We studied the ground state properties of the model and we showed that depending on physical parameters of the model, there is a phase transition from solid hexagonal network to soft networks, where the ground state is degenerate.

We introduced a cell division algorithm in our vertex model, based on quasistatic changes of cell properties. This algorithm has two main steps: (i) A growing phase of the dividing cell that the preferred area of the cell is doubled in a few steps while minimizing the energy after each increment. (ii) By the end of this growing phase, we introduce a new boundary at a random angle passing through the cell center. Repeating this process we can grow the tissue starting from a small number of cells up to an arbitrary size. Cell packing generated by this algorithm are characterized according to the fraction and average area of different polygon classes. We found that depending on model parameters, distinct patterns of cells emerge with different packing geometries and morphologies. We studied phase transitions for growing networks, which are

far from equilibrium and we found that there is a transition from solid to soft networks, for which the transition line falls on the line that we found for the ground state phase transition. During growth, local stresses are induced in the network due to cell division that result in cell shape changes as well as junctional remodeling. We studied how the dynamics of junctional remodeling in growing networks is affected by cell mechanics and we found that the rate of junctional remodeling increases for decreasing line tension, while the rate of cell death increases for increasing line tension.

We also studied the displacement field of vertices due to local perturbations such as removal of cell boundaries. We showed that this results in anisotropic movement of vertices around the removed boundary. Vertices in the direction of the cut bond moves outward, however, vertices perpendicular to the cut bond moves slightly inward. We studied two scenarios for removal of a cell boundary. In the first scenario, we only remove the tension of the boundary leaving the two cells next to the boundary otherwise unaffected. In the second scenario, we remove both the tension on the boundary and also the perimeter contractility of the two cells adjacent to the cut boundary. We found that the second scenario generates greater anisotropy than the first one. We also studied how mechanical parameters of the tissue might affect the displacements due to removal of a cell boundary. We found that slight changes in the parameter values of the model generates significantly different displacements around the cut bond, which shows that this analysis is quite sensitive to cell mechanics and cell adhesion in tissues and can be used as a probe to quantify precisely forces in the tissues.

Many developmental processes occur in absence of cell division, that affect tissue shape and morphology. Two examples of such processes have been studied in this thesis: convergent-extension and hexagonal repacking. During convergent-extension the shape of the tissue changes dramatically; it narrows in one direction and expands in the other direction by a factor of about two, which is governed internally. We studied two mechanisms that can generate internal shear in grown networks: junctional remodeling and cell division without growth. The later process is different from what described in our growth simulations; the preferred area of the diving cell dose not increase before division and the two daughter cells will have half of the preferred area of the mother cell. We found that to shear the network effectively, the junctional remodeling should be oriented. We also found that one round of oriented cell doubling without growth generates internal shear in the tissue. During repacking, specifically in the *Drosophila* wing, the packing geometry of the tissue changes dramatically and the percentage of hexagons increases by a factor of two. We studied two mechanisms that can result in hexagonal packing: annealing and shear flow. Both mechanisms occur during development of the *Drosophila* wing. We introduced annealing in the vertex model by randomly changing the adhesion of cell boundaries, while relaxing the network. This can result in fluctuation of cell boundaries. For those networks with hexagonal ground state, these fluctuations are biased by the energy minimization toward

the hexagonal packing. We found that the percentage of hexagons can increase to $\sim 80\%$ during annealing. We also introduced shear flow in the vertex model by imposing shear on vertices lie in the middle of the network, while relaxing the other vertices. Shear flow also influences the packing geometry of the network and the hexagonality increases to $\sim 70\%$.

Processes such as convergent-extension and repacking are controlled by a network of interacting proteins that are involved in planar polarization of tissues. Planar cell polarity is a tissue-level phenomenon that coordinates cell behavior in epithelia. Planar polarity is established by a molecular organization that includes an asymmetric distribution of these proteins within cells. The distribution of these proteins in a given cell determines of the polarity of neighboring cells. We developed a model to study planar cell polarity in the context of vertex model. Our model includes two type of molecules that interact across cell boundaries and inhibit each other within cells. We showed that starting from a random distribution of these molecules in cells, for small networks long-range polarity order emerges, however for larger networks defects of planar polarity appear. We found that if we grow a small polarized network, the initial polarity preserves during growth and we can generate a network of arbitrary size with long-range order. We then studied how these polar networks behave under shear flow. We found that the polarity vector of cells reorients, while the general global order is preserved and the angle of the polarity vectors converges to a well-defined steady state value. This behavior of our model is similar to liquid crystal physics We developed a general coarse-grained model for the polarity of cells which is governed by two mechanisms: vorticity and shear. Although vorticity can reorient polarity vector of cells, the shear might influence the orientation of polarity vectors differently. We introduce a phenomenological coefficient describing the coupling between shear and orientation of the polarity vector of cells and give a quantification.

Finally we compare our theoretical results with the experimental ones to quantify for the first time cell mechanics and cell adhesion in tissues such as the wing disc of the fruit fly *Drosophila*. To study how cell shape and packing geometry are influenced by the physical parameters of the model and find regions of parameter values corresponding to the wing disc, we systematically change these parameter values and performed growth simulations. For each set of model parameters we compare neighbor number distribution between experiment and simulation and we find that for those parameter values lie in the red region in Fig. 6.2, the packing geometry is similar in simulations and experiment. From this analysis , we conclude that the distribution of neighbor numbers does depend on physical parameters, but there is an extended region that is consistent with experiments. Comparing area variability in simulations and experiment, we find that only a subset of parameter choices is consistent with the cell shapes and network morphologies observed in the proliferating wing disc, which is outlined in blue in Fig. 6.2. Area variability constrains parameter values corresponding to the wing disc more than neighbor number distribution. We also have performed laser-ablation experiments of

cell boundaries to study the force balances described by our vertex model and to independently determine parameter values. Comparing these experiments to simulations shows that only a small range of parameters (green outlined region of Fig. 6.2). We conclude that laser-ablation experiments constrain parameter values corresponding to the wing disc the most among the other measurements.

Using these techniques, we studied mechanisms that result in establishment and maintenance of compartment boundaries between two cell populations in developing epithelia. For the condition that all cells are mechanically identical, stochastic cell division results in mixing of these two populations. However, if the tension along the compartment boundary increases with respect to the other bonds in the tissue, cells sort out during growth and a sharp interface forms. Higher tension along the compartment boundary results in the formation of a straighter boundary. We examined this hypothesis in experiment for the anterior-posterior compartment boundary in the wing disc using laser ablation. We performed ablation for bonds that are shared between two anterior cells, two posterior cells as well as the bonds shared between an anterior and posterior cells. We found that the tension is indeed increased by a factor of four along the compartment boundary. We then compared the shape and morphology of the anterior-posterior compartment boundary with the ones generated in simulations for four-fold increase tension along the compartment boundary. We found that on small scales, our model generates remarkably similar morphologies to experiment, however, on larger length-scales the anterior-posterior compartment boundary is straighter than our simulations.

Our vertex model can be used as a basis for further investigations on how networks of signaling molecules control cell mechanics and consequently final shape, size and morphology of tissues. In this thesis, we introduced a model to describe planar polarization of tissues, however we did not discuss how these molecules that are involved in tissue polarity control cell mechanics or cell division. There are evidences that planar polarity proteins tightly control tissue properties [83], such as packing geometry of tissues [81], cell division orientation [82], cell migration [84] and convergent-extension [85]-[87]. It is recently proposed that cell packing geometry influences planar cell polarity signaling and irregular cell packing results in misorientation of polarity [88]. The detailed mechanisms of these processes are poorly understood. In future, we can use the vertex model together with our planar polarity model to study these mechanisms in details.

We showed theoretically and experimentally that the anterior-posterior compartment boundary is under higher tension compared to the other boundaries in the tissue. However, our further analysis on the morphology and shape of the compartment boundary, showed that the anterior-posterior compartment boundary in the wing disc is straighter than the ones in simulations. This indicates that although four-times increase in the tension along the compartment boundary is sufficient to generate small-length scale morphology, there are other mechanisms that influence

the overall shape of the compartment boundary. These mechanisms are completely unknown. Moreover, establishment of the dorsal-ventral compartment boundary is still not clear [89]-[91]. It is worthwhile to test whether the tension along the dorsal-ventral compartment boundary is increased using laser ablation techniques and how this is comparable to the tension along the anterior-posterior compartment boundary.

Finally our vertex model can be extended to study more complicated developmental processes such as "cell competition" [92]-[95]. Cell competition is a type of short-range cell-cell interaction described in *Drosophila*, in which cells expressing different levels of a particular protein are able to discriminate between their relative levels of that protein in such a way that one of the cells disappears from the tissue, whereas the other not only survives but also proliferates to fill the space left by the disappearing cells. This was first discovered in experiments in which the division rate of wing cells was altered by using Minute mutations [92]. The Minute mutations in *Drosophila* produce a dominant growth defect and result from inactivating mutations in one of many different ribosomal proteins. Cells homozygous[1] for a Minute mutation cannot manufacture proteins and therefore die; this is not due to cell competition, but rather cell-autonomous apoptosis. However, cell competition can occur when cells heterozygous[2] for a Minute mutation, which are viable, are found next to wild-type cells. When flies containing Minute heterozygous cells together with wild-type cells were created, Minute heterozygous cells disappeared by apoptosis because of the presence of surrounding wild-type cells, despite the fact that they would have been viable on their own.

---

[1]A cell is homozygous for a particular gene when identical alleles of the gene are present on both homologous chromosomes.

[2]A cell is heterozygous for a particular gene when two different alleles occupy the gene's position on the homologous chromosomes.

A   Conjugate Gradient Mehod

iteration i

steepest descent method, iteration i+1

conjugate gradient method, iteration i+1
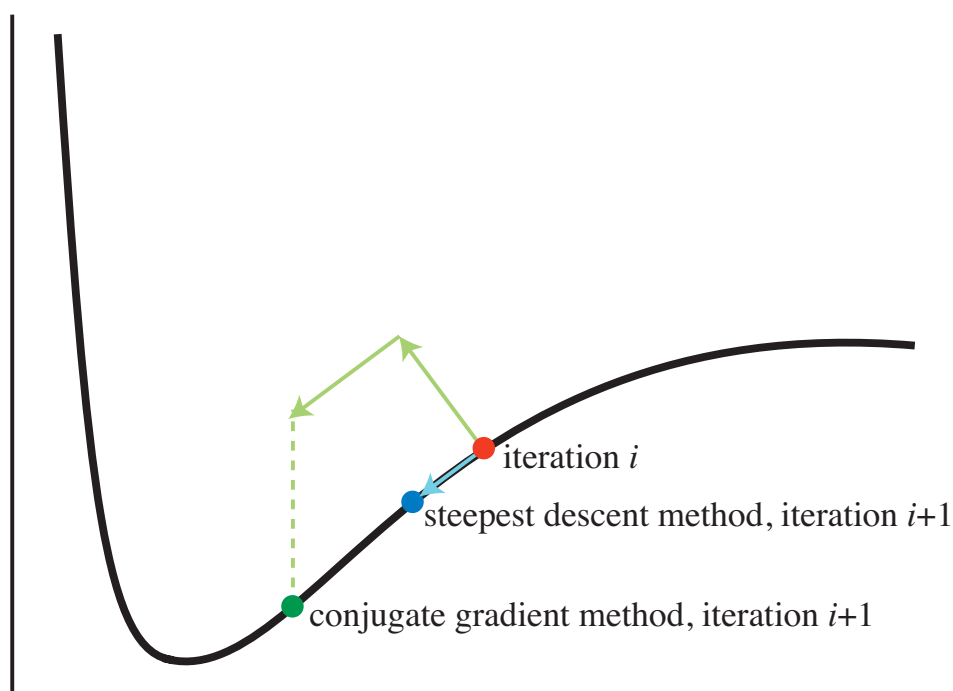
Figure A.1: Simple comparison between steepest descent method and conjugate gradient. In the steepest descent method, we only move slightly in the opposite direction of gradient of the function in each iteration; However in conjugate gradient method we move more efficiently in each iteration using conjugate vectors.

The simplest method of minimizing a function $f(\mathbf{x})$ with N independent variables ($\mathbf{x} = (x_1, \cdots, x_N)$) knowing the gradient of the function is the Steepest Descent method. In this method, we start from an initial point $\mathbf{x}_0$ and in each iteration, we move along the direction $-\nabla f$ until we are close enough to the solution. Although the steepest descent method has the advantage of numerical stability, but it performs many small steps in going down a long, narrow valley, even if the valley is a perfect quadratic form that makes this method inefficient from computational point of view. We therefore need to use a more sophisticated method such as Conjugate Gradient method that includes two basic steps: adding an orthogonal vector to

the direction of search for minimum and then move in a direction nearly perpendicular to this vector The conjugate gradient method is an algorithm for the numerical solution of particular systems of linear equations, namely those whose matrix is symmetric and positive definite. The conjugate gradient method is an iterative method, so it can be applied to sparse systems which are too large to be handled by direct methods such as the Cholesky decomposition. Such systems arise regularly when numerically solving partial differential equations. The conjugate gradient method can also be used to solve unconstrained optimization problems such as energy minimization. This difference between steepest descent method and conjugate gradient method is illustrated in Fig. A.1.

In any iterative minimization method, the new position of variables at step i, is updated such that

$$\mathbf{x}^{i+1} = \mathbf{x}^i + \lambda_i \mathbf{h}^i, \tag{A.1}$$

where λ_i is a scalar parameter and $\mathbf{x}^i$ is the position of the variables at step i. The direction $\mathbf{h}^i$ is the search direction towards the minimum. For the steepest descent method this direction is given by the negative of the gradient of the function, $\mathbf{h}^i = -\nabla f(\mathbf{x})$. However, for the conjugate gradient method, this direction is given via a simple recursion

$$\mathbf{h}^{i+1} = -\nabla f(\mathbf{x}^{i+1}) + \gamma_i \mathbf{h}^i. \tag{A.2}$$

There are two slightly different ways of definition of γ_i; the first definition was given by Fletcher and Reeves [96]

$$\gamma_i = \frac{\nabla f(\mathbf{x}^{i+1}).\nabla f(\mathbf{x}^{i+1})}{\nabla f(\mathbf{x}^i).\nabla f(\mathbf{x}^i)}, \tag{A.3}$$

where $\mathbf{x}^i = (x_0^i, \cdots, x_N^i)$. Later, Polak and Ribiere [97] introduced a new definition for γ_i

$$\gamma_i = \frac{(\nabla f(\mathbf{x}^{i+1}) - \nabla f(\mathbf{x}^i)).\nabla f(\mathbf{x}^{i+1})}{\nabla f(\mathbf{x}^i).\nabla f(\mathbf{x}^i)}. \tag{A.4}$$

For certain type of energy functions, the Polak-Ribiere algorithm is less efficient than Fletcher-Reeves algorithm. The conjugate gradient method is very efficient compared to steepest descent method, however for some type of energy functionals it sometimes can step so far into a very strong repulsive energy range where the gradient on this point is almost infinite.

B Cell Packing Geometry

Table B1. Polygon Class Distributions								
	P_3	P_4	P_5	P_6	P_7	P_8	$> P_8$	$\langle n \rangle$
Case I	0.11	11.29	32.10	28.39	16.79	7.31	4.02	5.90
Case II	8.21	21.63	24.39	16.18	10.92	6.63	12.05	5.95
Case III	0.05	15.73	40.62	29.20	11.25	2.70	0.45	5.46
Wing disc	1.0 ± 0.77	6.78± 4.18	34.61± 4.06	38.28± 6.29	14.28± 3.36	2.17± 1.76	0.06± 0.24	5.51

Table B2. Area Variation						
	$\langle A_3 \rangle / \langle A \rangle$	$\langle A_4 \rangle / \langle A \rangle$	$\langle A_5 \rangle / \langle A \rangle$	$\langle A_6 \rangle / \langle A \rangle$	$\langle A_7 \rangle / \langle A \rangle$	$\langle A_8 \rangle / \langle A \rangle$
Case I	0.05	0.42	0.80	1.08	1.30	1.47
Case II	0.03	0.20	0.65	1.21	1.73	2.06
Case III	1.0	1.0	1.0	1.0	1.0	1.0
Wing disc	0.42 ± 0.14	0.56 ± 0.02	0.82 ± 0.01	1.08 ± 0.01	1.36 ± 0.02	1.52 ± 0.05

Table B3. Number of T1 and T2 Transitions		
	T1 Transition per 100 Divisions	T2 Transition per 100 Divisions
Case I	37	12
Case II	16	3
Case III	146	0

C   Numerical Analysis of Phase Transitions in Tissue Growth
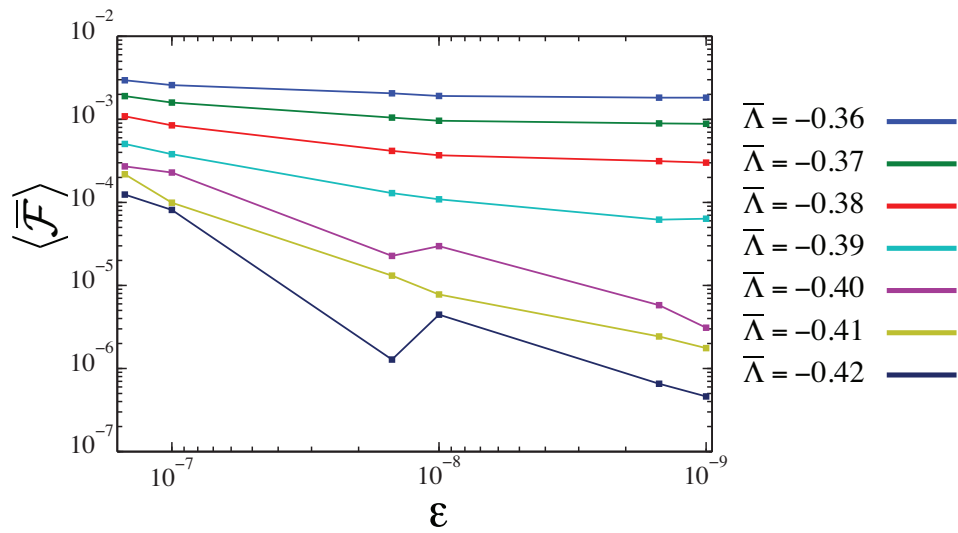
Figure C.1: Numerical analysis of phase transitions for growing tissues. Logarithmic plot of the converged value of the order parameter as a function of ϵ, the threshold for the conjugate gradient minimization method. This is plotted for different values of $\bar{\Lambda}$ and $\bar{\Gamma} = 0.05$.

D   Displacements Upon Laser Ablation
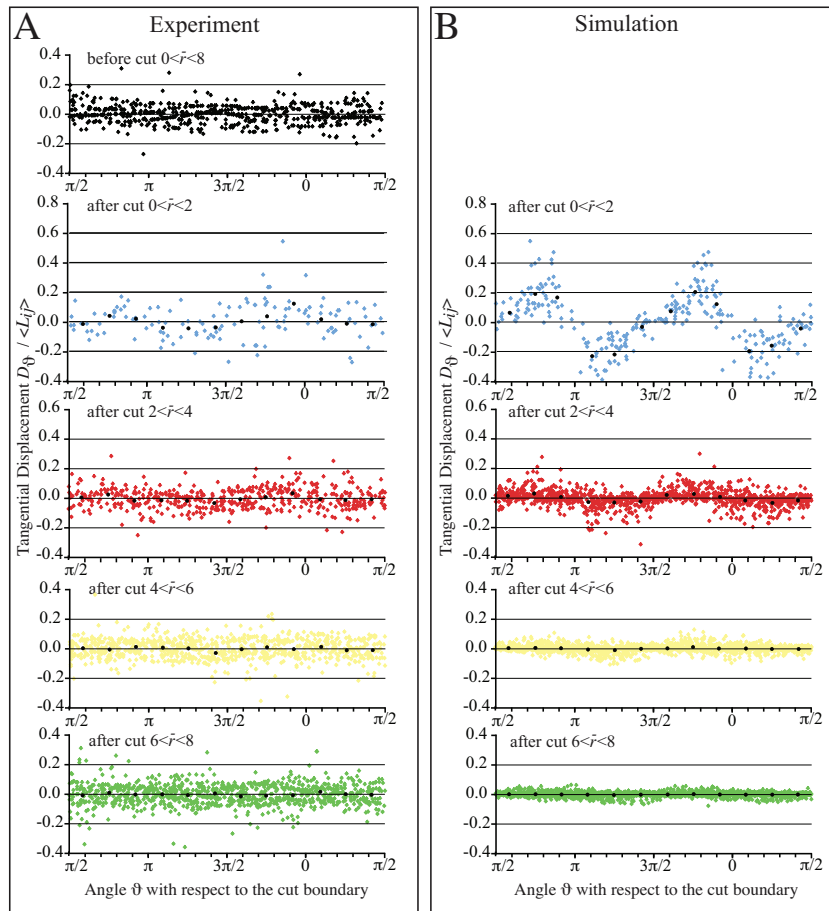
Figure D.1: (A and B) Tangential displacements D_θ of vertices relative to the average bond length $\langle L_{ij} \rangle$ as a function of the angle θ indicated in Fig. 6.5 A. Vertices at different distances from the ablation point are shown in the colors used in Fig. 6.5 A. Black dots show the average displacement for vertices at different angles, grouped in bins of $\pi/6$ radians. (A) shows tangential displacements observed in 20 different experiments. (B) shows tangential displacements obtained in the 50 simulations of bond removal, for which the radial displacements are shown in Fig. 6.5 B.

E   Processing Epithelial Images

| A | B | C |
| Original image | Removed background | Blurred image |
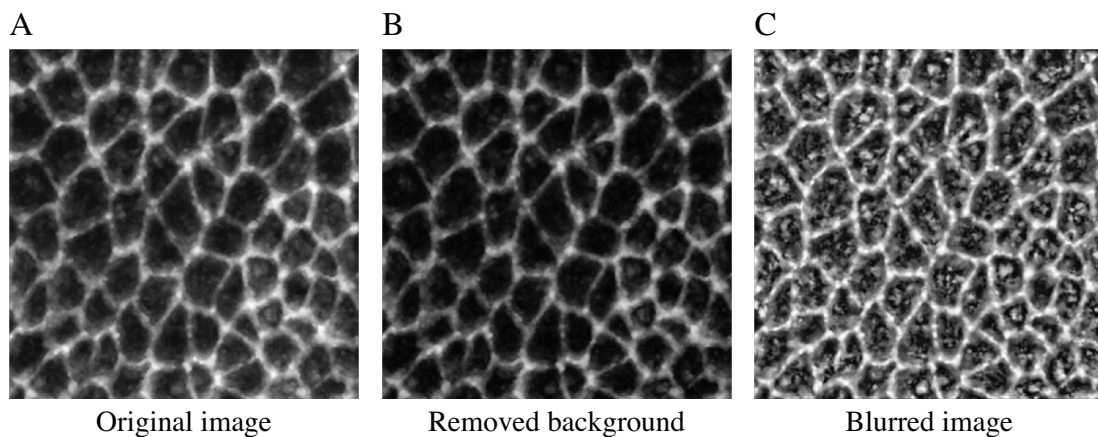
Figure E.1: Filtered epithelial images. (A) Confocal microscopy image of the *Drosophila* wing disc (provided by [3]). This is an input of the image processing software. (B) Processed image after removing the background from the original image. (C) Processed image after enhancing the contrast and slight blurring.

In most cases epithelial images that are captured by confocal microscopy require a series of filtering steps before further analysis. In these images, typically a membrane protein is marked with florescent molecules to detect cell boundaries. An example of such an image is shown in Fig. E.1, first panel. We use MATLAB for image-processing and we always refer to the related functions in MATLAB, however similar functions exist for other programming languages. We do not explain the details of these functions. The first step for processing the image is to subtract the background noise. To estimate the background noise, we first use the IMOPEN() function. We can then use the function IMSUBTRACT() to remove the background noise. The next step after removing the background noise is to enhance the contrast of the image using the ADAPTHISTEQ() function. This function uses contrast-limited adaptive histogram equalization. It selects small regions in the image and enhance the contrast within that region. These small regions are then combined to each other using bilinear interpolation to eliminate the artificially induced boundaries.

One important step before extracting the junctional network of cells is to slightly blur the image. Blurring might reduce details of the image but this is crucial for further processing for the following reason. In the confocal images of epithelial cells, we use florescent proteins that are reach in the adheren junctional network to identify cell boundaries. These proteins are not uniformly distributed and there are regions along cell boundaries that the intensity drops abruptly. To identify a cell in the tissue, we require to detect the region that is bounded by the boundaries of that cell. These regions of low intensity along cell boundaries can generate errors in our cell detection algorithm and slight blurring fills these gaps effectively. If we blur strongly, we might destroy the image very much and one should use proper blurring parameters for each image. We use the function IMFILTER() to blur the image by convolving a Gaussian filter.

To extract the junctional network of cells from these filtered images, we assign to those pixels with intensity higher than a threshold, a value of one, and to the others a value of zero. This threshold is different for each image. After removing those objects in the image that are smaller than a certain size, which correspond to vesicles carrying florescent molecules in tissues, we segment the image into cells. The goal of segmentation is to simplify and change the representation of an image into something that is more meaningful and easier to analyze. For this reason we use a "watershed" algorithm, which is an image processing segmentation algorithm that splits an image into areas based on the topology of the image. In this algorithm, we first identify the enclosed region of each cell and label them $(1, 2, 3, \cdots, N_C)$, where N_C is the total number of cells in the image. We then increase the area of these regions, analogous to filling them with water, until two neighboring cells meet at a border of one pixel width. These borders are then labeled "zero", and are taken as the junctional network of cells. In Fig. E.2 A, we show the watershed segmentation of the epithelial image shown in Fig. E.1, in which each cell is colored differently.

Extracting the junctional network of cells, we can determine the position of vertices in these networks. We define a vertex as the center of a 3×3 pixel box that contains more than two different cell labels. If the box has three different cell labels, the corresponding vertex is three-fold and if it contains four different labels, the vertex is four-fold. Note that we replace two three-fold vertices that are closer than 20% of the average bond length by a four-fold vertex. We show in Fig. E.2 B the junctional network of cells as green lines, representing three-fold and four-fold vertices by red and blue dots, respectively. Knowing the position of vertices, we can determine the number of vertices of each cell and quantify the packing geometry of cells in the images. In Fig. E.2 C, we show the packing geometry of cells in the processed image, where each cell is colored according to its neighbor number (the color code is indicated in Fig. E.2 C). Note that cells on the border of the image are not counted for the purpose of statistics, and are colored in black irrespective of their neighbor number.

We can also quantify area, perimeter and elongation of cells for the processed watershed
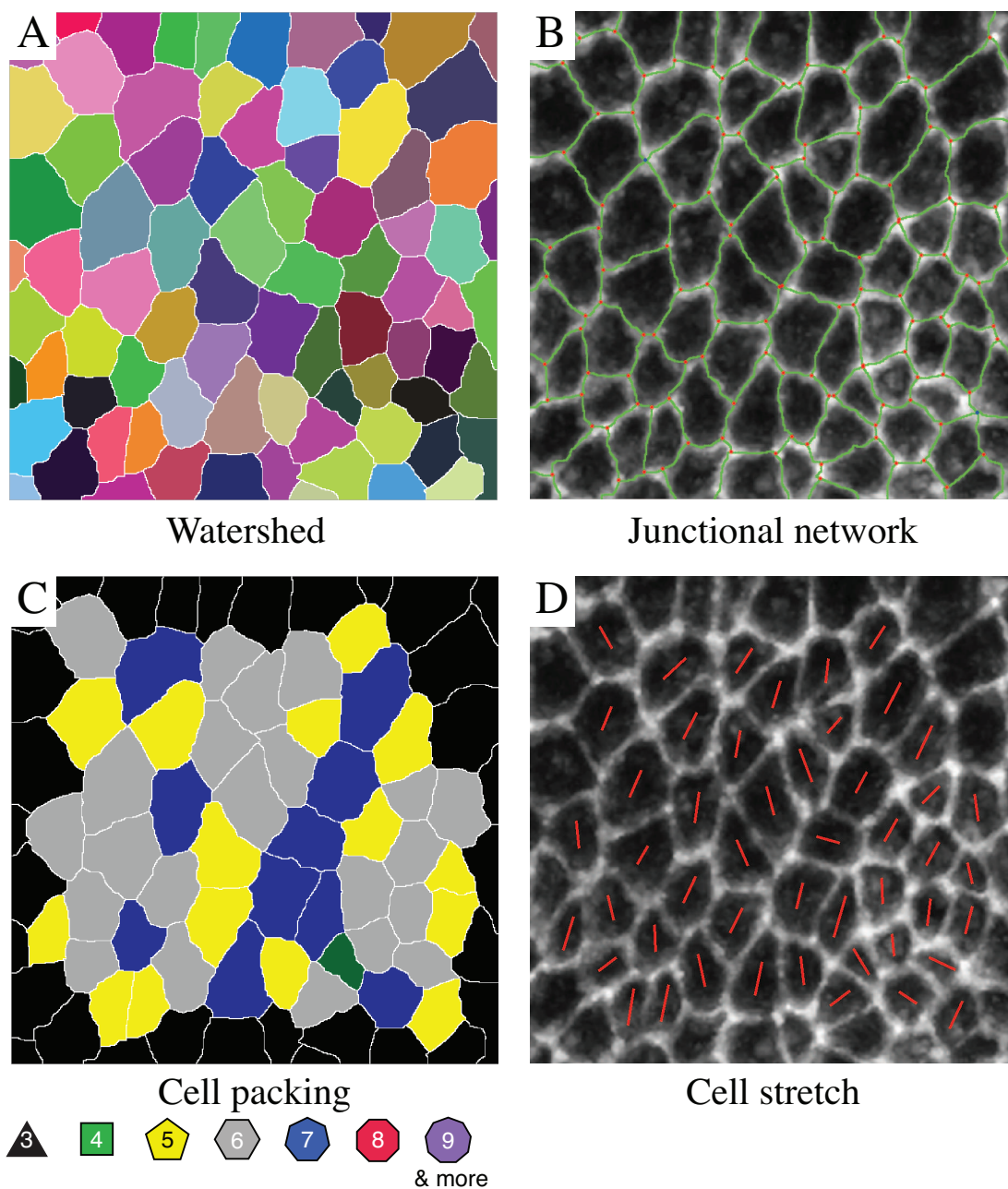
Figure E.2: Processed epithelial images. (A) Watershed segmentation of the processed image. Each cell is colored differently. (B) The junctional network of cells and vertices determined from the watershed segmented image. Three-fold and four-fold vertices are shown by red and blue dots, respectively. (C) Packing geometry of cells in the processed image. Each cell is colored according to its neighbor number. (D) Quantified cell elongation in the processed image. The elongation of cells is shown by red lines passing through the cell center. The length and direction of lines correspond to the magnitude and axis of cell elongation, respectively.

image. Cell area and cell perimeter are simply the number of pixels enclosed by cell boundaries and the number of boundary pixels of that cell, respectively. Knowing the position of boundary pixels of a cell, we can quantify cell elongation calculating a traceless, symmetric stretch tensor of cell α as

$$S_{\gamma\eta}^\alpha = \begin{pmatrix} S_1^\alpha & S_2^\alpha \\ S_2^\alpha & -S_1^\alpha \end{pmatrix}, \tag{E.1}$$

where S_1^α and S_2^α are defined as

$$S_1^\alpha = \frac{1}{A_\alpha} \sum_i \cos 2\theta_i$$
$$S_2^\alpha = \frac{1}{A_\alpha} \sum_i \sin 2\theta_i. \tag{E.2}$$

The sum in Eq. E.2 is over all pixels of cell α and θ is the angle of pixel i with respect to the x axis. A_α is the total number of pixels in cell α. The eigenvalue and eigenvector of the stretch tensor gives us the magnitude and axis of the stretch of the cell, respectively. In Fig. E.2 D, we show cell stretch as a red bar passing through the cell center.

List of Figures

Bibliography

[1] Hayashi, T. and Carthew, R.W. Surface mechanics mediate pattern formation in the developing retina. *Nature*, **431**, 647-652 (2004).

[2] Goodyear, R. and Richardson, G. Pattern formation in the basilar papilla: evidence for cell rearrangement. *J. Neurosci.*, **17**, 6289-6301 (1997).

[3] With the kind permission of Suzanne Eaton lab, Max Planck Institute of Molecular Cell Biology and Genetics, Dresden, Germany.

[4] Wolpert, L. Positional information and the spatial pattern of cellular differentiation. *J. Theor. Biol.* **25**, 1 (1969).

[5] Chuai, M., Zeng, W., Yang, X., Boychenko, V., Glazier, J.A., and Weijer, C.J. Cell movement during chick primitive streak formation. *Dev. Biol.* **296**, 137-149 (2006).

[6] Cui, C., Yang, X., Chuai, M., Glazier, J.A., and Weijer, C.J. Analysis of tissue flow patterns during primitive streak formation in the chick embryo. *Dev. Biol.* **284**, 37-47 (2005).

[7] Bertet, C., Sulak, L., and Lecuit, T. Myosin-dependent junction remodeling controls planar cell intercalation and axis elongation. *Nature* **429**, 667-671 (2004).

[8] Blankenship, J.T., Backovic, S.T., Sanny, J.S., Weitz, O., and Zallen, J.A. Multicellular rosette formation links planar cell polarity to tissue morphogenesis. *Dev. Cell* **11**, 459-470 (2006).

[9] Fristrom, D. The mechanism of evagination of imaginal discs of *Drosophila* melanogaster. III. Evidence for cell rearrangement. *Dev. Biol.* **54**, 163-171 (1976).

[10] Koppen, M., Fernandez, B.G., Carvalho, L., Jacinto, A., and Heisenberg, C.P. Coordinated cell-shape changes control epithelial movement in zebrafish and *Drosophila*. *Development* **133**, 2671-2681 (2006).

[11] Lecuit, T. and Lenne, P.-F Cell surface mechanics and the control of cell shape, tissue patterns and morphologies. *Nature Rev. Mol. Cell Biol.* **8**, 633-644 (2007).

[12] Graner, F., and Glazier, J.A. Simulation of biological cell sorting using a two-dimensional exended Potts model. *Phys. Rev. Lett.* **69**, 2013-2016 (1992).

[13] Mombach, J., de Almeida, R., and Iglesias, J. Mitosis and growth in biological tissues. *Phys. Rev. E* **48**, 598-602 (1993).

[14] Hufnagel, L., Teleman, A.A., Rouault, H., Cohen, S.M., and Shraiman, B.I. On the mechanism of wing size determination in fly development. *Proc. Natl. Acad. Sci. USA* **104**, 3835-3840 (2007).

[15] Käfer, J., Hayashi, T., Marée, A.F.M., Carthew, R. and Graner, F. Cell adhesion and cortex contractility determine cell patterning in the *Drosophila* retina. *Proc. Natl. Acad. Sci. USA* **104**, 18549-18554 (2007).

[16] Hilgenfeldt, S., Erisken, S., and Carthew, R.W. Physical modeling of cell geometric order in an epithelial tissue. *Proc. Natl. Acad. Sci. USA* **104**, 3835-3840 (2007).

[17] Byrne, H.M., King, J.R., McElwain, D.L.S. and Preziosi, L. A two-phase model of solid tumor growth. *Appl. Math. Letters* **16**, 567-573 (2003).

[18] MacArthur, B.D. and Please, C.P. Residual stress generation and necrosis formation in multi-cell tumour spheroids. *J. Math. Biol.*, **49**, (6), 537-552 (2004).

[19] Bittig, T., Wartlick, O., Kicheva, A., Gonza'lez-Gaita'n, M. and Jülicher, F. Dynamics of anisotropic tissue growth. *New J. Phys.* **10**, 063001 (2008).

[20] Thoumine, O. and Ott, A. Time scale dependent viscoelastic and contractile regimes in fibroblasts probed by microplate manipulation. *J. Cell Sci.* **110**, 2109-2116 (1997).

[21] Forgacs, G., Foty, R.A., Shafrir, Y. and Steinberg, M.S. Viscoelastic properties of living embryonic tissues: a quantitative study. *Biophys. J.* **74**, 2227-2234 (1998).

[22] Glazier, J.A. and Graner, F. Simulation of the differential adhesion driven rearrangement of biological cells. *Phys. Rev. E* **47**, 2128-2154 (1993).

[23] Zajac, M., Jones, G.L. and Glazier, J.A. Model of convergent extension in animal morphogenesis. *Phys. Rev. Lett.* **85**, 2022-2025 (2000).

[24] Zajac, M., Jones, G.L. and Glazier, J.A. Viscoelastic properties of living embryonic tissues: a quantitative study. *J. Theo. Biol.* **222**, 247-259 (2003).

[25] Schwann, T. Microscopical researches into the accordance of structure and growth in animals and plants. *Syndenham Society, London* (1847).

[26] Thompson, D.W. On growth and forms. *Cambridge university press, New York* (1961).

[27] Gibson, M.C., Patel, A.B., Nagpal, R., and Perrimon, N. The emergence of geometric order in proliferating metazoan epithelia. *Nature* **442**, 1038-1041 (2006).

[28] Cowan, R. and Morris, V.B. Cell population dynamics during the differentiative phase of tissue development. *J. Theo. Biol.* **122**, 205-224 (1986).

[29] Cowan, R. and Morris, V.B. Division rules for polygonal cells. *J. Theo. Biol.* **131**, 33-42 (1988).

[30] Lewis, F.T. The correlation between cell division and the shapes and sizes of prismatic cells in the epidermis of cucumis. *Anat. Rec.* **38**, 341-376 (1928).

[31] Lewis, F.T. The geometry of growth and cell division in epithelial mosaics. *Am. J. Bot.* **30**, 766-776 (1943).

[32] Rivier, N. and Lissowski, A. On the correlation between sizes and shapes of cells in epithelial mosaics, *J. Phys. A: Math. Gen.* **15**, L143-L148 (1982).

[33] Weaire, D., Rivier, N. Soap, cells and statistics- Random patterns in two dimensions. *Contemp. Phys.* **25**, 59-99 (1984).

[34] Rivier, N. Statistical crystallography structure of random cellular networks. *Philos. Mag. B* **52** 795-819 (1985).

[35] Zallen, J.A. Planar Polarity and Tissue Morphogenesis. *Cell* **129**, 1051-1063 (2007).

[36] Adler, P.N. Planar signaling and morphogenesis in *Drosophila*. *Dev. Cell* **2**, 525-535 (2002).

[37] Keller, R., Davidson, L., Edlund, A., Elul, T., Ezin, M., Shook, D., and Skoglund, P. Mechanisms of convergence and extension by cell intercalation. *Philos. Trans. R. Soc. Lond. B Biol. Sci.* **355**, 897-922 (2000).

[38] Seifert, J.R.K and Mlodzik, M. Frizzled/PCP signalling: a conserved mechanism regulating cell polarity and directed motility *Nat. Rev. Gen.* **8**, 126-138 (2007).

[39] Myers, D.C., Sepich, D.S., and Solnica-Krezel, L. Convergence and extension in vertebrate gastrulae: cell movements according to or in search of identity? *Trends Genet.* **18**, 447-455 (2002).

[40] Wallingford, J.B., Fraser, S.E., and Harland, R.M. Convergent extension: the molecular control of polarized cell movement during embryonic development. *Dev. Cell* **2**, 695-706 (2002).

[41] Dabdoub, A., and Kelley, M.W. Planar cell polarity and a potential role for a Wnt morphogen gradient in stereociliary bundle orientation in the mammalian inner ear. *J. Neurobiol.* **64**, 446-457 (2005).

[42] Zheng, L., Zhang, J., and Carthew, R.W. Frizzled regulates mirror-symmetric pattern formation in the *Drosophila* eye. *Development* **121**, 3045-3055 (1995).

[43] Wolff, T., and Rubin, G.M. Strabismus, a novel gene that regulates tissue polarity and cell fate decisions in *Drosophila*. *Development* **125**, 1149-1159 (1998).

[44] Adler, P., Lee, H. Frizzled signaling and cell-cell interactions in planar polarity. *Curr. Opin. Cell Biol.* **13**, 635-640 (2001).

[45] Gubb, D., Garcia-Bellido, A. A genetic analysis of the determination of cuticular polarity during development in *Drosophila melanogaster*. *J. Embryol. Exp. Morphol.* **68**, 37-57 (1982).

[46] Shulman, J.M., Perimon, N., Axelrod, J.D. Frizzled signaling and the developmental control of cell polarity. *Trends Genet.* **14**, 452-458 (1998).

[47] Strutt, H., Strutt, D. Polarity determination in the *Drosophila* eye. *Curr. Opin. Genet. Dev.* **9**, 442-446 (1999).

[48] Vinson, C.R., Adler, P.N. Directed non-cell autonomy and the transmission of polarity information by the frizzled gene of *Drosophila*. *Nature* **329**, 549-551 (1987).

[49] Wong, L.L., Adler, P.N. Tissue polarity genes of *Drosophila* regulate the subcellular location for prehair initiation in pupal wing cells. *J. Cell Biol.* **123**, 209-221 (1993).

[50] Vinson, C.R., Conover, S., and Adler, P.N. A Drosophila tissue polarity locus encodes a protein containing seven potential transmembrane domains. *Nature* **338**, 263-264 (1989).

[51] Taylor, J., Abramova, N., Charlton, J., and Adler, P.N. Van Gogh: a new Drosophila tissue polarity gene. *Genetics* **150**, 199-210 (1998).

[52] Chae, J., Kim, M.J., Goo, J.H., Collier, S., Gubb, D., Charlton, J., Adler, P.N., and Park, W.J. The Drosophila tissue polarity gene starry night encodes a member of the protocadherin family. *Development* **126**, 5421-5429 (1999).

[53] Usui, T., Shima, Y., Shimada, Y., Hirano, S., Burgess, R.W., Schwarz, T.L., Takeichi, M., and Uemura, T. Flamingo, a seven-pass transmembrane cadherin, regulates planar cell polarity under the control of Frizzled. *Cell* **98**, 585-595 (1999).

[54] Klingensmith, J., Nusse, R., and Perrimon, N. The Drosophila segment polarity gene dishevelled encodes a novel protein required for response to the wingless signal. *Genes Dev.* **8**, 118-130 (1994).

[55] Theisen, H., Purcell, J., Bennett, M., Kansagara, D., Syed, A., and Marsh, J.L. Dishevelled is required during wingless signaling to establish both cell polarity and cell identity. *Development* **120**, 347-360 (1994).

[56] Tree, D.R., Shulman, J.M., Rousset, R., Scott, M.P., Gubb, D., Axelrod, J.D. Prickle mediates feedback amplification to generate asymmetric planar cell polarity signaling. *Cell* **109**, 371-381 (2002).

[57] Feiguin, F., Hannus, M., Mlodzik, M., and Eaton, S. The ankyrin repeat protein Diego mediates Frizzled-dependent planar polarization. *Dev. Cell* **1**, 93-101 (2001).

[58] Shimada, Y., Usui, T., Yanagawa, S., Takeichi, M., and Uemura, T. Asymmetric colocalization of Flamingo, a seven-pass transmembrane cadherin, and Dishevelled in planar cell polarization. *Curr. Biol.* **11**, 859-863 (2001).

[59] Axelrod, J.D. Unipolar membrane association of Dishevelled mediates Frizzled planar cell polarity signaling. *Genes Dev.* **15**, 1182-1187 (2001).

[60] Strutt, D.I. Asymmetric localization of frizzled and the establishment of cell polarity in the *Drosophila* wing. *Mol. Cell* **7**, 367-375 (2001).

[61] Das, G., Jenny, A., Klein, T.J., Eaton, S., Mlodzik, M. Diego interacts with Prickle and Strabismus/Van Gogh to localize planar cell polarity complexes. *Development* **131**, 4467-4476 (2004).

[62] Bastock, R., Strutt, H., and Strutt, D. Strabismus is asymmetrically localized and binds to Prickle and Dishevelled during *Drosophila* planar polarity patterning. *Development* **130**, 3007-3014 (2003).

[63] Wong, H.C., Bourdelas, A., Krauss, A., Lee, H.J., Shao, Y., Wu, D., Mlodzik, M., Shi, D.L., Zheng, J. Direct binding of the PDZ domain of Dishevelled to a conserved internal sequence in the C-terminal region of Frizzled. *Mol. Cell* **12**, 1251-1260 (2003).

[64] Jenny, A., Darken, R.S., Wilson, P.A., and Mlodzik, M. Prickle and Strabismus form a functional complex to generate a correct axis during planar cell polarity signaling. *EMBO J.* **22**, 4409-4420 (2003).

[65] Locke, M. The cuticular pattern in an insect, Rhodnius Prolixus. *J. Exp. Biol.* **36** 459-477 (1959).

[66] Lawrence, P.A. Gradients in the insect segment: the orientation of hairs in the milkweed bug Oncopeltus fasciatus. *J. Exp. Biol.* **44** 607-620 (1966).

[67] Stumpf, H.F. Über gefälleabhängige Bildungen des Insektensegmentes. *J. Insect. Physiol.* **12** 601-617 (19660).

[68] Lawrence, P.A., Crick, F.H.C., Munro, M. A gradient of positional information in an insect, Rhodnius. *J. Cell. Sci.* **11** 815-853 (1972).

[69] Park, W.J., Liu, J., Adler, P.N. The frizzled gene of Drosophila encodes a membrane protein with an odd number of transmembrane domains. *Mech. Dev.* **45** 127-137 (1994).

[70] Amonlirdviman, K., Khare, N.A., Tree, D.R., Chen, W.S., Axelrod, J.D., and Tomlin, C.J. Mathematical modeling of planar cell polarity to understand domineering nonautonomy. *Science* **307**, 423-426 (2005).

[71] Gilbert, S.F. Developmental Biology. *Sinauer* (2008).

[72] Rothwell, W.F. and Sullivan,W. Fluorescent analysis of *Drosophila* embryos In *Drosophila* Protocols. *Cold Spring Harbor Laboratory Press* (1999)

[73] Gergely, F., Kidd, D., Jeffers, K., Wakefield, J.G., and Raff, J.W. D-TACC: a novel centrosomal protein required for normal spindle function in the early *Drosophila* embryo *The EMBO Journal* **19**, 241-252 (2000).

[74] Wolpert, L. Principles of development. *Oxford Univ. Press* (2002).

[75] Paddock, S.W. Confocal microscopy methods and protocols (methods in molecular biology). *Humana Press* (1999).

[76] Gennes, P.-G de and Prost, J. The physics of liquid crystals. *Clarendon Press, Oxford* (2007).

[77] Friedlander, D.R., M'ege, R.M., Cunningham, B.A., and Edelman, G.M. Cell sorting-out is modulated by both the specificity and amount of different cell adhesion molecules (CAMs) expressed on cell surfaces. *Proc. Natl. Acad. Sci. USA* **86**, 7043 (1989).

[78] Steinberg, M.S. Reconstruction of tissues by dissociated cells. *Science* **141**, 401 (1963).

[79] Steinberg, M.S., and Takeichi, M. Experimental specification of cell sorting, tissue spreading, and specific spatial patterning by quantitative differences in cadherin expression. *Proc. Natl. Acad. Sci. USA* **91**, 206 (1994).

[80] Dahmann, C. and Basler, K. Compartment boundaries at the edge of development. *Trends in Genetics* **15**, 320 (1999).

[81] Classen, A., Anderson, K., Marois, E., and Eaton, S. Hexagonal packing of *Drosophila* wing epithelial cells by the planar cell polarity pathway. *Dev. Cell* **9**, 805-817 (2005).

[82] Gong, Y., Mo, C., and Fraser, S. E. Planar cell polarity signalling controls cell division orientation during zebrafish gastrulation. *Nature* **430**, 689-693 (2004).

[83] Simons, M. and Mlodzik, M. Planar cell polarity signaling: from fly development to human disease. *Annu. Rev. Genet.* **42**, 517-540 (2008).

[84] Carreira-Barbosa, F., Concha, M.L., Takeuchi, M., Ueno, N., Wilson, S.W., Tada, M. Prickle1 regulates cell movements during gastrulation and neuronal migration in zebrafish. *Development* **130** 4037-4046 (2003).

[85] Djiane A., Riou J., Umbhauer M., Boucaut J., Shi D. Role of frizzled 7 in the regulation of convergent-extension movements during gastrulation in Xenopus laevis. *Development* **127** 3091-3100 (2000).

[86] Heisenberg, C.P., Tada, M., Rauch, G.J., Saude, L., Concha, M.L., Geisler, R., Stemple, D.L., Smith, J.C., Wilson, S.W. Silberblick/Wnt11 mediates convergent extension movements during zebrafish gastrulation. *Nature* **405**, 76-81 (2000).

[87] Kinoshita N., Iioka H., Miyakoshi A., Ueno N. PKC delta is essential for Dishevelled function in a noncanonical Wnt pathway that regulates Xenopus convergent-extension movements. *Genes Dev.* **17** 1663-1676 (2003).

[88] Ma, D., Amonlirdviman, K., Raffard, R.L., Abate, A., Tomlin, C.J., Axelrod, J.D. Cell packing influences planar cell polarity signaling. *Proc. Natl. Acad. Sci. USA* **105**, 18800-18805 (2008).

[89] Garcia-Bellido, A., Ripoll, P., and Morata, G. Developmental compartmentalisation of the wing disk of *Drosophila*. *Nat. New Biol.* **245**, 251-253 (1973).

[90] Garcia-Bellido, A., Ripoll, P., and Morata, G. Developmental compartmentalization in the dorsal mesothoracic disc of *Drosophila*. *Dev. Biol.* **48**, 132-147 (1976).

[91] O'Brochta, D.A, and Bryant, P.T. A zone of non-proliferating cells at a lineage restriction boundary in Drosophila. *Nature* **313**, 138-141 (1985).

[92] Morata, G. and Ripoll, P. Minutes: mutants of Drosophila autonomously affecting cell division rate. *Dev. Biol.* **42**, 211-221 (1975).

[93] Simpson, P. Parameters of cell competition in the compartments of the wing of Drosophila. *Dev. Biol.* **69**, 182-193 (1979).

[94] Simpson, P. and Morata, G. Differential mitotic rates and pattern of growth in compartments in the *Drosophila* wing. *Dev. Biol.* **85**, 299-308 (1981).

[95] Moreno, E., Basler, K., and Morata, G. Cells compete for Decapentaplegic survival factor to prevent apoptosis in Drosophila wing development. *Nature* **416**, 755-759 (2002).

[96] Fletcher, R. and Reeves, C.M. Function minimization by conjugate gradients. *Comput. J.* **7**(2), 149-154 (1964).

[97] Polak, E. and Ribiere, G. Note sur la convergence de methods de directions conjuguees. *Rev. Fr. Inform. Rech. Oper.* **16**, 35-43 (1969).

[98] Ranft, J. Interfaces in growing tissue. Diploma Thesis. *TU Dresden* (2008).

Erklärung

Hiermit versichere ich, dass ich die vorliegende Arbeit ohne unzulässige Hilfe Dritter und ohne Benutzung anderer als der angegebenen Hilfsmittel angefertigt habe; die aus fremden Quellen direkt oder indirekt übernommenen Gedanken sind als solche kenntlich gemacht. Die Arbeit wurde bisher weder im Inland noch im Ausland in gleicher oder ähnlicher Form einer anderen Prüfungsbehörde vorgelegt. Die vorliegende Arbeit wurde vom 19.09.2005 bis 26.03.2009 unter der Aufsicht von Prof. Dr. Frank Jülicher am Max-Planck-Institut für Physik komplexer Systeme in Dresden durchgeführt.

Ich versichere, dass ich bisher keine erfolglosen Promotionsverfahren unternommen habe. Ich erkenne die Promotionsordnung der Fakultät Mathematik und Naturwis-senschaften der Technischen Universität Dresden an.

Dresden, den 26. März 2009, Reza Farhadifar